Sebastian Dunst, DI (FH)

Polymer – copper indium sulphide hybrid solar cells: Operational stability and novel device architectures

DOCTORAL THESIS

to achieve the university degree of

Doktor der technischen Wissenschaften

submitted to

Graz University of Technology

Supervisor:

Assoc. Prof. DI Dr. Gregor Trimmel

Institute for Chemistry and Technology of Materials

Graz, 03-2016

AFFIDAVIT

I declare that I have authored this thesis independently, that I have not used other than the declared sources / resources, and that I have explicitly marked all material which has been quoted either literally or by content from the used sources. The text document uploaded to TUGRAZonline is identical to the present doctoral thesis.

…… ……..

Date Signature

Abstract

The main part of this thesis deals with operating stability issues of polymer-copper indium sulphide (CIS) hybrid solar cells that have been prepared according to a novel route for the direct formation of CIS nanoparticles within a polymer matrix. A mixture of precursor chemicals for the formation of CIS (i.e copper and indium xanthates) and a semiconducting polymer get dissolved together and coated on a substrate. During a moderate thermal annealing step below 200°C the precursor chemicals are converted into CIS nanocrystals and a hybrid nanocomposite absorber layer is obtained. Polymer-CIS hybrid solar cells in the architecture indium-tin-oxide (ITO)|poly(3,4-ethylene-dioxythiophene)-poly(styrenesulfonate) (PEDOT:PSS)|absorber-layer|Al show power conversion efficiencies up to 2.8%; however, the limited stability of these devices which lies in the range of hours is an issue. It has been found that the aluminum electrode is the main factor for degradation and by replacing aluminum with silver, the devices show stable behavior over several thousand hours of operation under permanent illumination when appropriately encapsulated; however, due to lower open circuit voltages, power conversion efficiencies of devices with silver electrodes are typically lower than that of devices with aluminum electrodes. Therefore, in a next step the influence of titanium and TiO_x cathode interlayers on device performance and stability has been investigated. The introduction of these interlayers leads to higher open circuit voltages of solar cells with silver electrodes and to enhanced lifetimes of devices with aluminum electrodes. In a further series of experiments, the so called inverted device architecture has been explored. Inverted hybrid solar cells with power conversion efficiencies up to 2.1% could be realized in the architecture ITO|TiO_x|absorber-layer|PEDOT:PSS|Ag. In the second part of this thesis, a route towards ordered nanostructured polymer-CIS hybrid solar cells is investigated. For this purpose, polymer layers have been nanostructured by nanoimprint lithography and the obtained surface morphology has been characterized by the means of scanning electron microscopy and gracing incidence small angle X-ray scattering. As the nanostructures showed a reasonable thermal stability up to the conversion temperature of the xanthates, hybrid solar cells have been fabricated by infiltration of the imprinted structures with copper- and indium xanthates followed by a thermal conversion. The obtained nanostructured bilayer hybrid solar cells show significantly better photovoltaic performance as similar prepared devices with flat interfaces.

Kurzfassung

Der Hauptteil dieser Arbeit beschäftigt sich mit der Stabilität von Polymer-Kupferindiumdisulfid (CIS) Hybridsolarzellen, die nach einer neuartigen Route für die direkte Bildung von CIS Nanopartikel innerhalb einer Polymermatrix hergestellt wurden. Precursorchemikalien (Kupfer- und Indium-Xanthate) für die Bildung von CIS und ein halbleitendes Polymer werden zusammen gelöst und auf ein Substrat aufgetragen. Während eines thermischen Umwandlungsschritts unterhalb von 200°C reagieren die Precursorchemikalien zu CIS und eine Hybrid-Nanokomposit-Absorberschicht wird erhalten. Polymer-CIS Hybridsolarzellen in der Architektur Indiumzinnoxid (ITO)|Poly(3,4-ethylendioxythiophen)-Poly(styrolsulfonat) (PEDOT:PSS)|Absorberschicht|Al zeigen Wirkungsgrade von bis zu 2.8%, jedoch stellt die begrenzte Stabilität dieser Solarzellen, die im Bereich von Stunden liegt, ein Problem dar. Es zeigte sich, dass die Aluminiumelektrode einen wesentlichen Anteil an der raschen Degradation hat und durch den Ersatz von Aluminium mit Silber, zeigen eingekapselte Solarzellen ein stabiles Verhalten über mehrere tausend Stunden unter Dauerbeleuchtung. Jedoch sind aufgrund von niedrigeren Leerlaufspannungen die Wirkungsgrade dieser Zellen niedriger. Daher wurde der Einfluss von Titan- und TiO_x-Kathodenzwischenschichten auf den Wirkungsgrad und die Stabilität untersucht. Die Anwendung dieser Zwischenschichten führt zu höheren Leerlaufspannungen von Solarzellen mit Silberelektroden und zu einer erhöhten Lebensdauer der Zellen mit Aluminiumelektroden. In weiteren Experimenten wurde die inverse Zellarchitektur realisiert. In der Architektur ITO|TiO_x|Absorberschicht|PEDOT:PSS|Ag konnten inverse Hybridsolarzellen mit Wirkungsgraden von bis zu 2.1% erhalten werden. Im zweiten Teil dieser Arbeit wurde eine Methode, um nanostrukturierte Polymer-CIS Hybridsolarzellen mit geordneten Morphologien herzustellen untersucht. Hierzu wurden Polymerschichten mittels Nanoimprintlithographie strukturiert und die erhaltene Oberflächenmorphologie wurde mittels Rasterelektronenmikroskopie und Röntgenkleinwinkelstreuung mit streifendem Einfall charakterisiert. Da die Nanostrukturen eine angemessene thermische Stabilität bis zu der Umwandlungstemperatur der Xanthate zeigten, wurden Hybridsolarzellen durch Infiltration der geprägten Strukturen mit Kupfer- und Indium-Xanthaten, gefolgt von einer thermischen Umwandlung hergestellt. Die erhaltenen nanostrukturierten Bilayer-Hybridsolarzellen zeigen deutlich bessere Wirkungsgrade als ähnlich hergestellte Zellen mit planaren Grenzflächen.

Acknowledgments

First of all, I want to express my gratitude to my supervisor Assoc. Prof. DI Dr. Gregor Trimmel for giving me the opportunity to conduct my PhD thesis on the very interesting topic of polymer-$CuInS_2$ hybrid solar cells, his patience and of course for his excellent supervision and pleasant permanent support during my work.

Moreover, I want to convey my appreciation to DI Dr. Thomas Rath for always sharing his knowledge and experience in the field of research, having an ear for concerns, bringing useful ideas and inspirations and for guiding me through my first scientific publications.

I want to thank DI Dr. Eugen Maier for planning and assembling the automated measuring system used for the stability tests performed in this work and Lukas Troi for manufacturing several useful tools (sample holders, measuring chambers) for solar cell characterization and for his measuring software developments. I want to thank all members of the former Christian Doppler Labor für Nanokomposit Solarzellen for the fruitful discussions and the excellent collaboration as well as my office colleagues for the friendly and enjoyable atmosphere and students for performing several experiments in the frame of project laboratories.

I want to express my gratitude to DI Dr. Heinz Amenitsch, Dr. Benedetta Marmiroli and MSc. Barbara Sartori for getting insights into GISAXS and GIWAXS techniques at the Austrian SAXS beamline at Elettra Trieste and the group of Dr. Massimo Tormen (Instituto Officina dei Materiali IOM-CNR Laboratorio TASC), especially Dr. Andrea Radivo who conducted NIL structuring of polymer layers. I further want to thank Sebastian Rauch for the preparation of ion polished cross sections of the solar cells for SEM characterization and Dr. Angelika Reichmann as well as Sanja Simic for acquiring the images, DI Dr. Thomas Griesser for XPS measurements and MSc. Huei-Ting Chien for EQE measurements.

Financial support by the Isovoltaic AG, the Polymer Competence Center Leoben GmbH and the Österreichische Forschungsförderungsgesellschaft is gratefully acknowledged.

My deepest gratitude is dedicated to my friends, my family and especially to my father who supported and motivated me all over my life.

Table of contents

1. Introduction

1.1 Motivation

We are living in a world where energy is one of the most important factors for economic development and prosperity of any country. Over 80% of the world´s energy demand today is covered by burning fossil fuels such as coal, natural gas or oil.[1] The thereby liberated carbon dioxide and other greenhouse gases contribute significantly to global warming, smog or acid rain. Through a steady increase in population as well as the industrialization of threshold countries, the total world energy consumption is projected to further increase in the upcoming decades. In order to reduce harmful emissions or environmentally degradation and the fact that fossil fuels are limited, we are obliged to improve overall energy efficiency and reflect on alternative, renewable forms of energy.

Besides the fact that wind, hydro, biomass and fossil fuel energy have their origins in sunlight as well, the direct use of naturally available solar energy shows an immense potential to cover part of future world´s energy demand. Photovoltaic (PV) technologies can be seen as a clean energy source as the direct conversion of sunlight to electricity occurs without environmental emissions or the consumption of fresh water during operation. In the field of photovoltaics encouraging progress has been made over the last years, evolving from a relative expensive niche market and small scale applications in the 1990s to a recent large-scale global deployment and increased competitiveness as in the year 2014 PV had a share of more than 1% of the global electricity supply for the first time.[2] This seems to be only the beginning of the future market relevance as its share is envisioned to rise up to 16% by 2050.[3] Thus the development of an affordable, reliable and clean as well as sustainable solar energy innovation, offering new technological solutions and opening up new market segments could have huge long-term benefits.

1.2 History of photovoltaics

The term photovoltaic has its etymological origin in the Greek work “phōs” meaning "light" and in the term "volt" on the basis of the physicist A. Volta, a pioneer in electricity and the inventor of the electrical battery.

The first work related to photovoltaics goes back to the year 1873, when W. Smith and J. May identified enhanced conductivity of selenium when exposed to light.[4] Four years later W. G. Adams and R. E. Day discovered that selenium itself produces electricity when exposed to light.[5] In 1883 C. Fritts built the first photovoltaic module of selenium cells[6] but the solar cells did not provide enough power for electrical equipment and technical potential has been doubted. In parallel deeper insights in the nature of electromagnetic radiation was gained. H. R. Hertz and W. Hallwachs investigated the external photoelectric effect from the year 1886 onwards,[7] which was experimentally discovered earlier in 1839 by A. E. Becquerel.[8] In 1905 this effect was theoretically interpreted by A. Einstein and for the first time the modern photon concept was introduced.[9]

In the year 1904 a copper oxide solar photocell was presented.[10] Power conversion efficiency was far below 1%, nonetheless various areas of application began to become conceivable. In 1940 R. S. Ohl noted that a current could be generated by the illumination of silicon.[11] He also worked in the field of doping semiconductors with impurities to change their electrical properties.

The breakthrough came in 1954 as D. Chapin, C. S. Fuller and G. Pearson from the Bell Laboratories exhibited silicon solar cells with efficiencies of about 6%.[12] In 1958 the first solar powered space satellite Vanguard 1 was launched into space and communication was possible up to 1964. From the seventies on, performance of solar cells improved and production costs were lowered, leading to the deployment of several terrestrial off-grid powering applications.

Classical monocrystalline silicon solar cells today show power conversion efficiencies up to 25.6%[13] in laboratory scale and typically module efficiencies between 14% and 21.5%.[14] Multicrystalline silicon solar cells are less expensive in production, but also less efficient (20.8% in laboratory scale, modules up to 18.5%).[14] The price (USD per Watt peak) of crystalline silicon solar cells dropped steadily in the last decades but industry observers are the opinion that the price floor for this technology is near.[15]

The production of these cells still requires expensive clean-room technologies and high energy consumption. In addition, a significant material loss occurs while cutting silicon wafers to a thickness of about 150 to 200 micrometers.

Thin film technologies like amorphous silicon, CIGS (copper indium gallium sulphide, selenide) and CdTe (cadmium telluride) solar cells can be produced at lower prices. The lowered manufacturing costs can be attributed to a lowered thermal budget and lowered material usage, as direct bandgap semiconductors are used as absorber layer and thicknesses are typically in the range between sub-microns to tens of micrometers. Amorphous silicon solar cells show power conversion efficiencies around 10%,[14] whereas CIGS and CdTe solar cells in contrast already show laboratory scale efficiencies above 20%[16,17] and module efficiencies of about 15%.[18,19] However, the toxicity of the cadmium is in discussion and indium as well as tellurium is short in supply.[20]

Highest power conversion efficiencies up to 46.0% in laboratory scale can be achieved with multi-junction solar cells (such as a GaInP/GaAs/GaInAsP/GaInAs four junction cell) under concentrated sunlight.[14]

In 2014, the market share of silicon based PV technology accounted for about 92% of the total annual production, where the share of multicrystalline silicon technology was about 56% of total production. The market share of all thin film technologies was about 9% of the total production.[21] The total cumulative installed PV capacity amounted to 183 GWp at the end of 2014, while concentrator photovoltaic technologies amounted to 360 MWp.[22]

Another approach to reduce the production costs is the deployment of organic semiconductors instead of classical inorganic semiconductors. Due to higher absorption coefficients in organic semiconductors, absorber layer thicknesses in the range of 100 nm are feasible. The possibility of printing modules at relative high throughput using roll-to-roll coating and printing techniques like slot die coating, gravure coating, spray coating or ink jet printing opens the opportunity of low-cost mass production resulting in short energy payback times.[23,24] In the case of further so called third generation photovoltaic cells, the absorber layer combines organic and inorganic semiconductors. The concept of the hybrid solar cell will be introduced in the upcoming chapters. Other emerging photovoltaic technologies exhibiting closely related device structures such as

quantum dot solar cells,[25] dye-sensitized solar cells[26] and perovskite solar cells[27,28] are not covered in this work.

Organic photovoltaic (OPV) as well as hybrid photovoltaic applications could fill niche markets in on- and off-grid usage. Main advantages could be mechanical flexibility, semi-transparency, color tunability and ease in integrity into existing architectural elements. Furthermore, its usage in lightweight and portable or even wearable electronics seems to be a key selling point.[29]

1.3 Milestones in the field of organic photovoltaics

Despite the fact that studies on photoconductivity, occurring photovoltages and rectifying effects of organic materials placed between different electrodes have been performed earlier,[30] first organic solar cells were presented in 1975 by C. W. Tang and A. C. Albrecht. They sandwiched chlorophyll-a between two different metal electrodes and a power conversion efficiency of 0.01% has been reported.[31] A significant milestone was achieved eleven years later in 1986 as Tang reported the first organic solar cell with an efficiency of 1% by introducing an electron donor-acceptor system.[32] The first polymer-buckminsterfullerene (C_{60}) solar cell in bilayer architecture was presented in 1992.[33]

With the introduction of the first soluble derivatives of C_{60} in combination with soluble PPV derivatives, solution processed organic solar cells with efficiencies around 2.5% have been published.[34,35] Further optimizations were done with the use of soluble polythiophene derivatives. These polymers show morphology changes due to annealing (higher degree in crystallinity) and in combination with a soluble C_{60} derivate, phenyl-C_{61}-butyric acid methyl ester (PCBM), organic solar cells with efficiencies of 4.4%-5% have been reported.[36,37]

The introduction of donor-acceptor polymers, which consist of electron rich segments and electron deficient units along the polymer backbone led to broader spectral light absorption. Due to this strategy, in combination with novel electrode interlayer materials, efficiencies over 10% could be reached.[14,38] A co-evaporated “small molecule” organic solar cell in tandem architecture marks the benchmark up to day, showing 12% cell efficiency at laboratory scale (active area: 1.1 cm^2).[39]

1.4 Hybrid solar cells

Inorganic-organic hybrid solar cells, in which a conjugated polymer and an inorganic semiconductor form the absorber layer, could be a promising alternative approach to the already well-established organic solar cells. The advantages of hybrid solar cells are the capability of additional spectral contribution of photocurrent via the inorganic semiconductor, which can be tuned, as the bandgap of the nanoparticles is not only material- but also particle size-dependent. The inorganic components usually show higher charge carrier mobilities and better environmental stabilities than organic materials. Thus the incorporation of inorganic materials in fabrication methods established from organic semiconductor processing, such as low-cost roll-to-roll production technologies on light weight and flexible substrates with high throughput constitutes the possible advantage of hybrid solar cells compared to inorganic as well as organic solar cells.

While hybrid solar cells have been researched since more than 15 years, in particular in the last years notable progress has been achieved in the understanding of synthesis, characterization and device assembly leading to power conversion efficiencies up to 5.5%, realized with a polymer-PbS,Se absorber layer.[40] Examples for further promising systems are based on CdS,[41,42] CdSe,[43,44] CdTe,[45] Sb_2S_3,[46] ZnO,[47] or $CuInS_2$ (CIS)[48,49] nanoparticles in combination with different conjugated polymers.

1.5 Electrical conductivity in organic materials

The semiconducting properties of organic materials can be attributed to the presence of a conjugated system, where π-electrons and lone pair electrons are not attached to a particular atom or bond in the molecule. This delocalization leads to different energetically equivalent resonance forms of the molecule, which lowers the overall energy and increases the stability. Conjugation occurs in molecules with alternating single and multiple bonds (mostly double bonds).

Overlapping p_z orbitals form energetically lower bonding (π) and energetically higher antibonding (π*) orbitals. Due to the Pauli exclusion principle and Hund's rules, both electrons of the sp^2 (or sp) hybridized atoms contribute to the double (or triple) bond located in the π-orbital, forming the so called HOMO (highest occupied molecular

orbital). The unoccupied π*-orbital is called the LUMO (lowest unoccupied molecular orbital). The energy difference between the HOMO and the LUMO is called the band gap. In semiconducting polymers for photovoltaic applications, the band gap has typically values below 3 eV and thus energy of visible light is high enough to move electrons from the valence band to the conduction band, creating mobile π-electrons along the polymer chain. Electrochemical doping resulting in creation of positive or negative charges along the conjugated system due to oxidation and reduction reactions, respectively, has shown to alter the conductivity in several orders of magnitude as well.[50] In addition to the intramolecular conduction along the conjugated system allow hopping processes intermolecular charge transport between neighbouring conjugated molecules.[51] This results in a charge transport capability over a macroscopic scale in the organic material.

1.6 Operating principle of hybrid solar cells

The absorber layer of hybrid solar cells consists of an electron donor component (conjugated polymers or small molecules) and an inorganic component as electron acceptor. This absorber layer is covered with two different electrodes, where one of the electrodes acts as transparent electrode, which is in the most cases a transparent conductive oxide (TCO) like indium tin oxide (ITO), fluorine-doped tin oxide (FTO) or aluminium-doped zinc oxide (AZO). The other one can be a simple metal electrode or also a transparent electrode if semi-transparency is intended.

The photocurrent generation of organic and hybrid solar cells can be summarized in a four step process; i.e. absorption of light (exciton generation), exciton diffusion, electron transfer and charge separation (Figure 1).

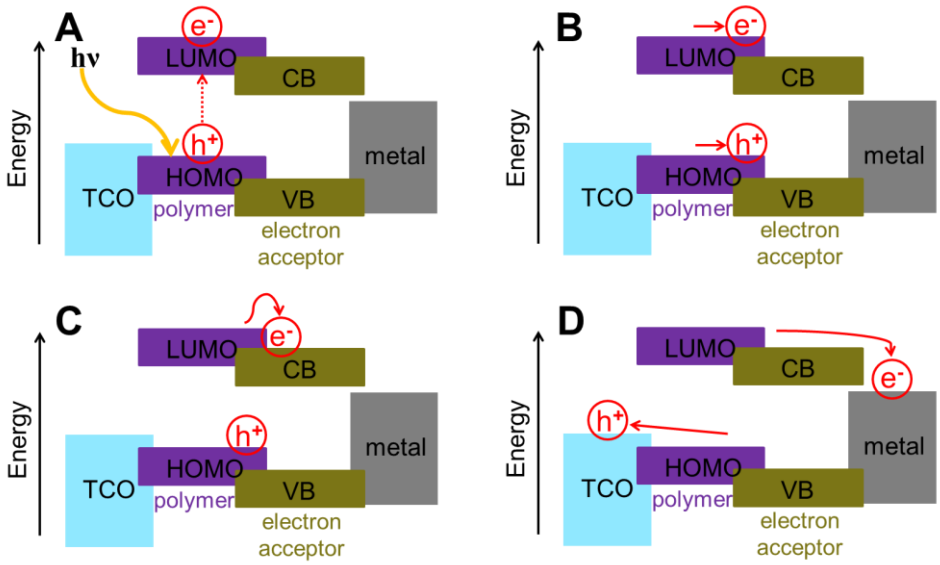

Figure 1: Schematic operating principle of hybrid solar cell (situation for exciton generation in the polymer): (A) absorption of light, (B) exciton diffusion, (C) electron transfer and (D) charge separation.

Upon absorption of photons with appropriate energy, electrons in the polymer get excited from their electronic ground state (HOMO) to their first excited state (LUMO) and an exciton is formed (Figure 1A). An exciton can be seen as a coulombically bound electron-hole pair. In organic semiconductors, typical exciton lifetimes are in the range of 100 picoseconds to 1 nanosecond before they recombine; this can be translated into an exciton diffusion distance on the order of 5-10 nm.[52] When diffusing excitons reach the interface to the inorganic nanoparticles (Figure 1B), electrons can be transferred to the conduction band (CB) of the CIS nanoparticles, while holes remain in the polymer (Figure 1C). This exciton dissociation (via electron transfer) is driven by the ionisation potential of the electron donor component and the electron affinity of the electron acceptor component. The relative energetic position of the LUMO of the donor material should be at least 0.3 eV higher than the conduction band of the acceptor component.[53] In contrast, too high differences cause thermalization losses, resulting in lowered voltages. In addition to the excitons formed in the polymer, charge carrier generation in the inorganic component also contributes to the photocurrent. In that case, holes created in the valence band (VB) of electron acceptor get filled with electrons from the HOMO of the donor-polymer.

The separated charges are still bound by Coulomb interactions and need to be separated. An internal electric field that is given when a semiconductor is sandwiched between

electrodes with different work functions accelerates the charges to the respective electrodes; i.e. electrons are accelerated to the electrode with the lower work function and holes are accelerated to the electrode with the higher work function (Figure 1D). This charge separation process depends in addition to the internal electric field also on temperature and on the local morphology.[54] After charge carriers are "collected" at the electrodes, they are passed into an outer circuit to generate the photocurrent.

1.7 Device architecture

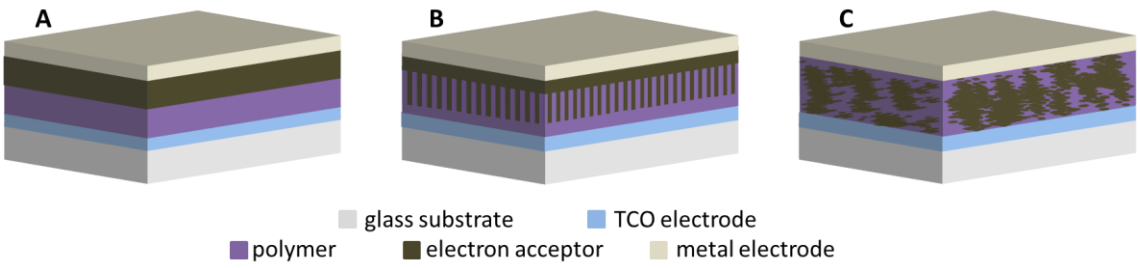

Figure 2: Schematic device layout of hybrid solar cells in (A) planar bilayer, (B) ordered nanostructured bilayer and (C) bulk-heterojunction architecture.

In the planar bilayer architecture (Figure 2A), electron donor and acceptor components are stacked as planar layers on top of each other. Since exciton diffusion length in semiconducting polymers is limited to a maximum length of about 10 nm,[52] only excitons created near the donor-acceptor interface may result in free charge carriers. This limits the effective absorber thickness in the planar bilayer architecture to a range, where light absorption gets too low for efficient solar cells. The relatively low interface area in bilayer architectures results in low current.

A possible way to increase the interface area is the introduction of structured layers. These structures can be columns or pyramids as shown in Figure 2B. Optimally the structure size lies in the range of exciton diffusion length to minimize exciton recombination. This is however difficult to obtain practically.

Another approach is the so called bulk-heterojunction architecture (Figure 2C). The concept of the bulk-heterojunction was first introduced in the field of organic

photovoltaics, where soluble fullerene derivates and soluble polymers have been coated from the same solution and the obtained films have showed domains in the nanometre regime forming a structure network of an internal donor-acceptor heterojunction.[34] There also exists several approaches that make the formation of hybrid bulk-heterojunction films for photovoltaic applications accessible.[55]

Nanomorphology in bulk-heterojunction solar cells plays a crucial role to maximize charge transport and minimize bulk recombination.[56] An optimum balance between a large amount of interfaces (for efficient exciton dissociation) and a suitable nanomorphology i.e. a bicontinous interpenetrating phase structure (for efficient charge transport) is needed.[57]

1.8 Electrical characterization

The electrical characterization of the solar cells is done by acquiring current-voltage (IV) curves under illumination and in the dark.

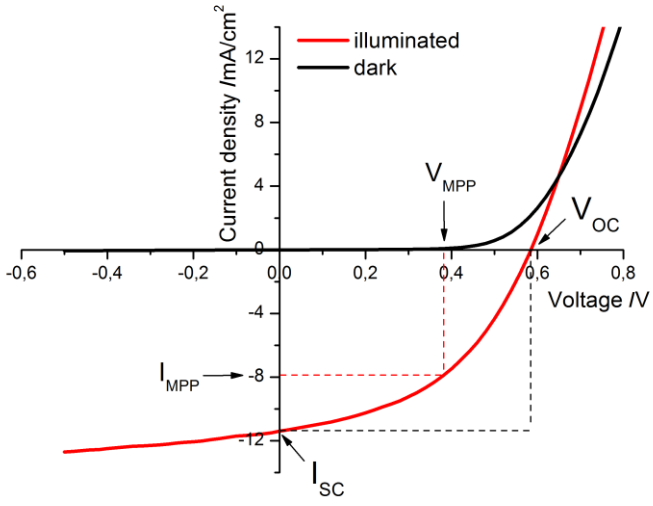

Figure 3: Current density vs. voltage curves of a solar cell under illumination and in the dark.

In the dark (Figure 3, black curve), the solar cell acts as a diode as it shows rectifying characteristics. In reverse bias (negative voltage applied on ITO), hardly any current occurs as the energy barrier is too high for electrons to be injected from the anode. In

forward bias electrons are injected from the energetically favoured cathode and current flows after a certain threshold is reached.

Under illumination (Figure 3, red curve) a photocurrent inside the solar cell occurs and current flows from cathode to the anode since even no external voltage is applied. The point where the IV-curve cuts the y-axis marks the short circuit current density (I_{SC}). (Situation for zero Ohm load, short circuit) The point, where the IV-curve under illumination cuts the x-axis marks the open circuit voltage (V_{OC}). At this point, the external applied voltage compensates the photocurrent. (Situation for infinite Ohm load, open circuit) The solar cell shows its maximum power output (P_{max}) at that point of the IV-curve where the product of voltage and current reaches its maximum – the so called maximum power point (mpp).

The power conversion efficiency (PCE) is defined as the ration of the power output (P_{OUT}) of the solar cell and the incident light intensity (P_{IN}).

$$PCE = \frac{P_{OUT}}{P_{IN}} = \frac{V_{mpp} * I_{mpp}}{P_{IN}} = \frac{V_{OC} * I_{SC} * FF}{P_{IN}}$$

$$FF = \frac{V_{mpp} * I_{mpp}}{V_{OC} * I_{SC}}$$

A further key parameter is the fill factor (FF) since it provides a measure for the performance of the device compared to its theoretical maximum. It is defined as the ratio of the maximum power output to the product of the open circuit voltage and the short circuit current. A low fill factor can be associated to a high degree of internal losses.

The characteristic of the solar cell under illumination can be approximately represented by an equivalent circuit, that of an imperfect current generator (Figure 4).[58]

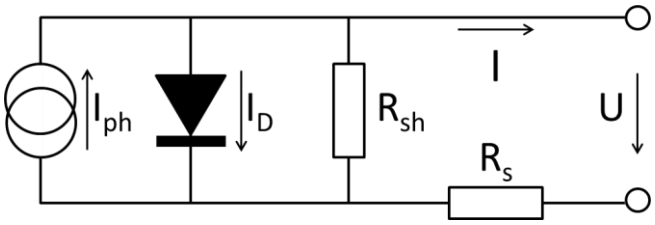

Figure 4: Equivalent circuit of a solar cell under illumination.

The basic structure of the solar cell in this case consists of a current source and a diode connected in parallel with opposite conducting direction. The shunt resistance R_{sh} detects shorts and material defects leading to leakage currents. It should therefore be as large as possible. In contrast, the series resistance R_s detects all transport resistances in the solar cell stemming from intrinsic semiconductor resistivity, electrode or interfacial layer resistivity or metal-organic interface barriers. In order to keep losses to a minimum, it must consequently be as small as possible.

R_s and R_{sh} can be extracted from IV-curves of the solar cell under illumination. R_s is given by the reciprocal value of the slope of the IV-curve at V_{OC} and R_{sh} is given by the reciprocal value of the slope at the I_{SC}.

The external quantum efficiency (EQE) or also called incident photon to current efficiency (IPCE) gives insights into the spectral contribution of light onto the photocurrent. The EQE is defined as the ratio of the number of generated electrons to the number of incident photons under short circuit conditions and is usually given as percentage. The EQE of a solar cell is collected under monochromatic light and plotted against the wavelength. Effects of optical losses such as transmission through the cell and reflection of light away for the cell are not considered.

$$EQE = \eta_A * \eta_{diff} * \eta_{diss} * \eta_{tr} * \eta_{cc}$$

The EQE is determined by the efficiency of the product of five consecutive steps: η_A is the photon absorption yield, determined by the absorption coefficient and the thickness of the absorber layer; η_{diff} is the exciton diffusion yield and represents the ability of excitons to diffuse through the material without recombination; η_{diss} is the exciton dissociation yield and represents the probability that holes and electrons get separated by the internal electric field at the donor-acceptor interface; η_{tr} is the charge carrier

transport yield and is limited by the charge carrier mobilities of the semiconductors and η_{cc} is the charge collection yield and represents the ability of the charges to be transferred from the absorber layer to the electrodes. The most limiting processes in the photogeneration of free charge carriers in OPV are believed to be recombination of excitons prior to dissociation, lowering η_{diff} and losses during the charge transport of holes and electrons, lowering η_{tr}.[59]

$$I_{SC} = \frac{q}{h * c} \int_{\lambda_{min}}^{\lambda_{max}} EQE(\lambda) * P_{AM1.5G}(\lambda) * \lambda * d\lambda$$

The I_{SC} of the solar cell can be expressed as a function of the integrated wavelength dependent EQE over the irradiation intensity of the light source according to the equation above.

A reference light source spectrum is given by the sun under a solar zenith angle of 48.2°, defined as AM1.5G, representing the overall yearly average spectrum at mid-latitudes.[60] At this incident angle the incoming photons have to pass 1.5 times the atmosphere (air mass, AM), where the extraterrestrial sunlight (AM0) is attenuated by scattering and absorption. The reference spectra of extraterrestrial sunlight (AM0 – ASTM E490) and under global AM1.5G conditions (ASTM G173) are given in Figure 5; data derived from Ref. 61.

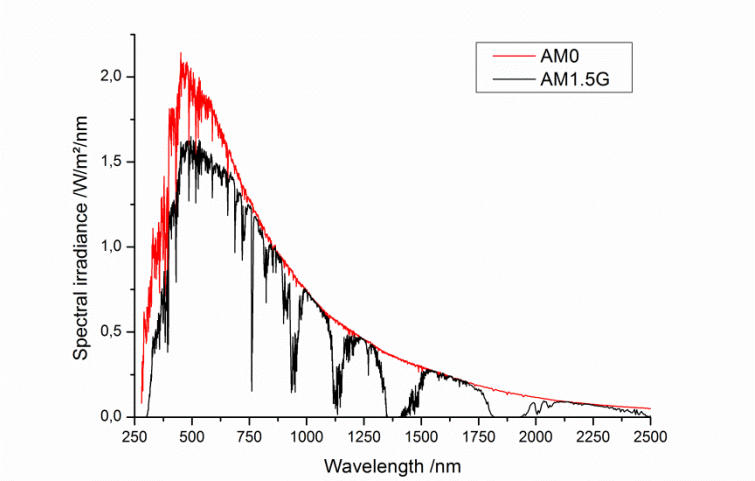

Figure 5: Standard solar spectra for extraterrestrial, AM0 (red curve) and terrestrial use, AM1.5G (black curve); data derived from Ref. 61

1.9 Stability of organic photovoltaics

With raising power conversion efficiencies of organic and hybrid solar cells in the last ten years, the long term stability of these devices became more and more a research topic and has to be addressed for the success of new photovoltaic technologies.[62]

Three main requirements are essential for the commercialization of cost-effective photovoltaic systems, i.e. the minimization of system cost, the maximization of initial performance and the minimization of loss in performance over time.[63]

The comparison with the market launch of a familiar organic optoelectronic device, namely the organic light emitting diode (OLED) points out, that lifetime and stability are major issues for all organic electronic technologies.

Classical inorganic silicon solar cells are offered by the majority of manufacturers with a 20 up to 25 years solar panel warranty. Under the assumption that the manufacturing costs in terms of costs per Watt peak of novel solar cell techniques can be lowered to a quarter of that of existing silicon cells, at least lifetimes in the order of five years should be granted to equal profitability.[64]

In the case of crystalline silicon solar cells, limited research about intrinsic stability has been done; the focus has been on extrinsic failure paths such as corrosion of electrical connections (solder joints, busbars and other interconnects) or degradation of encapsulation material what may lead to limiting transmittance for incoming light.[65,66] The situation changed for thin film solar cells like a-Si, CdTe, and CIGS solar cells.[67] New problems like corrosion of transparent conductive electrode material[68] or hot spots caused by shunts due to non-uniformities of the absorber layer[69] have been reported. In the case of amorphous silicon solar cells for example, a light induced degradation of cell performance has been observed – the so called Staebler-Wronski effect.[70]

With the introduction of organic materials as solar cell components, totally new aspects concerning the long term stability become an issue. Failure modes of inorganic solar cells may not be applicable to organic or hybrid photovoltaics. Organic solar cells present an enormous variability in all aspects and the most complex degradation phenomena and therefore the number of publications regarding degradation far exceeds all the other solar cell technologies.[71]

However, a comparison of obtained results concerning device stability performed under different testing conditions at different laboratories seems to be problematic.

The International Electrotechnical Committee (IEC), an international standardization organization, sets specific norms for the design qualification and type approval of photovoltaic modules. There exist norms for crystalline silicon terrestrial PV modules (IEC 61215) and adapted moderated norms for thin-film terrestrial photovoltaic PV modules (IEC 61646) that take possible instabilities of this technology into account. For organic or hybrid solar cells no such norms exist till now.

Therefore, annual International Summits on Organic Photovoltaic Stability (ISOS) are held since 2008 to aid the community in creating standards for the lifetime assessment of organic photovoltaic devices. ISOS documents have been published that offer a set of recommendations to provide some general measurement practices and guidelines for the determination and reporting of stability data of OPVs allowing other laboratories to duplicate and compare results.[72] The testing procedures are divided into shelf life testing (ISOS-D), outdoor testing (ISOS-O), laboratory weathering testing (ISOS-L), thermal cycling testing (ISOS-T) and solar-thermal-humidity cycling (ISOS-LT).
To meet the capabilities of a wider range of laboratories, each type of these testing regimes can be conducted at three levels depending on available equipment: Basic (Level 1), Intermediate (Level 2) and Advanced (Level 3). The ISOS documents are envisaged to serve as a basis for future standards that are used throughout the community.

The lifetime of photovoltaic devices is commonly defined as the time when the solar cell performance has degraded to 80% of its initial performance. However, just reporting time for reaching that point does not give much information of the ageing behaviour of the device unless the general shape of the efficiency decay pattern is known. Some devices show a linear decay curve over time, some show an increase in efficiency before they degrade; more often a rapid initial degradation is observed (the so called burn-in period) followed by a more stable, slower degradation rate. In this case it is allowed to apply an alternative definition of device lifetime (Figure 6).

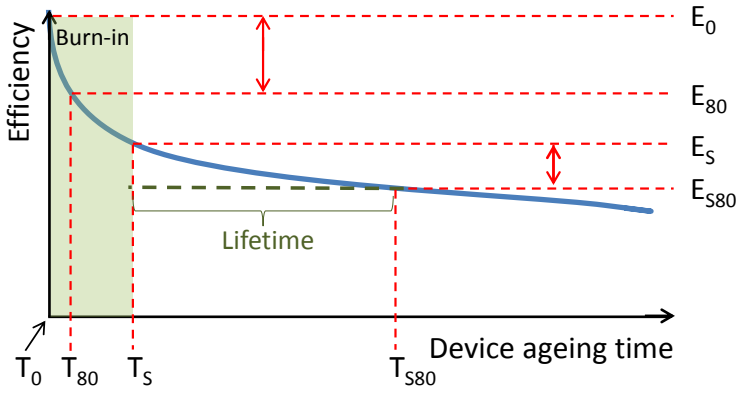

Figure 6: Typical decay curve of an organic solar cell (solid blue line). Lifetime (green dashed line) represents a 20% loss from cell efficiency after its burn-in period.

According to the ISOS guidelines, four pairs of parameters are needed to define the device decay pattern. E_0 marks the device efficiency direct after fabrication at the time t=0 (T_0). E_{80} marks the 20% loss of initial efficiency. This point is reached after a certain time (T_{80}). E_S marks the device efficiency at the start of the stabilized section after burn-in period, where the degradation rate becomes almost constant. This point is defined arbitrarily by the user at the time T_S. T_{S80} is the time when the device performance reaches 80% of E_S (E_{S80}). This time is commonly translated into device lifetime.[73]

It is absolutely important to know and document the incident light intensity, the spectrum of the incident light, the manner of illumination (i.e. continuous or only during collecting IV-curves), the temperature of the device during the experiment and the atmosphere (i.e. humidity and oxygen content if the experiment was not carried out in air).

Furthermore the ISOS initiative conducted inter-laboratory stability studies to reach a consensus on organic solar cell performance. The first round robin study was conducted 2009 and 18 different laboratories from Northern America, Europe and Middle East participated.[74] In a second round robin study 2011, 24 laboratories from 10 countries and across four different continents have been involved.[75] In 2014 a further round robin study among 46 laboratories worldwide has been published.[76]

While already tremendous work has been done to increase the stability and lifetime of organic solar cells only limited information dealing with stability issues of hybrid solar cells can be found in literature.[77,78,79,80,81,82,83]

2. State of the art in the field of polymer-$CuInS_2$ hybrid solar cells and aim of this thesis

The concept of the CIS-polymer hybrid solar cell has been introduced by the Linz Institute for Organic Solar Cells (LIOS). At early stages, CIS-nanoparticles have been synthesized by a thermal decomposition method and extensive nanoparticle growth has been controlled with the use of capping ligands. In a next step the nanoparticles and the polymer have been combined and coated from the same solution. Hybrid solar cells fabricated according this strategy showed significantly better photovoltaic response in comparison to polymer single layer solar cells; however, a relative low I_{SC} in the range of 0.3 mA/cm² has been obtained.[84]

The concept of the polymer-CIS hybrid solar cell has been carried forward at Graz University of Technology. A significant improvement in terms of photovoltaic performance could be achieved with a novel route for the direct formation of CIS nanoparticles within the polymer matrix.[85] A mixture of precursor chemicals for the formation of CIS (i.e inorganic copper and indium salts and thiourea as sulphur source) and a semiconducting polymer gets dissolved together and coated on a substrate. During a moderate thermal annealing step the precursor chemicals are decomposed into CIS and a hybrid nanocomposite layer is obtained. No additional nanoparticles-capping ligands have been needed; the polymer acts as capping agent and thus prevents extensive particle growth. The in-situ synthesis route for nanoscaled inorganic–organic semiconductor composite layers by converting metal salts and thiourea directly in the polymer–matrix into inorganic metal sulfides has also been successfully applied for CdS, PbS, and ZnS.[85]

As melamine as side product during the decomposition of thiourea seemed to hinder device performance,[77] alternative precursors for the preparation of CIS have been evaluated. The introduction of metal carbamates and metal xanthates allowed the formation of CIS without an additional sulphur source. Various organic alkyl moieties at the carbamates and xanthates have been tested and rigorous optimisation of the copper-indium ratio, polymer-inorganic ratio as well as device fabrication technique has been done. During the thermal decomposition of metal xanthates for the formation of CIS nanoparticles in the polymer layer only volatile decomposition byproducts occur that do not remain in the nanocomposite layer.

The usage of metal xanthates for CIS formation in combination with the low bandgap polymer poly[2,1,3-benzothiadiazole-4,7-diyl-2,5-thiophenediyl-(9,9-dioctyl-9H-9-silafluorene-2,7-diyl)-2,5-thiophenediyl] (PSiFDBT) led to a published cell efficiency of 2.8%; however, the operating stability of these hybrid solar cells was an issue.[49]

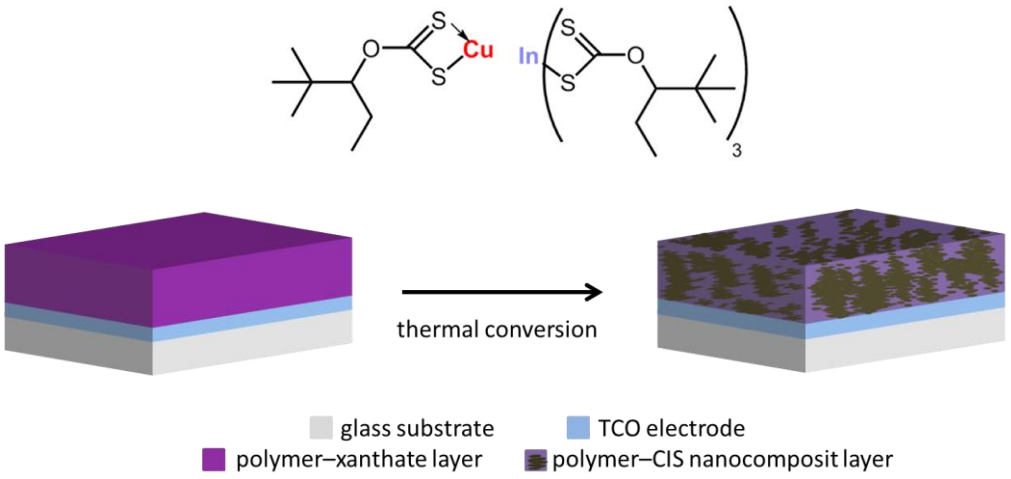

Figure 7: Chemical structures of copper- and indium-*O*-2,2-dimethylpentan-3-yl dithiocarbonate and schematic in-situ formation of the acceptor phase ($CuInS_2$) from copper and indium xanthates within the donor matrix.

In Figure 7 the chemical structures of copper- and indium-*O*-2,2-dimethylpentan-3-yl dithiocarbonate and the schematical *in-situ* formation of the CIS acceptor phase from the xanthates within the polymer matrix, forming a nanostructured bulk-heterojunction, are presented.

Several diploma theses and doctoral theses have investigated the polymer-CIS hybrid solar cell in the frame of the Christian Doppler Labor (CDL) für Nanokomposit Solarzellen.[86,87,88,89,90,91,92,93,94,95]

In the work of Eugen Meier[96] an automated multichannel measuring system for organic and hybrid solar cells has been planned and assembled and first stability test of polymer-PCBM and polymer-CIS devices have been conducted. The investigated polymers in this study have been poly(*p*-phenylen-vinylen) (PPV), poly[2-methoxy-5-(2-ethylhexyloxy)-1,4-phenylenevinylene] (MEH-PPV), poly[2-methoxy-5-(3′,7′-dimethyloctyloxy)-1,4-phenylenevinylene] (MDMO-PPV) and poly[(9,9-dioctylfluorenyl-2,7-diyl)-*co*-bithiophene] **(**F8T2).

In parallel works during this thesis, the influence of a thin silver cathode interlayer on the performance of hybrid photovoltaic cells,[97] polymer-nanoparticle hybrid solar cells in tandem architecture[98] and flexible polymer-CIS hybrid solar cells and modules[99] have been realized.

The main aim of this thesis was to get insights into stability limiting parameters and reasons for device degradation of in-situ prepared polymer-CIS hybrid solar cells and to develop and evaluate strategies to improve their long-term stability. For that purpose, hybrid solar cells had to be fabricated, characterized and the characteristic electric parameters have been monitored over time. In the next step, the goal was to stabilize the solar cells via introduction of more stable materials or the introduction of additional interlayers while keeping cell efficiencies at high level. Furthermore, possibilities for stabilization via an appropriate encapsulation to prevent oxidative degradation of the absorber layer had to be evaluated.

In the second part of this work, the aim was focused on ordered nanostructured hybrid solar cells. It was to examine if nanoimprint lithography (NIL) is applicable for structuring low-bandgap polymer layers to obtain a large surface area. As the conversion of the metal xanthates occurs at temperatures above 150°C, the target was to examine the thermal stability of the nanostructures in the polymer layer. In the following, the infiltration of the NIL-structured polymer layer with metal xanthates for the formation of the metal sulfide phase had to be realized and the influence of these structures on device performance had to be investigated.

3. Results and discussion

3.1 Determine status quo in stability of PSiFDBT-CIS hybrid solar cells

Hybrid solar cells in the architecture glass|ITO|PEDOT:PSS|PSiFDBT-CIS|Al have been fabricated according to the in-situ route using copper and indium xanthates as precursors for the CIS phase.[49] The chemical structures of PSiFDBT and copper and indium xanthates are given in Figure 8 and Figure 7, respectively. A detailed description of the solar cell fabrication can be found in the experimental part.

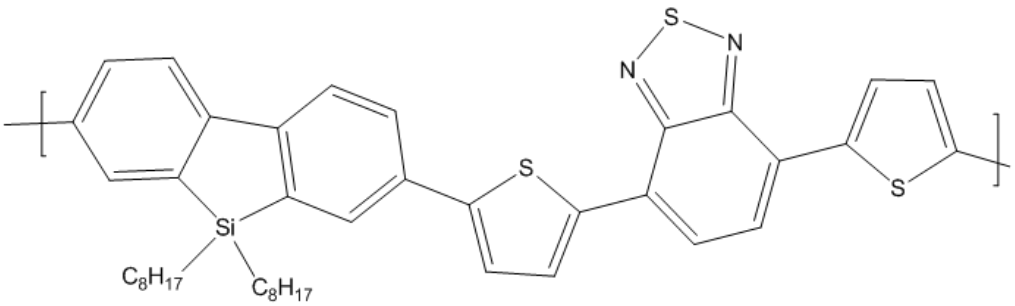

Figure 8: Chemical structure of PSiFDBT - Poly[2,1,3-benzothiadiazole-4,7-diyl-2,5-thiophenediyl-(9,9-dioctyl-9H-9-silafluorene-2,7-diyl)-2,5-thiophenediyl].

The device consists of a ~60-90 nm PSiFDBT-CIS bulk heterojunction absorber layer sandwiched between an 150-200 nm ITO anode in combination with a ~40 nm poly(3,4-ethylene-dioxythiophene)-poly(styrenesulfonate) (PEDOT:PSS) interlayer on a glass substrate and an ~200 nm aluminum cathode. The PEDOT:PSS layer acts as smoothening layer, promotes the adhesion of further coatings and lowers the Fermi level of the anode. A schematic presentation of the device architecture can be seen in Figure 9.

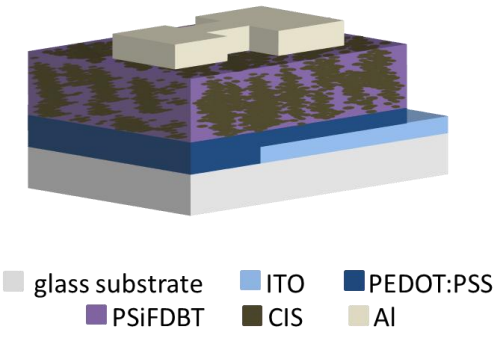

Figure 9: Schematic device architecture of a PSiFDBT-CIS hybrid solar cell.

Figure 10 shows IV-curves obtained from measurements inside a nitrogen filled glovebox direct after fabrication under illumination and in the dark. The solar cell exhibits a V_{OC} of 530 mV, an I_{SC} of 10.5 mA/cm² and a FF of 49.2%, leading to a PCE of 2.74%.

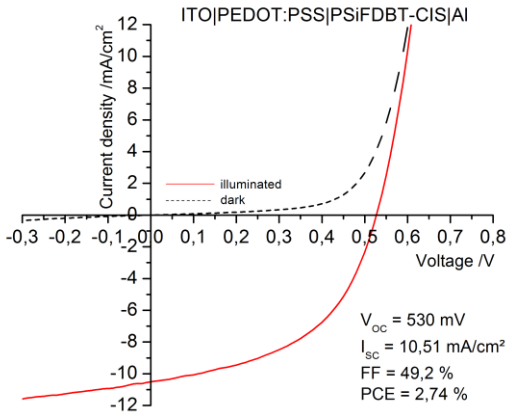

Figure 10: IV-curves of a PSiFDBT-CIS hybrid solar cell obtained from a measurement inside a glovebox under illumination and in the dark.

Immediately, after the initial electrical characterization inside the glovebox, selected solar cells have been transferred into air and their performance under continuous illumination over time has been evaluated. For that purpose, additional electrical connectors have been attached on the ITO- and the evaporated metal-electrode respectively. IV-curves of the device have been collected every 15 minutes and the cells have been kept in open circuit condition in between the measurements. No additional cooling was applied during the stability tests, resulting in a device temperature of approximately 55°C under illumination.

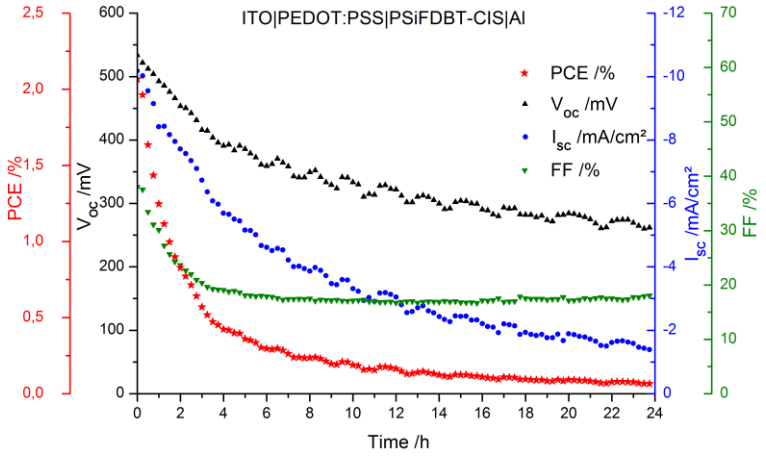

Figure 11: Decay pattern for the PCE, the V_{OC}, the I_{SC} and the FF of a PSiFDBT-CIS hybrid solar cell (with aluminum cathode) over time in air.

Figure 11 shows a typical decay pattern for the PCE, the V_{OC}, the I_{SC} and the FF of the solar cell under permanent illumination (100 mW/cm²) in air over time. Starting from 2.1%, PCE drops dramatically in the first hours of operation in air. T_{80} is reached within the third measuring point, after 30 minutes. After 9 hours, the solar cell only shows 1/10 of its initial performance. I_{SC} decreases from 10.2 mA/cm² to 3.5 mA/cm² and V_{OC} decreases from 534 mV to ~350 mV during that time. The FF decreases significantly in the first testing hours from 38% to ~20% and stays constant for the rest of the testing period. The FF already decreased from 49%, obtained from measurements inside the glovebox, to 38% indicating that first degradation already occurred in the time between the two measurements.

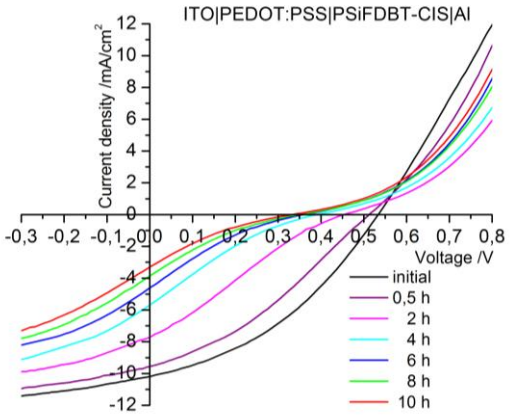

Figure 12: Representative IV-curves during the ageing experiment of a PSiFDBT-CIS hybrid solar cell with an aluminum cathode.

In Figure 12 representative IV-curves during the testing period are presented. R_s increases with increasing illumination time, indicating a hindered charge transport or extraction, possibly due to photo-oxidation of the absorber layer or the formation of an insulating oxide layer between the absorber layer and the aluminum cathode. R_{sh} and the FF decrease with increasing illumination time, indicating enhanced charge recombination processes.

3.2 Possible reasons for weak stability

Except the acceptor material, the device architecture and working principle of hybrid solar cells are quite similar to the widely investigated organic solar cells and therefore, concepts and scientific achievements, which positively influence device performance and stability, can be adapted for the fabrication of stable hybrid solar cells to some extent. For organic solar cells with the architecture ITO|PEDOT:PSS|absorber-layer|Al several potential instabilities and various degradation processes have been described in literature. Selected works concerning the stability of similar devices or even the same device components are summarized in the next paragraphs.

3.2.1 Anode degradation

ITO|PEDOT:PSS is the most commonly used combination as an anode in organic solar cells in regular architecture.[100]

Concerning the stability of ITO itself, it was found that the resistance increases with time under outdoor exposure and accelerated ageing conditions. Water absorption at the grain boundaries increases carrier scatter and therefore resistance but the optical properties are not affected.[101] In addition, the poor mechanical properties of ITO are in discussion. The thin layers possibly do not withstand extensive bending in the case of flexible solar cells. Crack formation and its propagation may increase the sheet resistivity, what results in hindered charge transport.[102] In comparison with alternative TCOs, it was found that FTO is the most stable material, followed by ITO, whereas AZO is extremely susceptible to environmental degradation.

Due to the hydrophilic and hygroscopic nature, PEDOT:PSS is often seen to be the cause of device failure and degradation.[103] The intake of water may result in swelling of the interlayer and as a consequence to a lowered conductivity of the films or

delamination of the device.[100,104] Moreover, it is believed that PEDOT:PSS attracts ambient humidity and enables its diffusion under the electrodes, followed by the release of this absorbed water towards the highly reactive metal cathode leading to a rapid oxidation of the cathode.[105] Additionally, the high acidity of water-based PEDOT:PSS formulations is suspected to be a further factor for degradation as accelerated corrosion of the ITO electrode has been observed. It favours the etching of indium atoms out of the ITO layer; this was first demonstrated for polymer light emitting diodes.[106] Diffused indium atoms have also been detected in the absorber layer of organic solar cells.[107] However, a direct lifetime limiting influence is not proved. As a consequence, more pH-neutral derivates[108] have been developed or the polymeric interlayer has been substituted by various metal oxides[109,110] that show a similar work function to PEDOT:PSS.

As an organic component, PEDOT:PSS can be easily oxidized. Norrman et al. found, that oxygen reacts mainly with PEDOT, and as a consequence, the PEDOT phase separates from the PSS phase.[111]

3.2.2 Absorber layer degradation

The semiconducting polymer can be photo-oxidized resulting in loss of conjugation or chain scission. This in consequence leads to bleaching of the polymer and to a loss of its semiconducting properties. Carbonyl groups that are formed as a result of oxidation may act as very efficient exciton quenchers.[112] It is believed that formation of reactive singlet oxygen and subsequent oxidation of organic compounds is responsible for oxidative degradation. A scheme of polymer sensitized singlet oxygen formation is given in Figure 13.

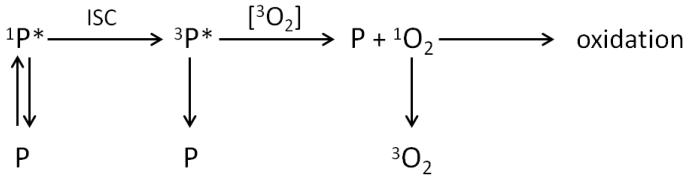

Figure 13: Scheme of polymer sensitized singlet oxygen formation according to Hintz et al.[113]

Upon absorption of light the singlet excited state is formed in the polymer. Via intersystem crossing (ISC) a triplet state may be formed from its singlet excited state if no relaxation or charge transfer occurs. This triplet state can decay spontaneously to the ground state or it can be quenched by oxygen in its ground state forming a reactive singlet oxygen species, followed by singlet oxygen deactivation via chemical reaction.[113] Blending polymers (or small molecule donor materials) with electron acceptors slows the bleaching rate as production of singlet O_2 is suppressed.[114,115]

However, due to the low triplet quantum yield of polythiophenes, singlet oxygen sensitization by triplet states of polythiophenes seems unlikely. Alternatively, it is speculated that singlet oxygen may be formed on dissociation of the excited state of reversible charge transfer complexes between oxygen and polythiophenes (Figure 14).[131]

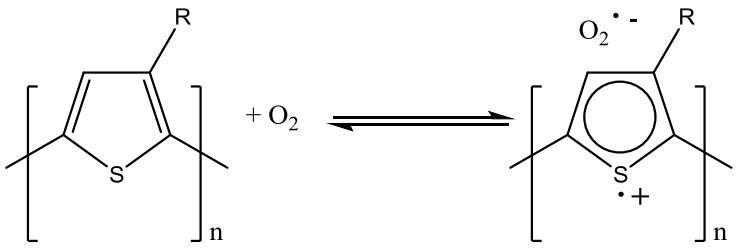

Figure 14: Reversible formation of a charge transfer complex between P3HT and O_2 according to Abdou et al.[116]

This charge transfer complex acts as a precursor for formation of a charge pair consisting of a positively charged radical cation on the polymer chain in combination with $O_2^{\cdot -}$.[117] Aguirre et al. also performed electron spin resonance (ESR) spectroscopy and found that illumination of π-conjugated polymers in the presence of air leads to formation of persistent radical cations on the polymer chain.[118] However, it is not clear that the generated $O_2^{\cdot -}$ directly initiates a radical chain reaction leading to large scale degradation.

It is known, that simple thiophenes react with oxygen even at low temperatures under irradiation to form thioozonides that undergo further degradation as shown in Figure 15.[119]

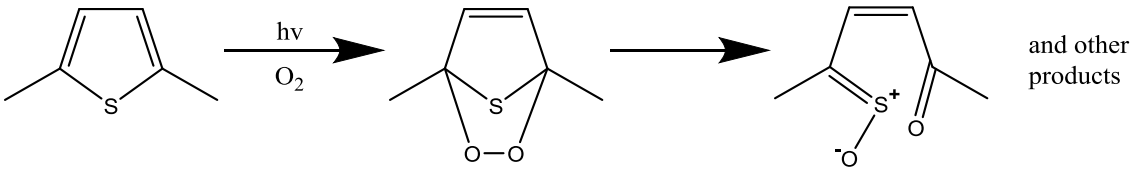

Figure 15: Thioozonide formation from 2,5-dimethylthiophene and oxygen and subsequent decomposition into an S-oxide and other products.

Moreover, the transformation of oxygen into a super oxide anion ($O_2^{\bullet -}$) trough electron transfer by a fullerene radical anion ($C_{60}^{\bullet -}$) was proved by ESR measurements[120] and a subsequent degradation of blend materials by attack of $O_2^{\bullet -}$ seems possible.

The initially popular PPV-type polymers such as MEH-PPV and MDMO-PPV are known to be highly unstable and sensitive to chemical attacks and devices typically degraded significantly in a matter of minutes to hours under 1000 W/m^2 illumination in ambient atmosphere.[114] Polythiophenes as well as low-bandgap polymers have shown to be much less sensitive to moisture and oxygen and allowed even better photovoltaic conversion efficiencies, however, devices based on this material are also susceptible to chemical degradation.[121]

Manceau et al.[122] have studied the photochemical stability of various common π-conjugated polymers for organic solar cells and found that the use of exocyclic double bonds in the main backbone (as present in MEH–PPV or MDMO–PPV) leads to a poor stability and should be avoided, furthermore, the presence of readily cleavable bonds (such as C–N or C–O) is problematic concerning their stability whereas aromatic polycyclic units generally exhibit a good photochemical stability.

It has been shown that the aliphatic side-chains that are introduced to provide enhanced solubility have a negative influence on the polymer photochemical stability[122] and thus their functionalization[123] or cleavage (via a thermal step after deposition)[124] improves stability.

Manceau et al.[125] further showed for P3HT that photochemical oxidation of the alkyl side chain occurs (Figure 16).

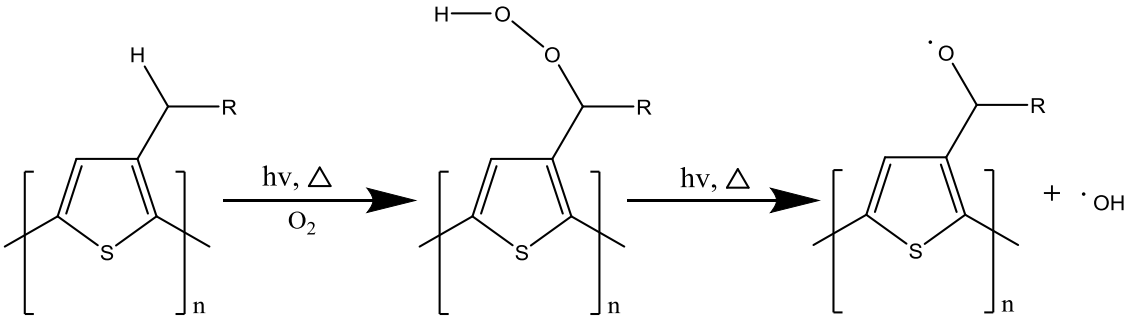

Figure 16: Photochemical oxidation of a P3HT side chain according to Manceau et al.[125]

In a first step, the formation of α-unsaturated hydroperoxides has been observed followed by a photochemical and thermal decomposition of the hydroperoxides yielding alkoxy and hydroxyl radicals. According to their infrared spectroscopy studies, these hydroxyl radicals may further react with the sulphur atoms of the thiophene ring forming sulfoxides and sulfones (Figure 17) that are possibly later decomposed into sulfinate esters.

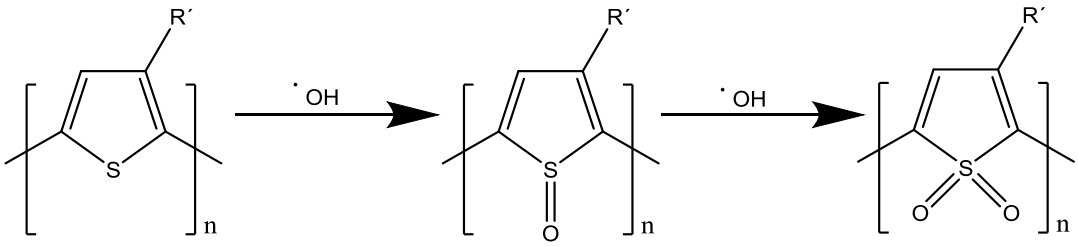

Figure 17: Oxidation mechanism of the sulphur atom in thiophene ring according to Manceau et al.[125]

Additional considerations cover the physical degradation of the morphology of the bulk-heterojunction nanostructure. Bulk-heterojunction thin films prepared by spin coating are not thermodynamically stable as morphologies are kinetically trapped in a metastable state and will tend to evolve toward phase separation.[59] It has been shown, that cross linking the polymer inhibits fullerene aggregation dramatically and thus enhances the lifetime of the devices.[126] Berto et al. studied the morphological and photovoltaic stability of bulk heterojunction polymer-fullerene solar cells by the means of transmission electron microscopy (TEM) and demonstrated that morphology changes are strongly related to the glass transition temperature of the matrix polymer.

3.2.3 Cathode degradation

In regular device architecture typically “low” work function metals are used for electron extraction to obtain a high internal electric field with respect to the transparent “high” work function ITO-counter electrode. These metals are, however, easily oxidized resulting in electrically insulating interfaces and limited charge extraction of the devices. Oxidation of aluminum already occurs during the vacuum deposition process of the material by traces of oxygen and water.[127] Hermenau et al.[128] studied the ageing of small molecule organic solar cells with aluminum electrodes using X-ray photoelectron spectroscopy (XPS) and time-of-flight secondary ion mass spectrometry (TOF-SIMS) in conjunction with isotopically labeled H_2O and O_2. Their findings point out that one of the most significant degradation mechanisms is diffusion of water through the aluminum electrode resulting in massive formation of aluminum oxide. They also found that water forms undesirable aluminum oxide to a greater extent than molecular oxygen and illumination is observed to impede the aluminum oxide formation, which is proposed to be a temperature effect. In general Al_2O_3 formation deteriorates the absorber layer – electrode interface, what results in hindered charge extraction and may lead to electrode delamination.

Various degradation processes take place simultaneously and degradation mechanisms are catalyzed or accelerated by high light intensities and elevated temperatures. Local electrical shorts and electrical stress caused for instance by shading of the device may lead to hot spots, resulting in degradation of the system. Furthermore, charged molecules at metal-organic interfaces are expected to be more reactive than the bulk materials.[127]

3.3 Photo-bleaching

In Figure 18A, the photo-bleaching of an 60 nm absorber layer of a PSiFDBT-CIS hybrid solar cell, deposited on a 40 nm PEDOT:PSS anode interlayer under 100 mW/cm² illumination (sulpur plasma lamp) in air is demonstrated. Spectra have been recorded against glass|ITO, divergent reflectance due to additional layers as well as scattering has not been considered.

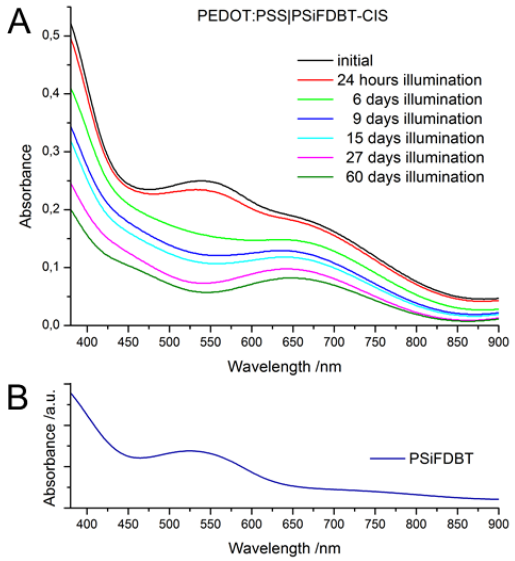

Figure 18: Time evolution of absorbance spectra of the absorber layer of a nanocomposite solar cell in air under 1 sun illumination (A) and an absorbance spectrum of a PSiFDBT-thin film (B).

In the absorbance of the pristine nanocomposite stack (Figure 18A, black curve) a local absorption maximum around 535 nm is observable, stemming from PSiFDBT as can be seen from an absorbance spectrum of a thin PSiFDBT film that has measured at the same conditions (Figure 18B). After 24 hours of illumination (Figure 18A, red curve), the absorbance of the absorber layer is already slightly reduced, while showing its main loss around the polymer peak. However, this peak is still clearly identifiable and overall absorption loss is not in an extent that explains a nearly complete loss in PCE. After 6 days of illumination, no peak around this wavelength region is observable any longer, indicating that the polymer has lost its typically chromophores due to oxidative photo-bleaching. It has to be noted, that the bleaching experiment has been carried out on the absorber layer without the metal electrode that may act as additional protective layer against diffusion of oxygen and humidity when deposited on the hybrid stack and thus slows down the beaching rate.

3.4 Stability under oxygen and water free environment

To evaluate the stability of hybrid solar cells under oxygen and water free environment, direct after fabrication solar cells have been transferred into a measuring chamber with an integrated quartz glass window to keep the devices under inert gas and characteristic electric parameters have been monitored over time under permanent illumination. The setup allowed the simultaneous monitoring of two individual solar cells.

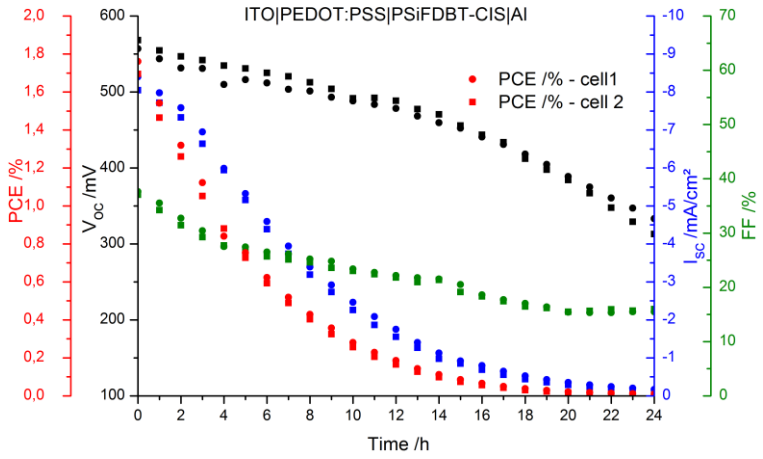

Figure 19: Characteristic parameters (PCE, V_{OC}, I_{SC}, FF) over time of two nanocomposite solar cells in an inert gas chamber under continuous illumination (P_{in} was 100 mW/cm^2).

Figure 19 shows characteristic parameters (PCE, V_{OC}, I_{SC}, FF) over time of two nanocomposite solar cells with aluminum electrodes in an inert gas chamber under continuous illumination. It can be seen, that even under the absence of oxygen and water degrade the devices within hours. Similar to the results obtained without encapsulation (see Figure 11), the I_{SC} is primarily responsible for device malfunction.

During the experiment, the content of oxygen and water inside the measuring chamber has not been monitored, nevertheless, similar results have been obtained while measuring the solar cell characteristics over time inside a nitrogen filled glovebox, where oxygen and water content have been monitored and kept below 1 ppm respectively.

Zhao et al.[129] carried out in-situ impedance spectroscopy studies on organic solar cells with the architecture ITO|PEDOT:PSS|P3HT-PCBM|Al. Their study confirmed that the degradation starts at the initial stage of device fabrication even inside a glove box with

ppm levels of oxygen. They concluded that one degradation process takes place at the interface of P3HT and PCBM and the other can be linked to the interface of the absorber layer and the metal electrode, involving the formation of Al_2O_3.

However, due to the weak stability of organic solar cells with aluminium electrodes even under oxygen and water free environment, an additional issue is in discussion. At the metal-blend interface, organometallic compounds may be formed during the deposition of the metal electrode.[127] XPS studies of PPV on aluminium reveal the formation of a 3 nm thick insulating layer that is believed to be formed as aluminium atoms diffuse into the polymer layer and react with the vinyl groups, resulting in disruption of conjugation and in formation of an increased electron injection barrier.[30] Lögdlund et al.[130] have carried out theoretical investigations of a PPV-aluminium interface and propose a direct formation of Al-C bonds as shown in Figure 20.

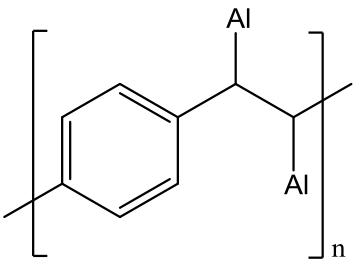

Figure 20: Proposed structure of Al-C bonds at the PPV-Al interface according to Lögdlund et al.[130]

Organo-aluminium compounds itself are highly reactive species too, that will react with any proton donors present or oxygen.[131] Krebs et al. assume that radical species formed in the absorber layer may react with the aluminium electrode, leading to a gradual deterioration of the absorber layer - electrode interface quality.[132]

3.5 Replacement of selective components

According to the motto “The chain is as strong as its weakest link”, the functional failure of a single component may lead to the failure of the complete device. To get insights to the influence of single components of the complete device architecture on solar cell stability, selective parts have been replaced into presumably more stable ones. The focus in this series of experiments was rather the comparison of different materials in solar cells that have been prepared at similar conditions, ideally in parallel from one chemical batch, than making extensive optimization of one material combination to achieve maximum efficiencies.

3.5.1 Replacement of aluminum as cathode material

Among all possible weak points, the instabilities according to active layer – cathode interface seems to be the most critical issue (especially in the case of aluminum electrodes). The replacement of the cathode material appears to be the most straightforward approach while keeping all processing conditions unchanged during device fabrication except evaporation of metal electrodes. For that reason aluminum has been replaced with silver and the influence on device performance and stability has been examined.

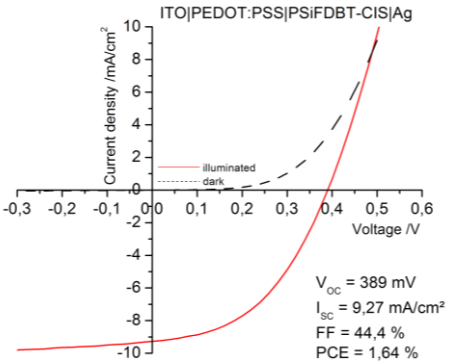

Figure 21: IV-curves of a PSiFDBT-CIS hybrid solar cell with a silver electrode under illumination and in the dark.

While showing similar values in I_{SC} and FF (Figure 21), the open circuit voltages of the solar cells with silver electrodes of typically 380-400 mV are significantly lower than those of solar cells with aluminum electrodes that are in the range of 500-540 mV.

This can be explained with the less favored work function of silver that is in the range of 4.52-4.74 eV[133] in respect with PEDOT:PSS compared to aluminum that is in the range of 4.06-4.26 eV,[133] resulting in a lowered internal electric field.

Figure 22 shows the energetically positions of the HOMO and the LUMO from PEDOT:PSS,[134,135] PSiFDBT[136] and CIS[137] as well as the Fermi level of the electrodes.[133,138]

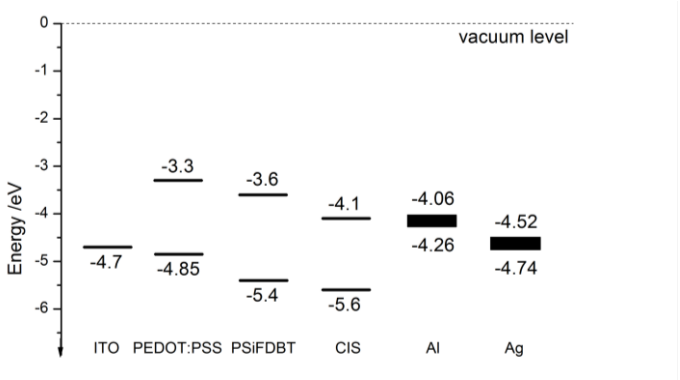

Figure 22: HOMO and LUMO level from PEDOT:PSS, PSiFDBT and CIS as well as Fermi level of the electrodes. Values taken from Ref. 133, 134, 135, 138, 137, 138.

PSiF-DBT has its HOMO at -5.4 eV and its LUMO at -3.6 eV and thus theoretically matching to CIS as electron acceptor that has its HOMO at -5.6 eV and its LUMO at -4.1 eV. PEDOT:PSS has its HOMO at -4.85 eV,[134] thus lowering the Fermi level of the ITO anode that has a value of -4.7 eV[138] and its LUMO at -3.3 eV,[135] thus acting as efficient electron blocking layer. The potential difference between the electrodes is lower in the case of Ag as cathode material, resulting in lowered V_{OC} values.

In terms of stability of devices with Ag electrodes, it can be seen from Figure 21 and Figure 23 that the V_{OC} obtained during the first IV-curve in air dropped significantly from 389 mV to 308 mV, lowering the PCE to 1.15%.

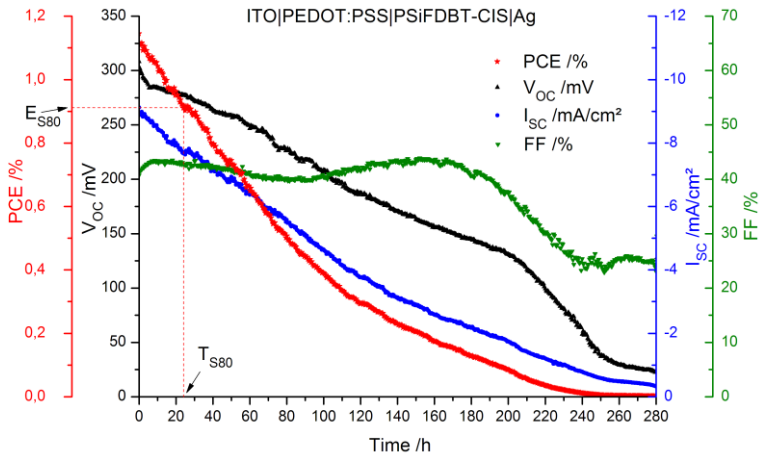

Figure 23: Decay pattern for the PCE, the V_{OC}, the I_{SC} and the FF of a PSiFDBT-CIS nanocomposite solar cell (with silver cathode) over time in air.

After one hour in air the V_{OC} is below 300 mV and reaches values under 250 mV after 58 hours. This voltage drop is assumed to be caused by the oxidation of silver at the absorber layer – electrode interface. Silver forms multivalent forms of oxides (Ag_2O, AgO, Ag_3O_4 and Ag_2O_3) by interacting with oxygen, while it is found that Ag_2O and AgO are the most observable phases.[139] Ag_2O films in general were reported to show a work function ranging from 4.8 to 5.1 eV,[140] thus the internal electric field gets lower due to silver oxidation leading to reduced V_{OC} values. Reese et al. employed TOF-SIMS to detect AgO, Ag_2O, AgS, and Ag_2S fragments in fresh and aged P3HT-PCBM devices with silver electrodes.[141] In fresh devices silver sulphide as well as silver oxide moieties are present. The sulphide compositions at the absorber layer – electrode interface are unchanged upon aging, what indicates that Ag reacts with sulphur sites on P3HT during the deposition process, as suggested earlier by Lachkar et al.[142] Upon air exposure, a pronounced increase of AgO and Ag_2O signals has been observed indicating further oxidation of silver at the absorber layer – electrode interface over time.

The I_{SC} shows a near linear decay over time. Starting from 9.1 mA/cm² the I_{SC} decreases to a value of 6.4 mA/cm² after 60 hours, reaching 3.8 mA/cm² after 120 hours of operation. The FF in contrast shows stable behavior in the first 180 hours of operation. If the initial voltage drop between the measurement inside the glovebox and the first measurement in air gets accounted as burn-in phase, the T_{S80} value is reached after 23 hours. After ~70 hours still 50% of initial PCE is remained and thus devices with silver

electrodes exhibit an at least 20-fold increased stability compared to devices with aluminum electrodes.

From IV-curves of the solar cells during the ageing experiment, it can be seen that R_s and R_{sh} stay relative constant during the first 150 hours of operation. In contrast to the behavior of solar cells with aluminum electrodes (Figure 12), overall resistivity does not increase with the ageing of the cell. At forward bias voltages above V_{OC} (Figure 24, first quadrant) even higher amounts of current are flowing through the degraded device than initially. This indicates rather the formation of additional conductive paths through the cell, which can be caused by migration of silver through the absorber layer,[143] than the formation of insulating layers.

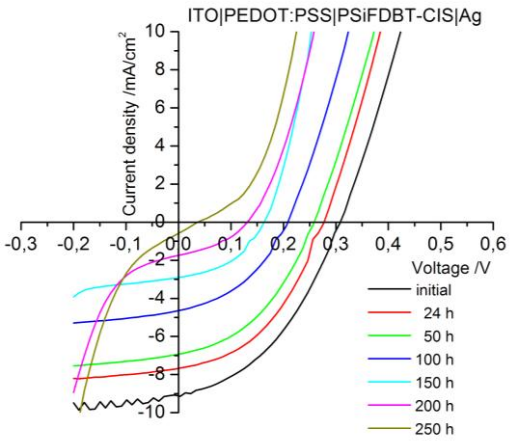

Figure 24: Representative IV-curves during the ageing experiment of a PSiFDBT-CIS hybrid solar cell with a silver cathode.

It can be clearly seen, that the replacement of aluminum with silver leads to a significantly better stability under permanent illumination in air. It can be concluded that the fast degradation of hybrid solar cells with aluminum electrodes does not occur due to oxidation of the organic active layer itself. The predominant mechanism is the corrosion of the aluminum cathode or degradation of the absorber layer - metal electrode interface, what limits charge extraction. For that reason, the next series of experiments concerning the stability of hybrid solar cells have been carried out with silver cathodes.

3.5.2 Replacement of PEDOT:PSS as anode interlayer

To examine the possible instabilities concerning the application of a PEDOT:PSS anode interlayer, solar cells without an anode interlayer and solar cells with an alternative hole transport layer, a sufonated poly(thiophene-3-[2-(2-methoxyethoxy)ethoxy]-2,5-diyl), namely Plexcore® OC 1200, have been fabricated. The chemical structures of PEDOT:PSS and Plexcore® OC are shown in Figure 25 and Figure 26, respectively. According to the supplier, this sulfonated polythiophene ink exhibits a lower acidity compared to PEDOT:PSS and dried films are less hygroscopic.

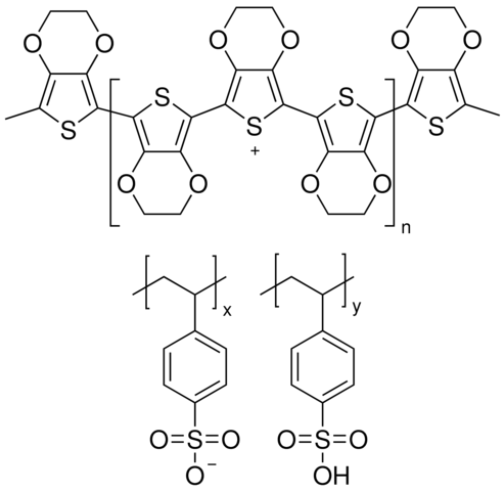

Figure 25: Chemical structure of PEDOT:PSS

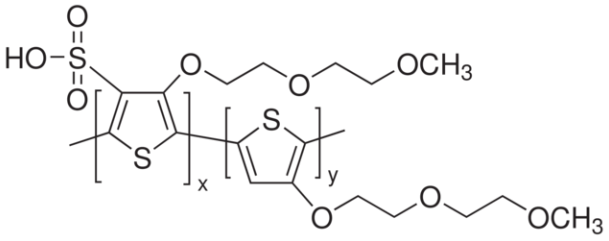

Figure 26: Chemical Structure of Plexcore® OC 1200 Ink

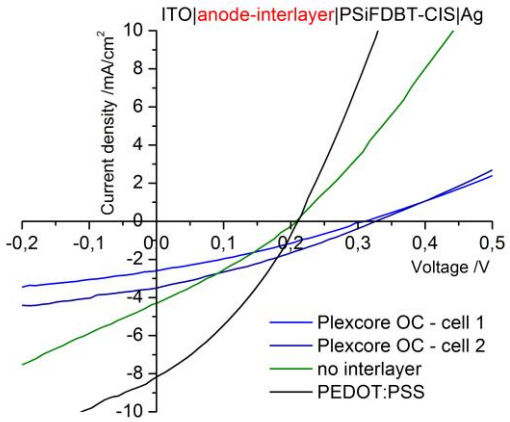

Figure 27: IV-curves from PSiFDBT-CIS solar cells with Plexcore® OC and PEDOT:PSS anode interlayers as well as no anode interlayer in combination with Ag electrodes obtained from measurements in air.

In Figure 27, IV-curves from PSiFDBT-CIS solar cells with Plexcore® OC and PEDOT:PSS anode interlayers as well as a cell without an anode interlayer in combination with Ag electrodes obtained from measurements in air are shown. The corresponding electrical parameters can be found in Table 1. Again, initial PCE values obtained from measurements inside the glovebox have been higher, as V_{OC} values have been higher (not shown).

Table 1: Characteristic parameters of PSiFDBT-CIS solar cells with Plexcore® OC and PEDOT:PSS anode interlayers as well as no anode interlayer in combination with Ag electrodes obtained from measurements in air.

	Anode Interlayer	V_{OC} /mV	I_{SC} /mA/cm²	FF /%	PCE /%
Cell 1	Plexcore® OC	305	2.6	30.2	0.24
Cell 2	Plexcore® OC	327	3.5	29.9	0.34
Cell 3	no interlayer	208	4.3	28.8	0.26
Cell 4	PEDOT:PSS	211	8.2	32.7	0.56

It can be seen that hybrid solar cells with Plexcore® OC interlayers and the solar cell without an anode interlayer exhibit lower performance than devices prepared with a PEDOT:PSS interlayers. In the case of the devices with the alternative interlayer, V_{OC}´s obtained in air are similar to that from the device with PEDOT:PSS in chapter 5.4.1, I_{SC} and FF controversially are significantly lower, leading to PCEs of 0.24% and 0.34%. The reference solar cell with a PEDOT:PSS anode interlayer shows a V_{OC} of 211 mV, an I_{SC} of 8.2 mA/cm² and a FF of 32.7, leading to a PCE of 0.56%. The cell without an anode interlayer exhibits a reduced V_{OC} of 208 mV, however, the I_{SC} of 4.3 mA/cm² is higher than in cells with the alternative interlayers. A poor FF of 28.8% leads to a PCE of 0.26%. It has to be noted that reproducibility for the cells without an anode interlayer is not given in the same extent as for cells with anode interlayers, presumably due to reduced wetting parameters of the precursor solution on bare ITO.

In Figure 28, the efficiencies of these cells over time under continuous illumination are presented. The obtained PCE values from these cells are normalized to the values in Table 1.

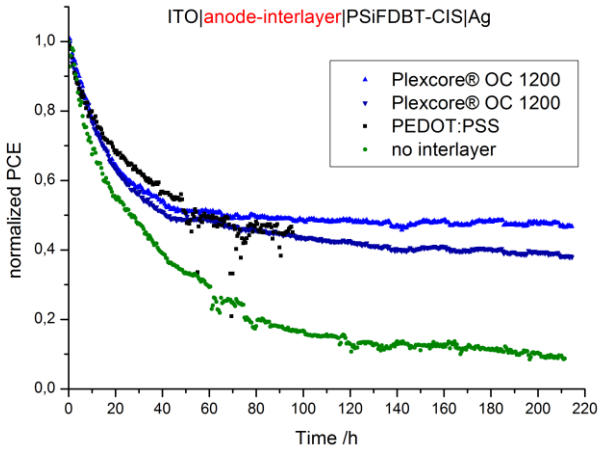

Figure 28: normalized PCE values of hybrid solar cells with different anode interlayers over time under permanent illumination.

In the case of the reference solar cell with PEDOT:PSS as anode interlayer, the external electrical contact was lost after 96 hours. Till this time the cell with the PEDOT:PSS interlayer and the cells with Plexcore® OC Ink as anode interlayer show similar stabilities. However, compared with the results in the previous chapters, the cells with Plexcore® OC interlayers seem to be more stable after ~80 hours of illumination. The

degradation rate decreases significantly after 40-50 hours of testing. Nevertheless, PCE values are below 0.17 % from that time on.

Times to reach 50% of initial PCE in air are between 42 and 60 hours in the case of the cells with Plexcore® OC interlayers, 50 hours in the case of the cell with PEDOT:PSS interlayer and 27 hours in the case of the cell without an anode interlayer.

Plexcore® OC is not an adequate substitute for PEDOT:PSS concerning the PCEs of the cells. Also cells fabricated without an anode interlayer do no show comparable performance to cells with a PEDOT:PSS interlayer. In chapter 3.12, the influence of an inorganic anode interlayer V_2O_5 on the performance and stability of hybrid solar cells will be discussed.

3.5.3 Replacement of PSiFDBT as donor polymer

In the next series of experiments, hybrid solar cells with two alternative low-bandgap donor polymers have been fabricated. For that purpose PSiFDBT has been replaced with poly[[9-(1-octylnonyl)-9H-carbazole-2,7-diyl]-2,5-thiophenediyl-2,1,3-benzothiadiazole-4,7-diyl-2,5-thiophenediyl] (PCDTBT) and poly[(2,3-diphenylthieno[3,4-b]pyrazin-5,7-diyl)-1,2-ethindiyl[2,5-bis(dodecyloxy)-1,4-phenylen]-1,2-ethindiyl] (TPPEPPE). The chemical structures of PCDTBT and TPPEPPE are shown in Figure 29 and Figure 30, respectively.

The backbones of PSiFDBT and PCDTBT are chemically identically except the bridging atom in the fluorene block; i.e. silicon in the case of PSiFDBT and nitrogen in the case of PCDTBT. Due to different valences of the bridging atoms, the aliphatic side groups that are attached directly on the bridging atom, are slightly different too; i.e. dioctyl in the case of PSiFDBT and 1-octylnonyl in the case of PCDTBT.

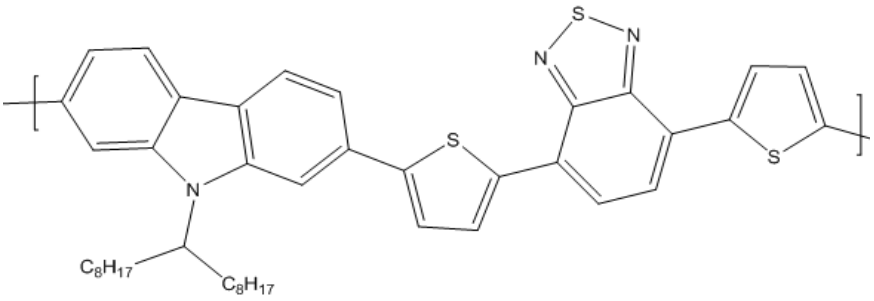

Figure 29: Chemical structure of PCDTBT

Both polymers have been studied as donor materials of choice in combination with CIS in our group. They exhibit similar optical properties and the HOMO and LUMO level are nearly identical.[144]

Best hybrid solar cells fabricated in combination with these two polymers also showed similar efficiencies (see chapters 3.10 and 3.16). Different suppliers and even different chemical batches from the same manufacturer have shown have a higher impact on polymer quality concerning the obtained cell efficiencies.[144]

TPPEPPE constits of diphenylthienopyrazin, ethinyl and benzene repeating units with two dodecyloxy side chains at the benzene ring. According to Manceau et al.[122] show dialkoxybenzene units a similar photochemical stability as carbazole units that are present in PCDTBT. The introduction of thienopyrazin units leads to an increase in the polymer HOMO energy level[145] and thus a lower oxidative stability would be expected.[146] Interestingly thienopyrazin units show experimentally in contrast superior photochemical stabilities.[122]

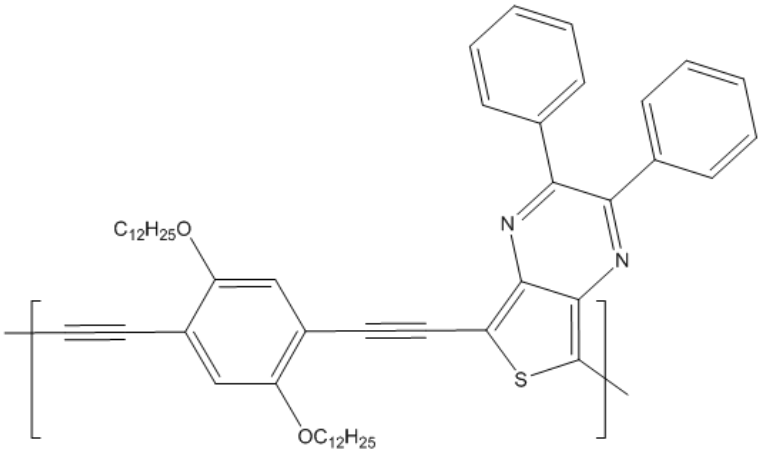

Figure 30: Chemical structure of TPPEPPE

IV-curves from the first measurement of two hybrid solar cells with PCDTBT and TPPEPPE, respectively, in ambient atmosphere are shown in Figure 31. The corresponding characteristic electric parameters are listened in Table 2.

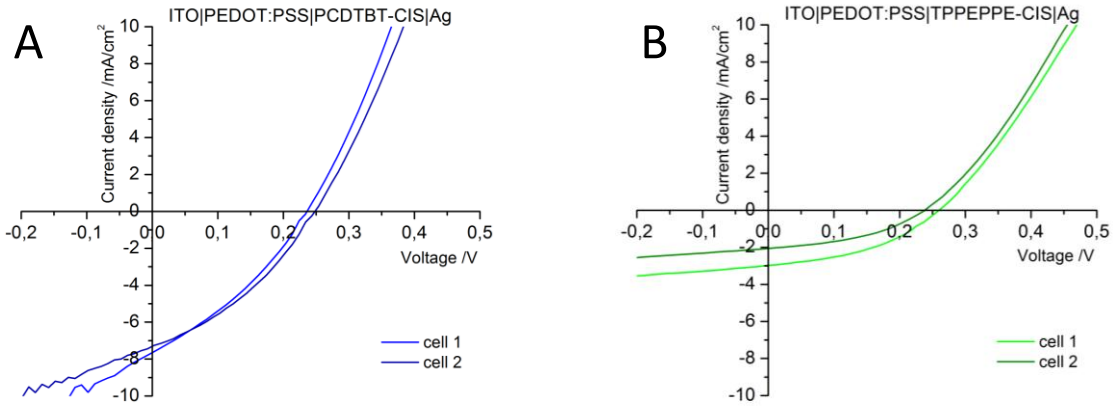

Figure 31: IV curves of (A) PCDTBT-CIS hybrid solar cells and (B) TPPEPPE-CIS hybrid solar cells obtained from measurements in ambient atmosphere.

Table 2: Characteristic solar cell parameters of PCDTBT-CIS hybrid solar cells and TPPEPPE-CIS hybrid solar cells obtained from IV-curves in ambient atmosphere.

	Donor-polymer	V_{OC} /mV	I_{SC} /mA/cm²	FF /%	PCE /%
Cell 1	PCDTBT	231	7.7	32.6	0.58
Cell 1	PCDTBT	248	7.3	35.1	0.64
Cell 2	TPPEPPE	246	2.0	41.1	0.20
Cell 2	TPPEPPE	236	3.0	41.1	0.32

In this series, hybrid solar cells with PCDTBT as electron donor showed slightly reduced V_{OC} and I_{SC} values compared to solar cells with PSiFDBT as electron donor. The FF shows distinct lower values leading to PCE values around 0.6% obtained from measurements in air. Hybrid solar cells with TPPEPPE as electron donor show comparable V_{OC} and FF values; I_{SC} values in contrast are significant lower and thus PCE values too. Nevertheless as characteristic electric parameters are in the same order, the influence on device stability was examined.

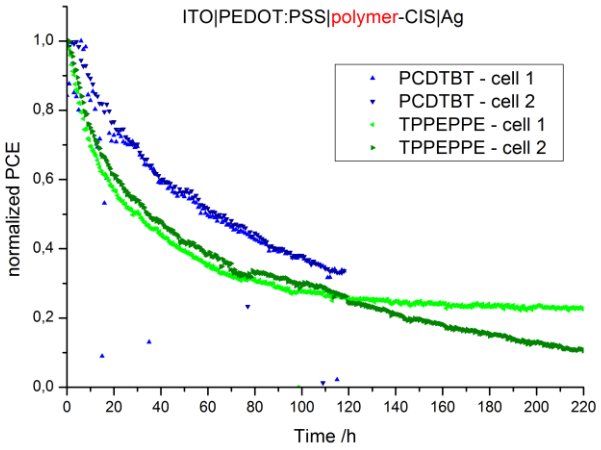

Figure 32: Decay pattern of normalized PCE values from two PCDTBT-CIS and two TPPEPPE-CIS hybrid solar cells.

For better comparison of stability data, the initial efficiencies have been normalized to the values in Table 2. Figure 32 shows the decrease in PCE of these hybrid solar cells over time under permanent illumination. It can be seen that solar cells with PCDTBT as electron donor show similar stabilities as cells with PSiFDBT (Figure 21 and Figure 28). The external electrical contact at the ITO electrode was lost after 118 hours of operation; due to the fact that both single cells are attached to the same anode, could both cells not be monitored any longer. However time to reach 50% of initial PCE is in both cells in the range of 60 hours, compared to 70 and 50 hours obtained from the first stability measurements with PSiFDBT (Figure 21 and Figure 28). Solar cells with TPPEPPE as electron donor degraded faster. The time to reach 50% of initial PCE is in the range between 30 hours and 40 hours. It can be concluded that TPPEPPE is no adequate substitute for PSiFDBT, neither in terms of the obtained efficiencies nor in terms of stability.

3.6 Encapsulation

From the obtained results of the stability measurements of hybrid solar cells performed under permanent illumination it can be seen that the devices are not stable under atmospheric conditions due to chemical and photochemical reactions mainly with oxygen and water. Thus they have to be protected from oxygen and humidity. Proper encapsulation is seen as one of the crucial points in any future commercialization of organic as well as hybrid photovoltaic devices.[147] The ability of oxygen and moisture to cross an encapsulation material can be expressed by the oxygen transmission rate (OTR) and the water vapor transmission rate (WVTR), respectively. The demand on OTR and WVTR for OLED devices achieving lifetimes above 10000 hours requires values below 10^{-3} $cm^3/m^2/day^1/atm^1$ and 10^{-6} $g/m^2/day^1$, respectively[148] and these values have been seen as the upper limit of organic solar cell requirements as well,[149] while recent studies indicate that the demand for the WVTR can be lowered with the introduction of new device architectures.[150] Additionally, encapsulation materials should offer sufficient UV light resistance.

As glass offers excellent barrier properties against water and oxygen and hybrid solar cells in this work have been fabricated on glass substrates, glass has also be chosen as encapsulation material. For this purpose, an additional backsheet glass slide has been glued onto the device stack glass|ITO|PEDOT:PSS|PSiFDBT-CIS|cathode (Figure 33).

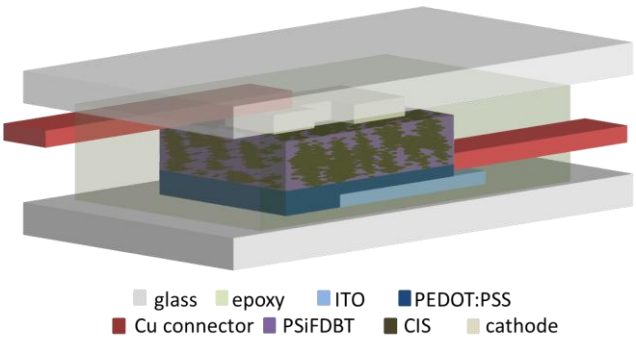

Figure 33: Schematic device architecture of an glass-glass encapsulated PSiFDBT-CIS hybrid solar cell.

Due to the rapid degradation of hybrid solar cells with aluminum electrodes, ultrafast curing epoxy glue was introduced. Nevertheless, hybrid solar cells with aluminum electrodes could not be stabilized through encapsulation; similar results as obtained during lifetime tests performed in an inert gas measuring chamber (chapter 3.4) have

been obtained (not shown). In chapter 3.10, the result of a stability measurement of a glass-glass encapsulated solar cell with aluminum electrodes will be demonstrated. Encapsulated hybrid solar cells with silver electrodes in contrast show eminently stable behavior over the first few thousand hours of operation.

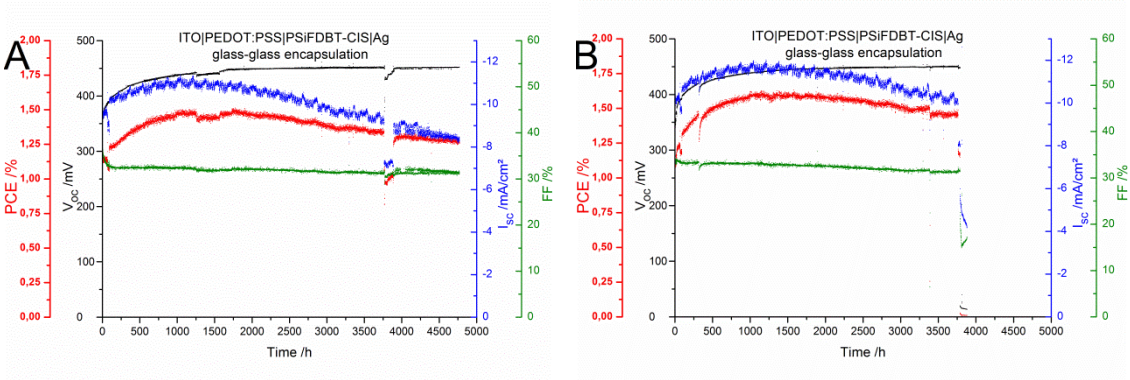

Figure 34: Lifetime tests of glass-glass encapsulated PSiFDBT-CIS hybrid solar cells with silver electrodes performed under continuous illumination using a sulphur plasma lamp.

Figure 34A and B show the result of a long term measurement of encapsulated hybrid solar cells with Ag electrodes. Both cells show an increase in efficiency in the first 1500 hours of operation, mostly stemming from an increase in I_{SC} as well as V_{OC}, followed by a moderate decrease in efficiency after that period, mostly due to a decrease in I_{SC}. The measurement of cell A has been stopped after 4700 hours due to a breakdown of the sulphur plasma lamp. Cell B showed a sudden drastic failure after 3700 hours of operation. The solar cell lost its open circuit voltage, indicating a shunting of the cell, presumably stemming from the formation of a conductive path between the two electrodes due to silver migration and dendrite formation leading to a partial electrical short circuit.[143]

Interestingly no voltage drop to values around 300 mV occurs during the measurement, as seen in cells aged without encapsulation. This leads to the assumption, that the glass-glass encapsulation with epoxy glue offers an appropriate protection for oxygen or water ingress and device failure can be related to rather intrinsic instabilities than to oxidation processes.

3.7 Accelerated ageing

As lifetimes of organic and hybrid solar cells of a few years are required for commercialization, long lasting stability determinations may slow down progress in market launch. Accelerated ageing test, as a common approach in inorganic solar cell technology, offers an appropriate method to circumvent this issue.[151]

Some workgroups published the use of elevated temperatures[64,152,153] or elevated irradiance intensities[154] for accelerated ageing of organic solar cells. Under the assumption, that degradation follows an Arrhenius model, a recalculation of the degradation rate under real environmental conditions should be possible. This technique however is not generally addressable, because degradation mechanisms may be different for various material combinations and various device architectures and thus do not follow a simple Arrhenius model. Furthermore, the ageing at elevated temperatures may accelerate oxygen induced chemical degradation but conversely reduces water from the device and thus real life conditions may be falsified.[151]

3.7.1 Damp-heat Tests

A PSiFDBT-CIS hybrid solar cell that has been glass-glass encapsulated with a dedicated encapsulation epoxy for organic electronic devices (Epotek 302-3M) and showed stable behaviour over a testing period of 1330 hours has been subjected to a damp-heat test for duration of seven days. Afterwards the solar cell has been again connected to the automated measuring system and further characterized to determine the influence of these harsh conditions on device performance. Damp-heat tests have been carried out in weathering chambers at the facilities of Isovoltaic AG. The samples have been exposed to ambient conditions of 85°C in combination with 85% relative humidity (RH). These testing conditions are part of the norms IEC 61215 and IEC 61646 for inorganic solar cells.

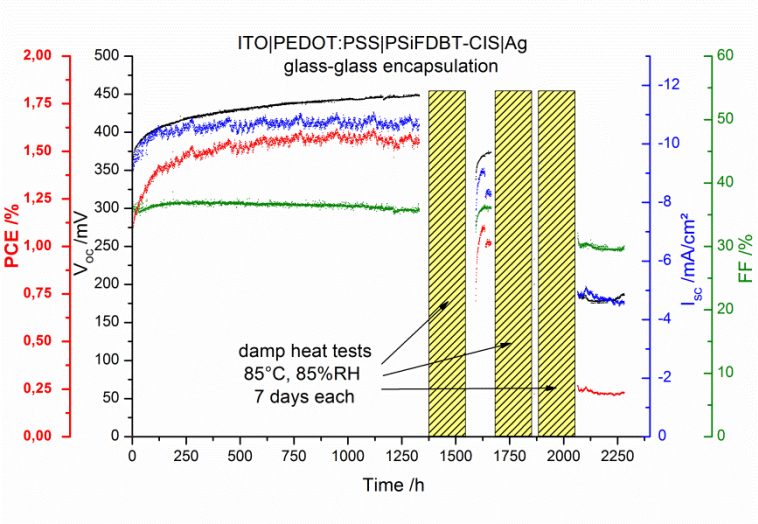

Figure 35: Lifetime tests of a glass-glass encapsulated PSiFDBT-CIS hybrid solar cells with silver electrodes performed under continuous illumination using a sulphur plasma lamp including three damp-heat tests over seven days each.

As seen in Figure 35, the initial PCE of about 1.5% has dropped significantly to a value of 0.7% after the first damp heat test, followed by steadily regeneration under operation during permanent illumination to values between 1.1% and 1% during the next 24 hours. In addition, two further damp heat tests over a testing period of one week each have been conducted. Between these two exposures only one IV-curve of the solar cell has been collected, thus a possible regeneration phase under illumination could not be observed. The obtained PCE value has been 0.22%, the solar cell showed an I_{SC} of 4.4 mA/cm^2, a V_{OC} of 200 mV and a FF of 28%. After overall three damp heat tests, the solar cells has degraded significantly, showing a PCE of 0.25%, a V_{OC} of 183 mV, an I_{SC} of 4.5 mA/cm² and a FF of 32%. In the subsequent monitoring of the cell, the solar cell further shows a slight degradation over additional 200 hours. The obtained results suggest that the glass-glass encapsulation with this epoxy glue does not withstand the damp-heat test as additionally a yellowing of the epoxy glue has been observed.

Similar results have been published for P3HT:PCBM devices. Established lifetimes in their work under moderate testing conditions lie in the range of several years, while under harsh testing conditions lifetimes of only weeks have been obtained.[151]

In the course the ISOS initiative, a temperature reduction from 85°C to 65°C during damp-heat tests, while maintaining 85% relative humidity is in discussion. Bardizza et al. already published accelerated ageing studies at these conditions.[155]

3.7.2 Thermal stress

To evaluate the influence of thermal stress without raised humidity on the stability of hybrid solar cells, glass-glass encapsulated devices were exposed to temperatures of 75°C and 85°C respectively using heating plates and exposed to permanent lighting. For this purpose, temperature sensors (resistance temperature detectors - PT100) were directly attached to the absorber layer and co-encapsulated. This allowed adjustment of prerequisite heating temperature and a monitoring of the actual cell temperature over time. As heating plates could not be positioned in the focus of the plasma lamp, light intensity has been lower (~35 mW/m²) in this experiment.

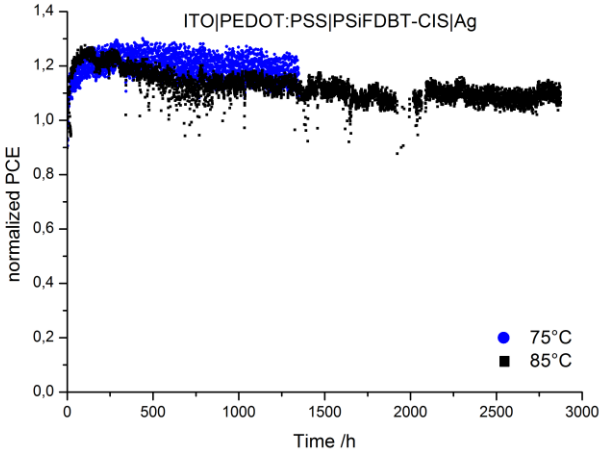

Figure 36: Lifetime tests of glass-glass encapsulated PSiFDBT-CIS hybrid solar cells with silver electrodes at elevated temperatures of 75°C and 85°C, respectively, performed under continuous illumination (~35 mW/cm²) using a sulphur plasma lamp.

Figure 36 shows the result of a lifetime test of glass-glass encapsulated PSiFDBT-CIS hybrid solar cells kept at 75°C and 85°C. Under these conditions, solar cells do not show accelerated degradation. The initial increase in PCE, as observed in the previous chapters is present again, but PCE seems to reach its maximum earlier; i.e. after about 100 hours at 85°C and after 280-300 hours at 75°C. The monitoring of the cell kept at 75°C has been stopped after 1300 hours due to limited availability of channels at the automated measuring system. It can be concluded, that a constantly elevated cell temperature in combination with ambient humidity does not cause perceptible device failure as observed at devices that were exposed to a damp-heat test (see Figure 35).

3.8 Introduction of cathode interlayers

By comparing the record cells in terms of efficiency with aluminum and silver electrodes prepared during the CDL, respectively (Figure 37 and Table 3), it can be seen, that both cells exhibit an I_{SC} about 11.3 mA/cm² and a FF about 45.5%. The significant difference of the two cells is the reduced V_{OC} of cells with silver electrodes; i.e. 450 mV, compared to 550 mV in the case of aluminum electrodes, leading to a PCE of 2.4% compared to 3.0%. The device with the aluminum electrode has been prepared by Stefan Moscher and the device with the silver electrode has been prepared by Verena Kaltenhauser.

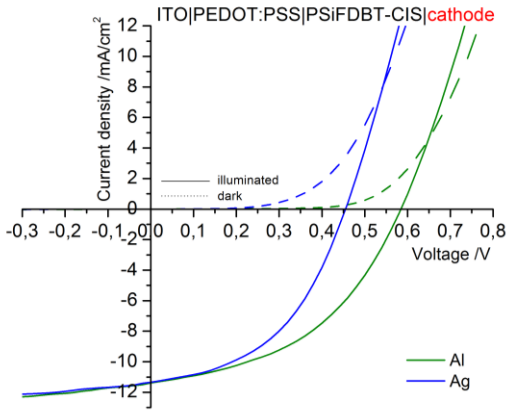

Figure 37: IV-curves of benchmark hybrid solar cells with aluminum and silver cathodes, respectively. (Data taken from Stefan Moscher and Verena Kaltenhauser.)

Table 3: Electrical parameters of best hybrid solar cells with different cathode materials including work functions of cathode materials.[133] (Data taken from Stefan Moscher and Verena Kaltenhauser.)

Cathode Material	Work function / eV	V_{OC} / mV	I_{SC} / mA/cm²	FF / %	PCE / %
Al	4.06 - 4.26	580	11.4	45.5	3.01
Ag	4.52 - 4.74	460	11.3	46.0	2.40

As already mentioned, the lower V_{OC} of cells with silver cathodes can be explained with the less favored work function of silver in respect with PEDOT:PSS compared to aluminum, resulting in a lowered internal electric field.

An opportunity to circumvent this issue is the introduction of cathode interlayers. Interface layers can be conducting, semiconducting or non-conducting materials in ultra-thin application.[156] The main functions of interface materials are the adjustment the energetic barrier height between the active layer and the electrodes, minimizing injection losses at interfaces, the formation of selective contacts for carriers of one kind (it is even possible to determine the polarity of the device, see chapter 3.16), the reduction of recombination processes at the interface and the suppression of chemical or physical reaction between the polymer and the electrode as well as the suppression of oxygen and water intake through the metal electrode.[156, 157]

Several, metal oxides like TiO_x,[158] ZnO,[159] CuO_x,[160] CrO_x,[161,162] MnO,[163] thin metal layers like Ti[164] and Cr[165] as well as organic materials like bathocuproine (BCP),[166] bathophenanthroline (Bphen)[167] and metal-organic compounds like tris(8-hydroxyquinolinato)aluminum (Alq_3)[168] have been already introduced as cathode interlayer in organic solar cells, leading to better photovoltaic performance and ambient stability. In this chapter the influence of cathode-interlayers on the efficiency and stability of polymer-$CuInS_2$ nanocomposite solar cells was investigated. In order to improve the V_{OC} of hybrid solar cells with Ag electrodes the cathode-interlayers Cs_2CO_3, Mg and Ti have been introduced. Cs_2CO_3 (1 nm), Mg (20 nm) and Ti (5 nm) interlayers have been thermally evaporated.

3.8.1 Introduction of caesium carbonate cathode interlayers

Cs_2CO_3 interlayers have been already sucessfully used in regular,[169] inverted[170] and semi-transparent[171] P3HT-PCBM solar cells. Yang et al. demonstrated that P3HT-PCBM solar cells with a thin (1 nm) Cs_2CO_3 cathode interlayer between the alumnium electrode and the absorber layer exhibited enhanced performance and improved air stability.[172]

Cs_2CO_3 interlayers have been introduced to enhance electron injection in OLEDs.[173] In addition, Cs_2CO_3 has been used as a n-type dopand for organic electron transport layers.[174] Cs_2CO_3 exhibits a work function of 2.2 eV,[170] however, during thermal

evaporation, a partially decomposition of Cs_2CO_3 into CsO_2 and caesium sub oxides (CsO),[175] yielding a heavily doped n-type semiconductor with low work function and even reduction into metallic Cs[176] has been proven.

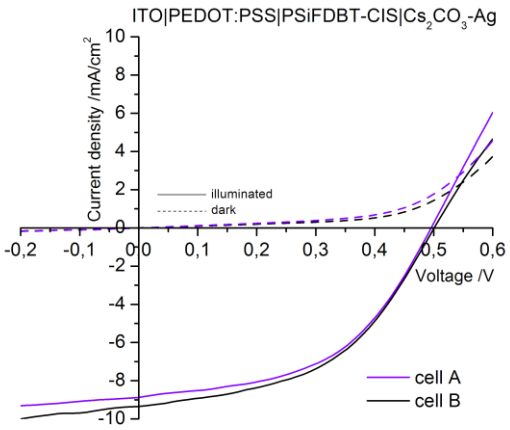

Figure 38: IV-curves of PSiFDBT-CIS hybrid solar cells with Cs_2CO_3 cathode interlayers in combination with silver electrodes under illumination and in the dark.

Figure 38 shows IV-curves of hybrid solar cells in the architecture ITO|PEDOT:PSS|PSiFDBT-CIS|Cs_2CO_3-Ag. The Cs_2CO_3 interlayer has a thickness of 1 nm and has been thermally evaporated. The characteristic electric parameters are summarized in Table 4.

Table 4: Electrical parameters of PSiFDBT-CIS hybrid solar cells with Cs_2CO_3 cathode interlayers in combination with silver electrodes including work function of Cs_2CO_3.[162]

Solar cell	Cathode Material	Work function / eV	V_{OC} / mV	I_{SC} / mA/cm²	FF / %	PCE / %
Cell A	Cs_2CO_3-Ag	2.2	502	8.88	49.2	2.19
Cell B	Cs_2CO_3-Ag	2.2	502	9.35	48.1	2.26

The devices exhibit V_{OC}-values of 502 mV, thus a distinct improvement compared to devices with bare Ag electrodes. FF-values higher than 48% in combination with I_{SC}-values above 8.8 mA/cm² lead to PCE-values around 2.2%.

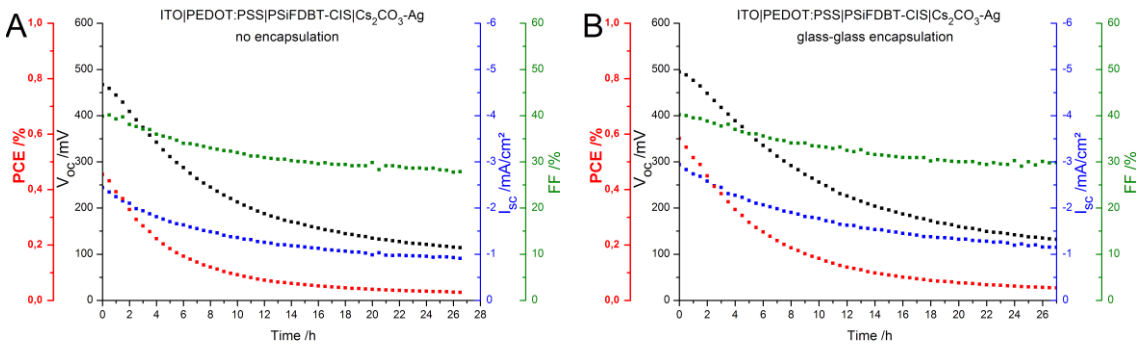

Figure 39: Lifetime tests of non-encapsulated (A) and glass-glass encapsulated (B) PSiFDBT-CIS hybrid solar cells with Cs_2CO_3 cathode interlayers and Ag electrodes performed under continuous illumination using a sulphur plasma lamp.

Hybrid solar cells with Cs_2CO_3-Ag cathodes do not show stable behaviour. The cell without encapsulation shows a significant reduction of Isc between the first measurement inside the glovebox (Table 4) and the first measurements in air (Figure 39A). Interestingly, an evident V_{OC} drop to values around 300 mV, as observed at non-encapsulated devices with bare silver electrodes in ambient atmosphere, does not occur. In the case of the encapsulated cell, a degradation during curing of the epoxy glue could be observed, leading to a reduced I_{SC} of 2.45 mA/cm² after encapsulation (Figure 39B) and thus the cell could not be stabilized by encapsulation. Encapsulated or not, both cells show similar performance losses over time in the first 24 hours. After 6 hours PCE values are below 0.2%.

3.8.2 Introduction of magnesium cathode interlayers

Mg interlayer has been introduced to even achieve higher voltages than cells with Al electrodes as work function of Mg lies around 3.66 eV.[133] Additionally the Mg interlayer acts as proof of principle, that the Voc is determined by the interlayer (if present) and not the electrode itself. A 30 nm Mg cathode interlayer has already been successfully introduced in CuPc:C60 solar cells with Ag electrodes and a V_{OC} increase from ~300 mV to ~450 mV was observed.[177] Furthermore, a protection of the thin Mg layer through the Ag coverage against water and oxygen ingress seems likely. Controversially Mg in direct contact with the noble silver may act as sacrificial anode.

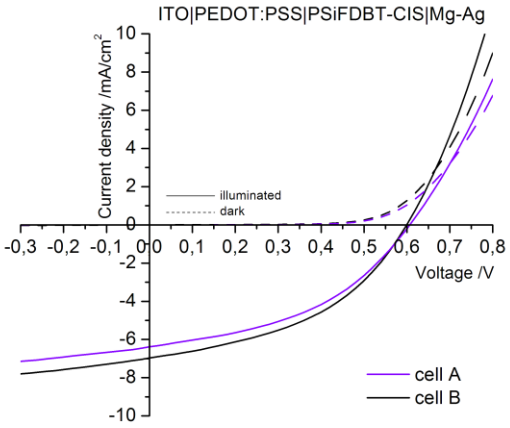

Figure 40: IV-curves of PSiFDBT-CIS hybrid solar cells with Mg cathode interlayers in combination with silver electrodes under illumination and in the dark.

Hybrid solar cells with Mg-Ag cathodes show V_{OC}-values between 600 and 605 mV and thus the highest voltages among all tested cathode configurations. FF-values between 43.5% and 43.7% and lowered I_{SC} values of 6.39-6.97 mA/cm² lead to efficiencies between 1.67% and 1.83% (see Figure 40 and Table 5).

Table 5: Electrical parameters of PSiFDBT-CIS hybrid solar cells with Mg cathode interlayers in combination with silver electrodes including the work function of Mg.[133]

Solar cell	Cathode Material	Work function / eV	V_{OC} / mV	I_{SC} / mA/cm²	FF / %	PCE / %
Cell A	Mg-Ag	3.66	603	6.39	43.5	1.67
Cell B	Mg-Ag	3.66	600	6.97	43.7	1.83

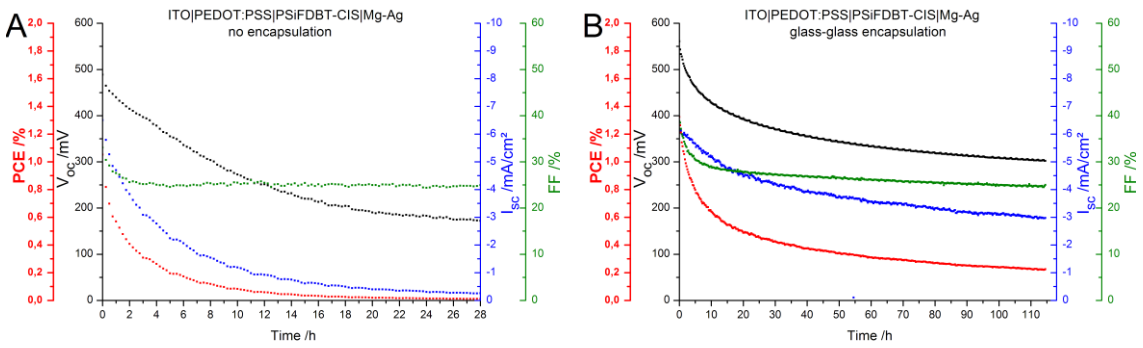

Figure 41: Lifetime tests of non-encapsulated (A) and glass-glass encapsulated (B) PSiFDBT-CIS hybrid solar cells with Mg-Ag electrodes performed under continuous illumination using a sulphur plasma lamp.

From stability measurements in air (Figure 41A), it can be seen, that the initial high V_{OC}, obtained from measurements inside the glovebox, was lost immediately; during the first IV-curve in air only 470 mV has been obtained, followed by a further decrease, leading to V_{OC}-values lower than 250 mV after 12 hours of operation.

The encapsulated hybrid solar cell with Mg-Ag cathodes (Figure 41B) still shows 540 mV after encapsulation, however after 24 hours of operation, V_{OC} is below 400 mV. Also I_{SC} and FF show reduced values of 4.4 mA/cm^2 and 27.5%, respectively, leading to a PCE of 0.46% after 24 hours under permanent illumination. Encapsulation has slowed down the degradation of hybrid solar cells with Mg-Ag electrodes; nevertheless, compared to devices with Ag electrodes, solar cells with Mg-Ag electrodes do not show stable behavior.

3.8.3 Introduction of titanium cathode interlayers

In this series of experiments a Ti interlayer has been introduced between the absorber layer and the silver cathode. The Ti interlayer thickness of 5 nm was adopted from Zimmermann et al.[165] Ti exhibits a work function of 4.33 eV[133] and thus higher V_{OC}-values than in devices with silver electrodes are expected. Ti as non-noble metal tends to form a passivation layer when exposed to humidity or oxygen. Passeggi Jr. et al.[178] studied the oxidation processes of Ti thin films and found that Ti reacts almost completely to form TiO previous to the appearance of TiO_2 and the saturation state consists of a mixture of TiO and TiO_2. Thus the Ti-interlayer may act as oxygen scavenging species to a certain degree preventing oxidation of the absorber layer.

Additionally the formed titanium suboxide shows semiconducting properties[179] and may act as cathode interlayer as well.

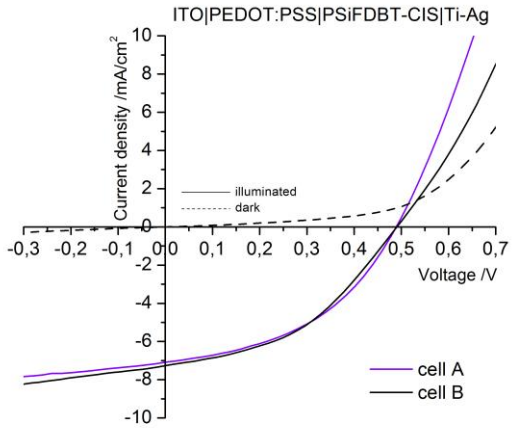

Figure 42: IV-curves of PSiFDBT-CIS hybrid solar cells with Ti-cathode interlayers in combination with silver electrodes under illumination and in the dark.

Figure 42 shows IV-curves of hybrid solar cells in the architecture ITO|PEDOT:PSS|PSiFDBT-CIS|Ti-Ag. The characteristic electric parameters are summarized in Table 6. The devices exhibit V_{OC}-values of 489 mV and FF-values between 43.4 and 45.1%. Reduced I_{SC}-values compared to solar cells without cathode interlayer in the range of 7.1-7.3 mA/cm² limit their PCE to ~1.55%.

Table 6: Electrical parameters of PSiFDBT-CIS hybrid solar cells with Ti cathode interlayers in combination with silver electrodes including the work function of Ti.[133]

Solar cell	Work function / eV	V_{OC} / mV	I_{SC} / mA/cm²	FF / %	PCE / %
Cell A	4.33	489	7.09	45.1	1.56
Cell B	4.33	489	7.29	43.4	1.53

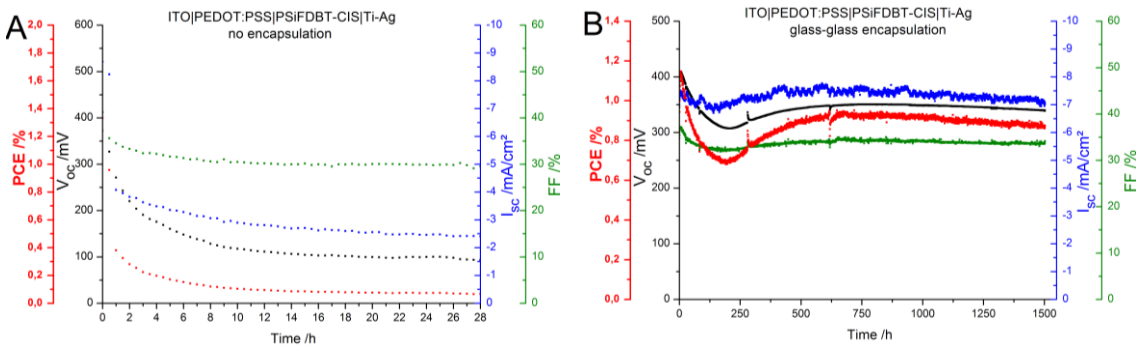

Figure 43: Lifetime tests of non-encapsulated (A) and glass-glass encapsulated (B) PSiFDBT-CIS hybrid solar cells with Ti-Ag electrodes performed under continuous illumination using a sulphur plasma lamp.

In Figure 43A it can be seen that the device that has not been encapsulated degraded within the first hours. During the first measurement in air, a PCE of 1.33% was obtained, after 30 minutes the device had a PCE of 0.95% and after 1 hour only 0.38% could be obtained. The encapsulated device in contrast showed relative stable behaviour (Figure 43B). After encapsulation, the solar cell had a V_{OC} of 408 mV, an I_{SC} of 7.48 mA/cm² and a FF of 37.1%, leading to a PCE of 1.15%. The device showed a heavy burn-in phase during the first 180 hours, mainly due to a distinct reduction of the V_{OC}, lowering the PCE to 0.68%. From that time on, the values recovered partly during the next 500 hours, leading to a V_{OC} of 349 mV, an I_{SC} of 7.51 mA/cm², a FF of 34.6% and a PCE of 0.94% after 680 hours of testing. After 1500 hours under permanent illumination, the device still showed a PCE of 0.87%. The measurement was stopped after 1500 hours due to a breakdown of the sulphur plasma lamp.

Summing up, the obtained V_{OC}´s of PSiFDBT-CIS hybrid solar cells strongly depend on the work function of the cathode material. The V_{OC} is improved from 460 mV for a solar cell with a bare Ag electrode to 502 mV for devices with a Cs_2CO_3 interlayer, up to 527 mV with a Ti interlayer and to 600 mV with a Mg interlayer. Due to a reduced I_{SC} in devices with cathode interlayer, the obtained PCE values of devices with cathode interlayer are lower compared to the record device with bare Ag electrodes. It has to be noticed, that much more solar cells without cathode interlayer have been fabricated and only few experiments of optimization on interlayer thicknesses or processing steps have been carried out. In respect of operating stability, solar cells with Ti interlayers showed the most promising results and thus the Ti interlayer has been investigated in detail in the following experiments; furthermore a TiO_x interlayer will be introduced.

3.9 Shelf life test of hybrid solar cells with different cathodes

In this experiment, the shelf life under inert gas of PSiFDBT-CIS hybrid solar cells with Al and Ag electrodes with and without an additional Ti cathode interlayer (5 nm) has been examined. During a shelf life test, the solar cells are kept in the dark between the electrical characterizations.[72] For that purpose, the devices have been stored inside a nitrogen filled glovebox and IV-curves have been repeatedly collected over a timeframe of 155 days (Figure 44).

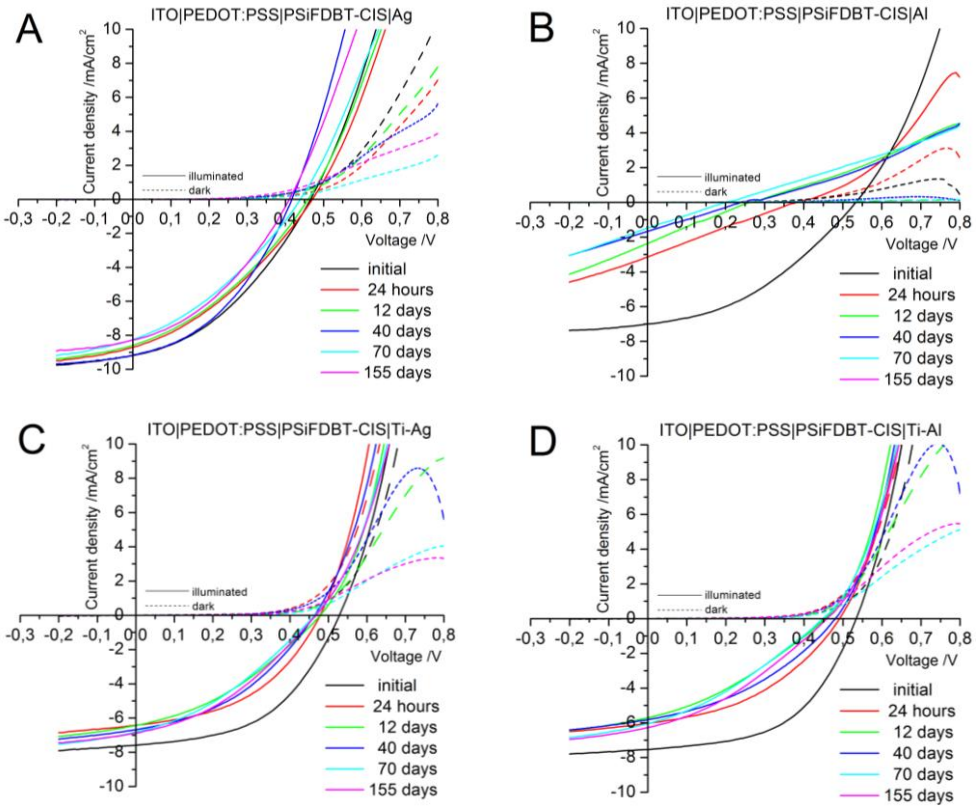

Figure 44: Repeatedly collected IV-curves PSiFDBT-CIS hybrid solar cells with (A) Ag, (B) Al, (C) Ti-Ag and (D) Ti-Al electrodes over a timeframe of 155 days. The devices have been kept in nitrogen atmosphere and in the dark between the measurements.

Table 7 summarizes the electrical parameters of the solar cells with different cathode materials obtained from IV-curves direct after fabrication, after 24 hours of dark storage and after 155 days of dark storage.

Table 7: Electrical parameters of PSiFDBT-CIS hybrid solar cells with different cathode materials obtained from IV-curves direct after fabrication, after 24 hours and after 155 days of dark storage in nitrogen atmosphere.

Cathode Material	Duration of ageing	V_{OC} / mV	I_{SC} / mA/cm²	FF / %	PCE / %
Ag	initial	467	9.18	37.7	1.61
	24 hours	467	8.69	34.5	1.40
	155 days	406	8.27	37.3	1.24
Al	initial	537	6.99	38.5	1.45
	24 hours	386	3.13	23.9	0.29
	155 days	n.a.	n.a.	n.a.	n.a.
Ti-Ag	initial	527	7.58	49.5	2.02
	24 hours	477	6.41	45.3	1.37
	155 days	467	6.87	36.6	1.17
Ti-Al	initial	537	7.54	51.8	2.10
	24 hours	487	6.01	42.0	1.23
	155 days	457	6.27	33.8	0.96

All devices show a distinct initial degradation within the first 24 hours of dark storage; however the solar cell with Ag electrodes without a Ti interlayer behaves as most stable, leading to the highest PCE-value of 1.40% after 24 hours of storage. Main loss parameters are I_{SC} and the FF although the initial FF-value is almost recovered after 155 days. The initial PCE of this device was 1.61% and after 155 days still a PCE of 1.24% was obtained. The solar cell with bare Al electrodes does not show stable behavior even when kept under inert gas and in the dark. After 24 hours of operation, the PCE dropped from initial 1.45% to 0.29%; after 155 days the device does not exhibit a photovoltage and a photocurrent and thus FF and PCE calculation was not possible after this time. The introduction of Ti interlayer clearly stabilizes the solar cell with Al electrodes. While showing a distinct degradation during the first 24 hours, lowering the PCE from 2.10% to 1.23% is still a PCE of 0.96% remained after 155 days of storage. The solar cell with the Ti-Ag cathode shows similar behavior over time. The initial PCE of 2.02% drops to 1.37% after 24 hours but a value of 1.17% is remained after 155 days.

3.10 Influence of TiO_x and Ti cathode interlayers on the performance and stability of hybrid solar cells

Sebastian Dunst, Thomas Rath, Stefan Moscher, Lukas Troi, Matthias Edler, Thomas Griesser, Gregor Trimmel

This chapter was first published in Solar Energy Materials & Solar Cells 130 (2014) 217-224.

3.10.1 Introduction

The field of organic photovoltaics has experienced a high level of attention during the last two decades due to advantages like low consumption of materials, low cost (roll to roll) production as well as fabrication of flexible or semitransparent devices. Inorganic-organic hybrid solar cells, in which a conjugated polymer and an inorganic semiconductor form the absorber layer, could be a promising alternative approach to the already well-established organic polymer/PCBM ([6,6]-Phenyl C_{61} or C_{71} butyric acid methyl ester) solar cells. However, while polymer-PCBM solar cells already reach power conversion efficiencies (PCEs) around and even above 10%,[180,181] efficiencies of polymer/nanoparticle hybrid solar cells are still lower. Currently, the best PCEs reached by polymer/nanoparticle hybrid solar cells are around 5.5%.[40] For recent reviews on organic-inorganic hybrid solar cells see Ref. 53, 182, 183, 184, 185, 186, 187. For commercialization not only high PCE, but also sufficient long term stability has to be ensured. While tremendous work has been done to increase the stability and lifetime of organic solar cells,[66,131,188] only few publications dealing with stability issues of organic-inorganic hybrid solar cells can be found.[77-83] Except the acceptor material, the device architecture and working principle of this type of solar cells is quite similar to the widely investigated polymer/PCBM devices, and therefore, concepts and scientific achievements, which positively influence device performance and stability, can be, to some extent, adapted for the fabrication of stable hybrid solar cells.

In non-inverted bulk heterojunction architecture (for polymer/PCBM as well as polymer/nanoparticle solar cells) typically “low” work function metals are used for

electron extraction to obtain a high internal electric field with respect to the transparent "high" work function ITO-counter electrode. These metals are, however, easily oxidized resulting in electrically insulating interfaces and therefore lead to limited lifetimes of the devices. Using silver instead of aluminum electrodes, the problem of oxidation can be reduced, however, a new challenge, the easy diffusion of this metal into the active layer, which can cause device shunting by diffusion of Ag through the absorber layer, is introduced.[143]

In this context, TiO_x cathode interlayers can lead to enhanced efficiency and stability of polymer/PCBM devices in non-inverted (regular) geometry.[66,158,189,190,191] TiO_x interlayers stabilize the interface between the organic(-inorganic) material and the metal electrode by oxygen scavenging, blocking the passage of oxygen or humidity into the absorber layer and preventing diffusion of cathode material (e.g. Ag) into, or reaction with the absorber layer. Furthermore, TiO_x can act as an optical spacer between the active layer and the metal electrode.[158,192]

There are several methods for the preparation of TiO_x interlayers already established in organic and hybrid photovoltaics, including hydrolysis of titanium alkoxide precursors,[158,190,193] coating of TiO_x nanoparticle solutions,[194,195] atomic layer deposition,[196] chemical vapor deposition[197] or sputtering.[198] In particular, the wide spread method for the preparation of TiO_x cathode interlayers via hydrolysis of organic TiO_x-precursors could be problematic for application in non-inverted solar cells. In this approach, the conversion to TiO_x usually requires elevated temperatures at atmospheric conditions that might harm the active layer. In this context, the Heeger group introduced an "activated" Ti-isopropoxide precursor allowing conversion temperatures around 80°C.[158,189] Furthermore, the preparation of TiO_x layers via sputtering of Ti under controlled oxygen atmosphere could be also problematic for non-inverted solar cells, because the highly energetic particles impacting the absorber layer during the sputtering process can lead to negative alterations in the absorber layer, hampering device performance.[55,198]

In this contribution, we discuss the preparation of thin TiO_x interlayers via oxidative evaporation of Ti under medium vacuum conditions (residual gas air) similar to a previously reported route for the formation of CuO_x[160] and CrO_x.[161] We compare the influence of TiO_x as well as Ti interlayers between the metal cathode (either Ag or Al) and the hybrid absorber layer on the photovoltaic performance and the device stability

of polymer/CIS hybrid solar cells. The investigated hybrid solar cells are prepared following a ligand-free *in situ* route based on metal xanthates.[49,55] With this approach various metal sulfide nanostructures (CIS,[49,199] CdS,[200,201] Bi_2S_3,[202] Sb_2S_3[203]) have been already successfully synthesized in a conjugated polymer matrix. For the preparation of the absorber layer, copper and indium xanthates are dissolved together with a conjugated polymer. After coating this precursor solution, the precursors are converted into CIS nanoparticles in the polymer matrix by applying temperatures around 200°C. [49,199]

3.10.2 Experimental

Preparation of PSiF-DBT/CIS hybrid solar cells

The hybrid solar cells were fabricated on glass/ITO substrates (Xinyan Technology Ltd., Hong Kong) with a sheet resistance of 10 Ω /sq. After cleaning in isopropanol in an ultrasonic bath followed by O_2 plasma cleaning (FEMTO, Diener Electronic, Germany) a PEDOT:PSS hole extraction layer (Clevios P VP.Al 4083, Heraeus) was spin coated (2500 rpm, 30 s) on the substrates and subsequently heated to 150°C for 10 min in a glove box (resulting layer thickness: 40 nm). The precursor solution for the active layer, consisting of 5 mg/mL PSiF-DBT (Poly[9,9-dioctyl-2,7-silafluorene-co-alt-5,5-(4´,7´-di-2-thienyl-2´,1´,3´-benzothiadiazole)]; 1-Material, Chemsitech Inc., Canada), copper and indium xanthates (32.2 mg/mL copper *O*-2,2-dimethylpentan-3-yl dithiocarbonate, 1 equiv.; 147.8 mg/mL indium *O*-2,2-dimethylpentan-3-yl dithiocarbonate, 1.7 equiv.; Aglycon, Austria) dissolved in chlorobenzene, was deposited by doctor blading (speed: 10 mm/s, substrate temperature: 40°C). The thermal conversion was carried out on a hot plate at 195°C for 15 min (+ 15 min ramp) under N_2 (resulting layer thickness: ~60 nm). The device for the long-term stability test with a duration of 3 years was prepared according to a slightly different procedure described in a previous publication.[49]

Optionally, TiO_x interlayers (approx. 4 nm) were prepared via oxidative evaporation of titanium under medium vacuum conditions ($1x10^{-3}$ mbar, residual gas: air). Ti interlayers as well as, on top of the interlayers, the metal cathode, either aluminum or silver, were deposited under high vacuum ($5x10^{-6}$ - $1x10^{-5}$ mbar, residual gas: N_2) via

thermal evaporation through a shadow mask. The active area of the devices was 0.09 cm^2.

Solar cell characterization

PCE values of non-encapsulated devices were determined from IV curves recorded inside a glovebox directly after preparation using a Keithley 2400 SourceMeter, a custom made LabVIEW software and a Dedolight DLH400D lamp. Irradiation intensity was calibrated with a pyranometer (Kipp & Zonen).

X-ray photoelectron spectroscopy (XPS) studies were performed on a monochromatic Thermo Fisher K-Alpha spectrometer using Al Kα excitation at 1486.6 eV with a base pressure in the range of 10^{-8} to 10^{-10} mbar. Elemental scans were acquired at a pass energy of 50 eV and a step size (resolution) of 0.1 eV. The instrument work function was calibrated to give a binding energy (BE) of 83.96 eV for the Au $4f_{7/2}$ line for metallic gold. The analyses were carried out with a defined spot size of 400 µm in diameter. Depth profiling was accomplished using an argon ion source (beam energy 1000 eV) scanning over a 1×1 mm^2 area at an angle of 58° from the surface normal. Sputtering was done in different intervals starting at the side of the Ag electrode. In a first etching step (500 s) the biggest part of the Ag electrode was removed. The elemental composition of the subjacent interface was determined by defined etch (4 s per level) and measurement intervals.

Encapsulation and stability measurements

The encapsulation of the solar cells was done with a light curable epoxy resin (Ossila EE1) and an additional glass slide at the back of the solar cells. Stability data on encapsulated devices were collected under permanent illumination of 1000 W/m^2 using sulphur plasma lamps (lamp 1: LG PSH0731WA, lamp 2: Plasma International AS1300 1.1) or a solar simulator (Steuernagel KHS SC1200) according to ISOS-L-1 (level 1 laboratory testing).[72]

The active area of the encapsulated devices was 0.238 cm^2 (diameter 5.5 mm). As an exception, the device for the 3-year long-term stability test had an active area of 0.09 cm^2.

Current-voltage (IV)-curves were measured using an automated system in periodic intervals of 30 min and the devices were kept under open circuit conditions between the measurements. The automated system consists of Keithley 2400 source meters, a

Keithley 3706A multiplexer and a custom made LabVIEW based software. Irradiation intensity was calibrated with a pyranometer (Kipp & Zonen) and monitored in 30 min intervals using a Si-photodiode (Hamamatsu). No additional cooling was applied, resulting in a device temperature of 55°C during the stability tests.

3.10.3 Results and discussion

Titanium-based interlayers in PSiF-DBT/CIS hybrid solar cells were prepared by deposition of a thin layer of Ti by thermal evaporation on the polymer/nanoparticle absorber layer under two different process conditions before Ag or Al electrodes were applied. In the first case, the interlayer was deposited at comparatively low vacuum ($1x10^{-3}$ mbar) with the residual gas in the evaporation chamber being air, expecting that TiO_x is formed in the oxidative conditions during the evaporation process like it has been already demonstrated for other metal oxides.[160,161] In the second method the Ti-based interlayer was also applied by thermal evaporation but under inert gas atmosphere (N_2) in a glove box in order that metallic titanium is retained as the interlayer.

To prove the assumptions to form TiO_x and Ti interlayers via these routes, X-ray photoelectron spectroscopy (XPS) analysis combined with argon ion sputtering was carried out on typical solar cells with 4 nm Ti and 4 nm TiO_x interlayer and Ag electrodes, which exhibited PCEs of about 2%. At first glance, by monitoring the depth profiles of the atomic compositions of the solar cells, a clear difference in oxygen content could be observed (see Figure 45A and B). For the sample with the TiO_x interlayer, the atomic percentage of oxygen is in the region of the interlayer approximately twice as high as the Ti content. In the sample with the Ti interlayer deposited under inert gas atmosphere, the oxygen content is significantly lower than the Ti content. Figure 45C and D show the XPS spectra of Ti in the TiO_x and Ti interlayer. The binding energies are clearly shifted in the samples, indicating a different oxidation state of Ti in the interlayer. In the TiO_x interlayer, the binding energies of Ti $2p_{1/2}$ and Ti $2p_{3/2}$ are at 464.8 and 459.0 eV, respectively, which match well with the Ti^{4+} oxidation state of TiO_2.[197,204] However, the peaks are quite broad, which leads us to the conclusion that also some amounts of the suboxide Ti_2O_3 with binding energies of 462.7 and 457.3 eV for Ti $2p_{1/2}$ and Ti $2p_{3/2}$, are present in the sample.[204]

In the sample with the Ti interlayer, the predominant peaks at 460.3 and 454.2 eV can be attributed to metallic Ti(0). The minor peaks in the spectrum at 461.5 and 455.9 eV may stem most presumably from titanium in Ti^{2+} oxidation state,[205] which gives the hint that, in addition to metallic Ti as main component, also small amounts of TiO are present in this sample.

The oxygen 1s spectrum, presented in Figure 45E, shows a distinct peak at approx. 530.7 eV for the TiO_x interlayer, which matches with literature data,[197] while in the sample with the Ti interlayer the oxygen 1s peak is very weak and hardly distinguishable from the background signal (see Figure 45F).

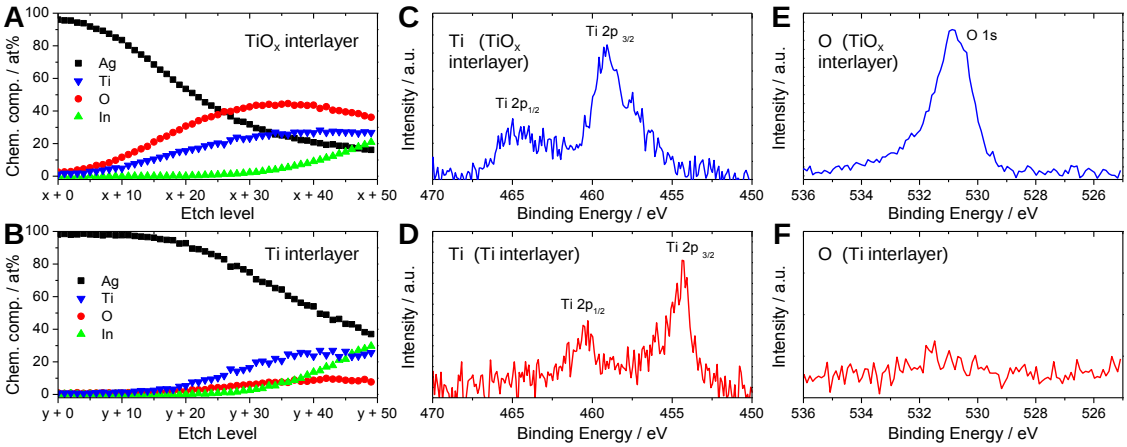

Figure 45: XPS depth profiles of PSiF-DBT/CIS hybrid solar cells with TiO_x/Ag (A) and Ti/Ag (B) electrodes for the elements Ag, Ti, O, and In. The content of the elements is given in atomic percent and plotted versus etch level starting from the side of the Ag electrode. X and y denote the sputtering time needed to penetrate the comparatively thick (approx. 200 nm) Ag electrode. XPS spectra of Ti (C,D) and O (E,F) in the TiO_x and Ti interlayer of the prepared hybrid solar cells acquired at etch level x + 10 for the TiO_x and y + 16 for the Ti sample.

XPS measurements proved that deposition of TiO_x interlayers via thermal evaporation under moderate vacuum conditions in ambient atmosphere is viable. Thus, this technique was used to prepare hybrid solar cells with TiO_x and Ti interlayers and Ag as well as Al electrodes. Based on this set of devices, the influences of the interlayers and interlayer-electrode combinations on the device performance as well as on the lifetime of the solar cells were investigated.

First, we focus on the device characteristics. To find out the optimal thickness of the TiO_x interlayer between the PSiF-DBT/CIS absorber layer and the Ag electrode, a series of solar cells with different interlayer thicknesses between 0 and 20 nm was prepared. The characteristic parameters of the solar cells prepared in this series are summarized in Figure 46.

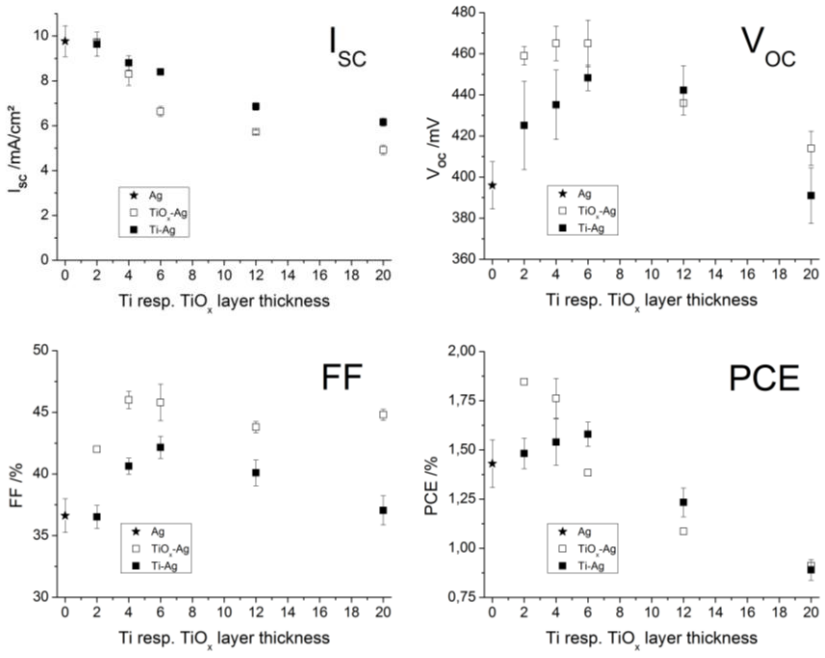

Figure 46: Dependence of the characteristic solar cell parameters I_{SC}, V_{OC}, FF and PCE on the thickness of the TiO_x and Ti interlayer in glass/ITO/PEDOT:PSS/PSiF-DBT:CIS/TiO_x or Ti interlayer/Ag solar cells (mean values and standard deviation of the best five cells of each series).

The short circuit current (I_{SC}) showed a maximum at a TiO_x interlayer thickness of 2 nm and decreased with increasing thickness of the interlayer. The open circuit voltage (V_{OC}) increased from about 390 mV without interlayer to values of about 460 mV for 2-6 nm thick TiO_x layers, before it decreased again. The fill factor (FF) increased up to a TiO_x thickness of 4 nm and stayed quite constant towards higher interlayer thicknesses. The PCE values showed a clear maximum at interlayer thicknesses of 2 and 4 nm. These observations are similar to the results of a study on poly(3-hexylthiophene-2,5-diyl) (P3HT)/PCBM bulk heterojunction solar cells by Hayakawa et al.,[191] where it was also found that the reason for a PCE increase by introducing a thin TiO_x interlayer is rather an increase in FF than in I_{SC}. The improvement of the FF can be ascribed to a higher shunt resistance (R_{sh}) in the devices with TiO_x interlayer, which stems most

presumably from the hole blocking effect of the TiO_x layer.[191] The values of series (R_s) and shunt resistances of typical solar cells with bare Ag or Al electrodes as well as with the Ti-based interlayers (thickness: 4 nm) are given in Table 8.

As shown in Figure 46, the V_{OC} is increased from approx. 390 mV for devices with Ag electrodes to about 460-480 mV for devices with a Ti-based interlayer, which is also similar to the V_{OC}-values obtained using Al electrodes (see also Table 1). We assume that the reason for this increase in V_{OC} is based on the different values for the work function or the conduction band (in the case of TiO_x) of the used electrode and interlayer materials. Even though, quite similar wok functions are found in databases and literature for Ag (4.26 eV)[206] and Al (4.28 eV),[206] we assume, as the V_{OC} of the solar cells with Ag electrodes is significantly lower than for devices with Al electrodes, that the effective work function of Ag in the prepared devices is shifted further from vacuum,[207,208] which is reported to be caused by small amounts of oxygen.[209] The conduction band of TiO_x has a value of approx. 4.4 eV[210] and lies in the range of the work function of Al (4.28 eV) and also Ti (4.33 eV),[206] which causes the increased V_{OC}, whereas the valence band is around 8.1 eV[194] acting as an efficient barrier for holes.[158] The reasons for the lower I_{SC} of the devices with interlayers found in our study are tentatively the processing conditions. On the one hand the solar cells with TiO_x interlayer had to be handled in air for a certain time, which affects the I_{SC} adversely, and on the other hand, the solar cells were subjected to a higher thermal stress during the thermal evaporation process of Ti for which higher temperatures were needed compared to Ag or Al. The decrease of all the characteristic solar cell parameters I_{SC}, V_{OC} and FF for devices with TiO_x interlayers having thicknesses of over 10 nm can be referred to the low conductivity of TiO_x, which becomes an issue at higher interlayer thicknesses.[191]

An analogous series was carried out for the implementation of Ti interlayers (see also Figure 46). Similar to the TiO_x interlayers, the I_{SC} values decreased with increasing layer thickness. The V_{OC} as well as the FF had maxima at a layer thickness of 4 - 6 nm, and thus, also the PCE had its maximum at a layer thickness of 6 nm. Also in the case of Ti interlayers, the most prominent effect of the interlayer is on the fill factor (decrease of R_s) and on V_{OC}, which might be caused by better charge extraction properties and a better suited work function of the Ti layer.

Based on the results of these series of solar cells, further experiments were carried out with interlayer thicknesses of 4 nm, as in the case of TiO_x interlayers the PCE is almost as high as with 2 nm interlayer thickness and V_{OC} as well as FF show a maximum at this thickness and in the case of Ti interlayers, the solar cells with 4 nm interlayers are also almost reaching similar PCE values as for 6 nm interlayer thickness.

Figure 47 shows the IV-characteristics of representative hybrid solar cells with Ag and Al electrodes and Ti as well as TiO_x interlayers with a thickness of 4 nm.

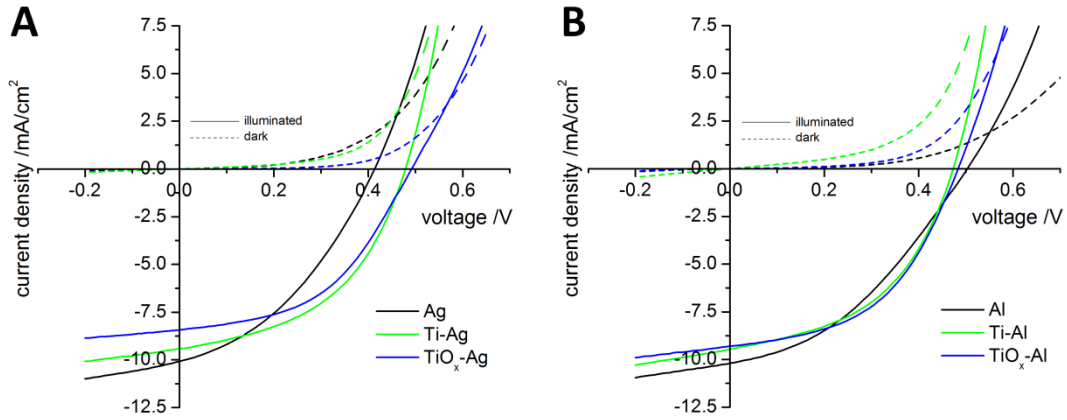

Figure 47: Typical IV-curves in the dark (dashed lines) and under 100 mW/cm² illumination (full lines) of PSiF-DBT/CIS hybrid solar cells with Ag electrodes and TiO_x as well as Ti interlayers (A) and Al electrodes as well as TiO_x and Ti interlayers (B).

The characteristic solar cell parameters extracted from the IV curves are summarized in Table 8.

Table 8. Characteristic solar cell parameters of PSiF-DBT/CIS hybrid solar cells prepared with different cathode materials.

Cathode Material	V_{OC} / mV	I_{SC} / mA/cm²	FF / %	PCE / %	R_s / Ω*cm²	R_{sh} / Ω*cm²
Ag	416	10.07	37.9	1.58	20	170
TiO_x-Ag	497	8.42	47.0	1.96	22	450
Ti-Ag	477	9.41	47.5	2.12	13	340
Al	507	10.18	38.0	1.93	27	160
TiO_x-Al	487	9.29	48.4	2.29	15	230
Ti-Al	477	9.45	47.0	2.09	13	180

The most obvious difference in the series prepared with Ag electrodes is the significant difference in FF as well as photovoltage, which is caused by the improved R_{sh} in the devices, as discussed above. The V_{OC} is improved from 416 mV for a bare Ag electrode to 497 mV for devices with TiO_x interlayer and to 477 mV with Ti interlayer. This is due to a less favorable work function difference to the opposite PEDOT:PSS hole extraction layer using bare Ag electrodes, as described before. Even though the I_{SC} is reduced in both cases compared to bare Ag electrodes, the PCE is significantly higher due to the higher V_{OC} as well as a distinct improvement in FF. While with PSiF-DBT/CIS solar cells with Ag electrodes PCEs of typically 1.6% are reached, devices with TiO_x or Ti interlayers show quite similar efficiencies of 2 and 2.1%, respectively. Concerning the solar cells prepared with Al electrodes instead of Ag electrodes, the major difference is detected in FF, which is clearly improved by the incorporation of the TiO_x or Ti interlayers. This increased FF when using TiO_x or Ti interlayers leads to PCEs of 2.3 and 2.1%, respectively, which are higher compared to the device with bare Al electrodes (PCE: 1.9%). A similar improvement in FF was also already detected by modifying the Al electrodes with a thin Ag interlayer.[97] The V_{OC} values of TiO_x/Al and Ti/Al are similar to those of TiO_x/Ag and Ti/Ag and are thus determined by the interlayer.

In a next step, we first focused on the stability of the PSiF-DBT/CIS hybrid solar cells with Ag electrodes. Based on our previous studies, the stability of the solar cells with Al electrodes has been evaluated to be problematic.[49] Figure 48A shows a lifetime test of a glass/glass encapsulated PSiF-DBT/CIS solar cell with Ag electrodes, prepared according to Ref. 49, over a time of 4600 h under continuous illumination with a sulphur plasma lamp and IV curves being measured every 30 min to monitor the characteristic solar cell parameters over time.

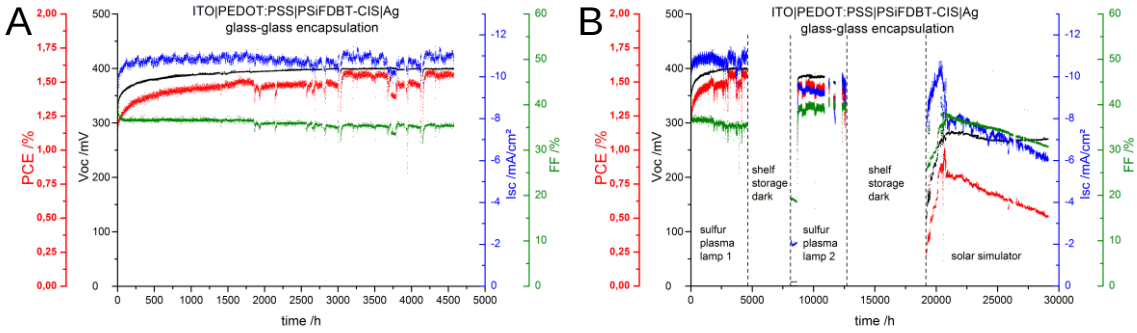

Figure 48: Stability test of a PSiF-DBT/CIS hybrid solar cell with Ag electrodes: (A) First 4600 h of illumination using a sulphur plasma lamp; (B) Results of the prolonged stability test of this solar cell in the time frame of about 3 years (approx. 28500 h). Due to technical issues, the test was performed using three different lamp systems: two sulphur plasma lamps 1 (LG) and 2 (Sulphurplasma International), and a solar simulator (Steuernagel).

It can be clearly seen from the graph that the solar cell showed a very stable behavior during this test. In the first about 300 h the I_{SC} and the V_{OC} increased to 120% and 130% of their initial value, respectively, and the FF decreased to about 90% of the start value in the very first hours. This burn-in phase led to an overall increase of the PCE to 120% of the initial value. The PCE stayed constant throughout the whole period of this lifetime test. The end of this lifetime test was determined by the breakdown of the used sulphur plasma lamp. The solar cell was stored in the dark until a new lamp was available and the stability test was continued, which is shown in Figure 48B. Unfortunately, there were also problems with the second sulphur plasma lamp leading to voids in the graph. Nevertheless, after a short burn-in phase, the solar cell showed the same constant PCE for 2700 more hours under illumination. After a second shelf storage in dark conditions (approx. 7000 h), the test was continued using a solar simulator. In this test phase the burn-in phase was much longer. All the solar cell parameters increased for approx. 2000 hours, before they more or less stabilized.

However, all the solar cell parameters were significantly lower than before leading to a drop in PCE. In the further course of the stability test (approx. 7200 h), all the solar cell parameters of the solar cell decreased slightly, but steadily. However, even after this test, which had an overall duration of about 3 years (28500 h, whereof 16900 h under illumination with 1000 W/m^2) approx. 50% of the initial PCE of the solar cell have been conserved. Due to the fact that the solar cell performance was very constant in the first 4600 h of the test (and also in the 3240 illuminated hours of the second phase) we assume that the decrease in performance in the third test phase is mainly caused by the failing of the encapsulation material and that the CIS/polymer hybrid absorber material is stable if suitably encapsulated.

However, it was also observed in some solar cells with Ag electrodes, that after a certain time frame of stable operation, the FF decreases as shown, for example, in Figure 49D. The prompt and drastic decrease of the FF could stem from failing of the encapsulation, or it may give a hint that Ag diffusing through the absorber layer leading to partial shunting of the device might be the reason for this behavior.[143] Therefore, TiO_x or Ti interlayers could be interesting materials to solve this problem, as they may provide a barrier for Ag-diffusion in and through the absorber layer. Moreover, these Ti-based interlayers could also solve problems concerning the weak stability of solar cells with Al electrodes. Thus, the stability of PSiF-DBT/CIS hybrid solar cells with and without TiO_x and Ti interlayers and Al and Ag electrodes were investigated in more detail. The results of the long-term measurements are shown in Figure 49. Representative IV-curves of these solar cells at various points in time are included in the supporting information (chapter 3.10.5).

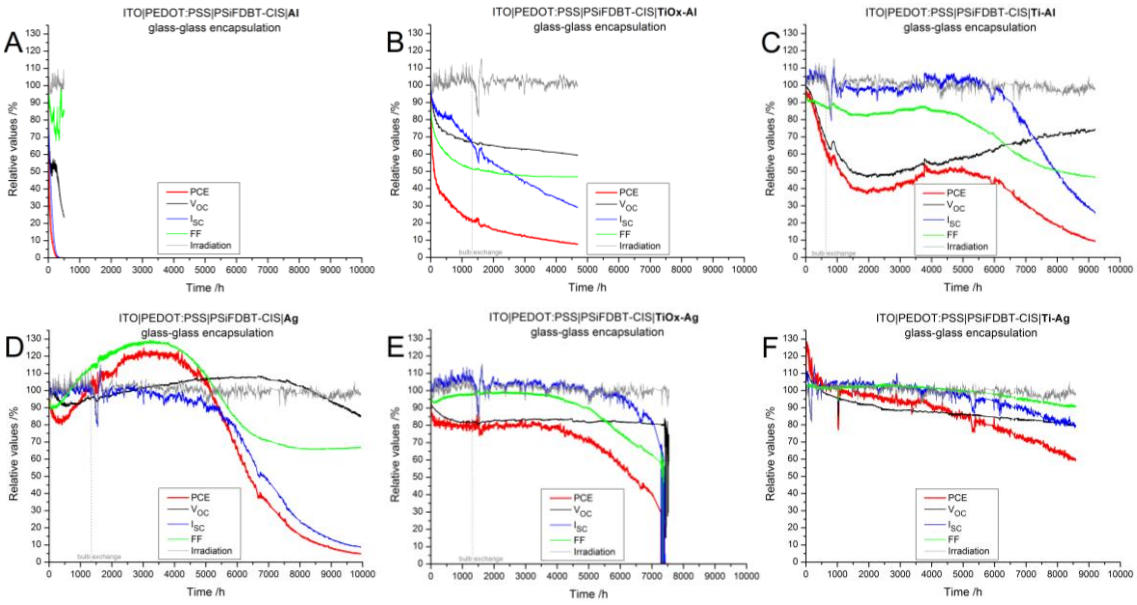

Figure 49: Lifetime tests of glass/glass encapsulated PSiF-DBT/CIS hybrid solar cells with Al (A), TiO_x/Al (B) and Ti/Al (C) electrodes as well as Ag (D) TiO_x/Ag (E) and Ti/Ag (F) electrodes performed under continuous illumination using a solar simulator. The grey lines represent the actual illumination intensity during the performed stability test.

Testing the stability of a set of encapsulated solar cells prepared with Al electrodes and TiO_x as well as Ti interlayers, it turned out that the lifetimes of the devices could be improved to some extent by the Ti-based interlayers. In the case of the device with Al electrodes prepared without interlayer, after 250 h of continuous illumination, the solar cells were completely degraded, which was mainly caused by the decreasing I_{SC} (see Figure 49A). It has to be noted that the devices with Al electrodes partly degraded during the encapsulation process, although this was carried out in a glovebox. The stability of the solar cells was significantly improved by introducing a TiO_x interlayer between the active layer and the Al electrode, see Figure 49B. While the V_{OC} and FF stayed quite constant after a burn-in phase of about 500 h, the I_{SC} decreased steadily - a quite similar behavior as before with bare Al, which caused a deterioration of the solar cells to about 10% of its initial PCE after about 4000 h. The solar cell with Ti/Al interlayer/electrode combination exhibited the most stable behavior in this series using Al electrodes (see Figure 49C). In this case, the I_{SC} as well as the FF were very stable, and the V_{OC} was responsible for the drop of the PCE to about 40% of its initial value in the first 1500 h of testing time. After that, the V_{OC} started to increase slightly, which implies also a slight recovery of the PCE during the next 3000 h of the stability test, before the FF started to decrease. After a testing time of 6500 h, also the I_{SC} decreased steeply and after 9000 h only 10% of the initial PCE remained.

Analyzing the stability data of the set of devices prepared with Ag electrodes (Figure 49D-F), it can be seen, that in the first two graphs the FF also started to degrade significantly at a test time between 4000 to 5000 hours. The reason for this observation could be a failure of the device encapsulation (glass/glass, epoxy glue, without edge sealing), however, also a shunting of the devices due to migration of the metal from the electrode through the absorber layer is likely. Generally, the solar cells prepared with Ag electrodes are much more stable than the devices with Al electrodes. While I_{SC} and V_{OC} of the device with bare Ag electrodes maintained more or less their initial value in the first 4000 hours of the test, the FF, after a decrease in the very first hours, increased to about 125% of its initial value before it started to decrease steeply after 4500 h. After this point, also the I_{SC} started so diminish, while the FF stabilized again at 70% of its initial value after 8000 h. The behavior was quite similar in the device with TiO_x interlayer and Ag electrodes. The I_{SC} and V_{OC} were, after a burn-in phase, in which the V_{OC} slightly went down, fairly stable. The FF increased a bit in the first hours of the test and stayed stable until it again started to decrease at about 4000 – 4500 h of test duration, before the solar cell completely failed after 7300 h of continuous illumination, most likely due to shunting of the device.

After some initial degradation during the encapsulation process, the solar cell with a Ti interlayer and Ag electrodes showed the most stable performance in this series. The stability data are presented in Figure 49F. It was observed that the FF was quite stable over the whole testing period. After 8500 h, the FF still exhibited 90% of its starting value, which shows that no indications for device shunting are observed during the lifetime testing in this case. The V_{OC} dropped slightly at the beginning and the I_{SC} started to decrease after 5000 h and so about 90% of the initial PCE were retained after a testing period of 4000 h and about 60% after 8500 h of continuous illumination.

Among the investigated series of devices with Ag or Al electrodes, the best stabilities were obtained with devices having Ti interlayers. Improved stability properties using Ti/Al bilayer electrodes were also found for small-molecular organic solar cells by Cao et al.[164] The superior stability of the polymer/nanoparticle hybrid solar cells with Ti interlayers compared to the solar cells with TiO_x interlayers might be due to the partly processing of the devices with TiO_x interlayer in air (before and after deposition of the TiO_x interlayer) but also due to an additional oxygen scavenging effect of the Ti interlayer.

3.10.4 Conclusion

Summing up, the thermal evaporation of Ti under moderate vacuum conditions in oxygen containing atmosphere outlines a smart method for the preparation of thin TiO_x coatings for OPV applications. The thicknesses of the TiO_x layers can be adjusted easily and also the subjacent absorber layer is not influenced by any solvent used in solution based processes.

The as prepared TiO_x layers as well as the Ti layers, deposited in oxygen free conditions, were applied as interlayers in PSiF-DBT/CIS hybrid solar cells and a positive influence of both the interlayers on the solar cell performance was observed. Polymer/CIS hybrid solar cells showed the best PCEs with Al electrodes so far,[49] however, the limited stability of this electrode is an issue. In contrast, devices with Ag electrodes, showed, if no catastrophic failure is observed due to Ag diffusion and device shunting, extraordinary stable behavior. A PSiF-DBT/CIS hybrid solar cell with Ag electrodes was tested, including some breaks, over a time range of about 3 years and still approx. 50% of its initial PCE are maintained. However, these solar cells suffer from a lower V_{OC} compared to Al electrodes, which limits their PCEs.

By introducing TiO_x as well as Ti interlayers between absorber layer and Ag electrodes, enhanced V_{OC} and FF values could be observed, which led to an increase in PCE from 1.6 to about 2.1%, and, in particular, with a Ti interlayer the hybrid solar cells show stable performance over a testing period of several thousand hours and after an overall testing period under continuous illumination of 8500 h 60% of the initial PCE are retained.

The introduction of TiO_x and Ti interlayers enhances also the stability of solar cells with Al electrodes, but their lifetimes are still not comparable with devices using Ag electrodes. Overall, the results concerning stability of polymer/nanoparticle hybrid solar cells gained in this study are quite encouraging and show that the lifetimes of *in situ* prepared hybrid solar cells using metal xanthates as precursors are comparable with lifetimes of polymer/PCBM solar cells, if appropriate interlayer/electrode combinations and proper encapsulation are used.

3.10.5 Supporting information for: Influence of TiO_x and Ti cathode interlayers on the performance and stability of hybrid solar cells

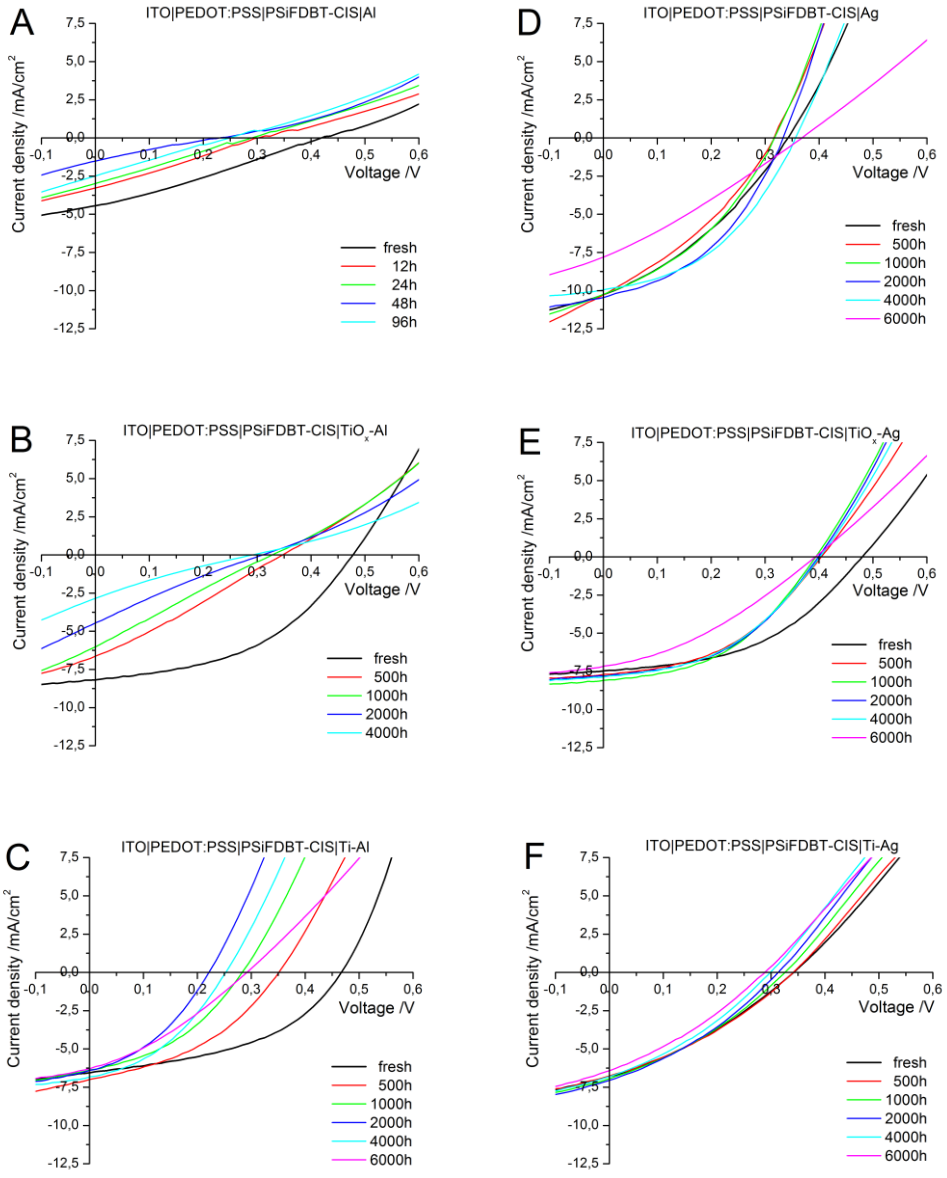

Figure 50: IV-curves of glass/glass encapsulated PSiF-DBT/CIS hybrid solar cells with Al (A), TiO_x-Al (B) and Ti-Al (C) electrodes as well as Ag (D) TiO_x-Ag (E) and Ti-Ag (F) electrodes measured at different times during the stability tests.

3.11 Influence of a solution processed TiO_x cathode interlayer on the performance and stability of hybrid solar cells

In this series of experiments the already mentioned solution processed preparation of TiO_x interlayer via an "activated" titanium tetraisopropoxide precursor that allows conversion temperatures around 80°C was introduced.[158] Due to the moderate conversion temperature is this route applied to obtain TiO_x for the formation of cathode interlayer in regular architecture solar cells.

The TiO_x precursor solution was prepared according to Cho et al.[211] After deposition via spincoating on the absorber layer, was the precursor layer heated for 10 minutes at 80°C in air. This procedure leads to TiO_x layer thicknesses in the range of 30-40 nm.[192]

Hybrid solar cells in the architecture ITO|PEDOT:PSS|PSiFDBT-CIS|TiO_x(solution processed)-Al showed poor photovoltaic performance direct after fabrication. During repeated electrical characterizations after dark storage overnight, exhibited the devices significantly enhanced I_{SC}, V_{OC} and FF values, thus maximum PCE values have been obtained after a storage time of 10 days. This led to the assumption that the chemical conversion of the TiO_x precursor has not been fully taken place under the applied conditions. In a next step, reaction time has been prolonged to 15 minutes and reaction temperature has been elevated to 90°C, 95°C and 100°C. Again, solar cells showed an increase in PCE after dark storage over several days, while best results in terms of PCE have been obtained at a reaction temperature of 90°C for 15 minutes. These optimizations have been carried out by Elisabeth Schwarz in the frame of a project laboratory. At higher conversion temperatures the PCE maxima are reached earlier, controversially devices showed poorer performance.

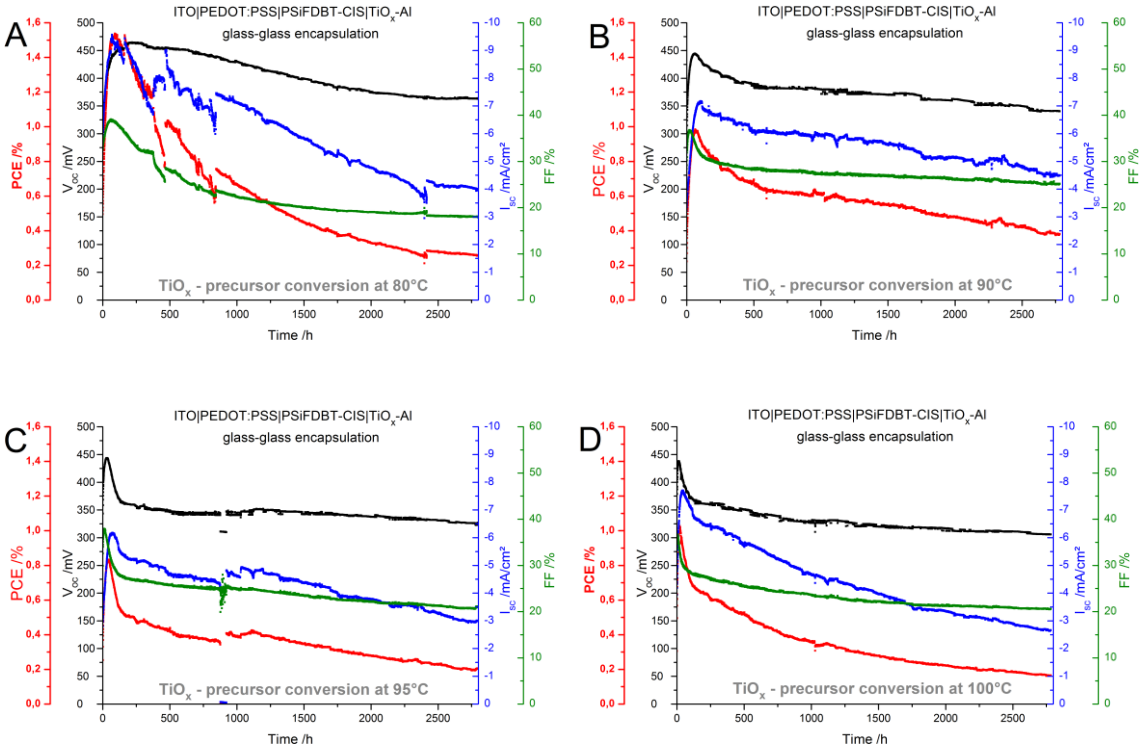

Figure 51: Evolution of the characteristic electric parameters of encapsulated hybrid solar cells with the architecture ITO|PEDOT:PSS|PSiFDBT-CIS|TiO_x(solution processed)|Al over time under permanent illumination using a solar simulator. The TiO_x precursor has been converted at (A) 80°C, (B) 90°C, (C) 95°C and (D) 100°C for 15 minutes on air.

Figure 51 shows the evolution of the characteristic electric parameters of encapsulated hybrid solar cells with the architecture ITO|PEDOT:PSS|PSiFDBT-CIS|TiO_x(solution processed)|Al over time under permanent illumination. The conversion of the TiO_x-precursor has been carried out for 15 minutes on air at 80°C (A), 90°C (B), 95°C (C) and 100°C (D), respectively. All four devices exhibit PCE values below 0.5% direct after fabrication and encapsulation. During the first hours of operation, PCE-values increase steadily, reaching a maximum after a certain time before device degradation occurs. As can be seen, the higher the conversion temperature of the TiO_x precursor, the earlier the PCE maximum is reached. In respect of stability, all four devices show distinct degradation in the first thousand hours of operation. In this experiment, the solar cell where the TiO_x precursor has been converted at 80°C shows best results in terms of efficiency; IV-curves direct after encapsulation and at the performance peak as well as the corresponding characteristic parameters can be found in Figure 53 and Table 9, respectively. The solar cell where the TiO_x precursor has been converted at 90°C shows the most stable behaviour, nevertheless the PCE of this device only reached 1.0% after

burn in phase. Solar cells with a solution processed TiO_x interlayer in combination with Al electrodes exhibit a better stability than the device with an evaporated TiO_x interlayer in combination with an Al electrode (see Figure 49).

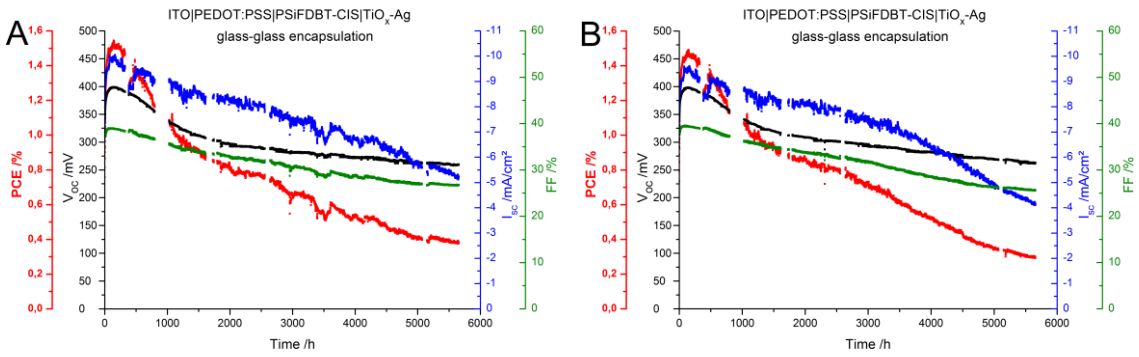

Figure 52: Evolution of the characteristic electric parameters of encapsulated hybrid solar cells with the architecture ITO|PEDOT:PSS|PSiFDBT-CIS|TiO_x(solution processed)|Ag over time under permanent illumination using a solar simulator. The TiO_x precursor has been converted at 90°C for 15 minutes on air.

Figure 52A and B show the evolution of the characteristic electric parameters of two encapsulated hybrid solar cells with the architecture ITO|PEDOT:PSS|PSiFDBT-CIS|TiO_x(solution processed)|Ag over time under permanent illumination. The TiO_x precursor conversion has been conducted at 90°C for 15 minutes on air. Again, PCE-values have been relative low (~0.75%) direct after fabrication and reach maximum values (~1.5%, see Figure 53 and Table 9) after 140-150 hours of operation before device degradation occurs. In comparison with solar cells with aluminium electrodes (Figure 51), these devices show slightly higher stability whereas a solar cell with an evaporated TiO_x interlayer in combination with a silver electrode showed better results (see Figure 49).

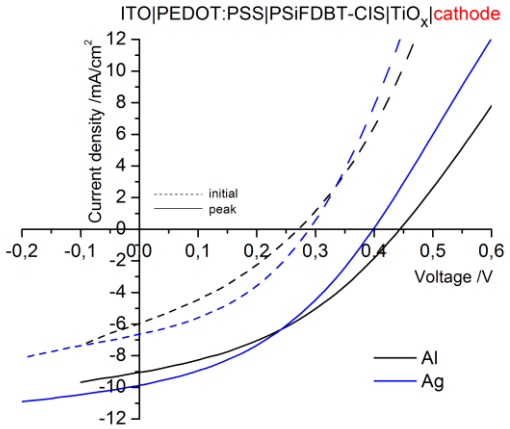

Figure 53: IV-curves of PSiFDBT-CIS hybrid solar cells with solution processed TiO_x cathode interlayers direct after encapsulation and at their performance peak after burn-in phase.

Table 9: Characteristic electric parameters of PSiFDBT-CIS hybrid solar cells with solution processed TiO_x cathode interlayers at their performance peak after burn-in phase.

Cathode Material	V_{OC} / mV	I_{SC} / mA/cm²	FF / %	PCE / %
Al	443	9.05	38.7	1.54
Ag	399	9.87	38.9	1.54

In Figure 53, IV-curves of PSiFDBT-CIS hybrid solar cells with solution processed TiO_x cathode interlayers in combination with aluminum and silver electrodes direct after encapsulation and at their performance peak after burn-in phase are presented.

Table 9 shows the corresponding electric parameters of the devices at their performance peak. While showing high I_{SC}-values, V_{OC}- and FF-values are lower and thus PCEs are lower compared to solar cells with evaporated TiO_x cathode interlayers (see Figure 47 and Table 8).

3.12 Solution processed V_2O_5 as anode interlayer

In further experiments concerning the search of an adequate substitution of PEDOT:PSS, the oxides MoO_3, WO_3 and V_2O_5 have been evaluated for their application as anode interlayers. These experiments have been carried out by Eva Lackner in the frame of a project laboratory. In this series of experiments, the V_2O_5 interlayer showed best results and thus the influence of this interlayer on the operational stability was examined. The preparation conditions of the solution processed precursor have been adapted from Zilberberg et al.[212]

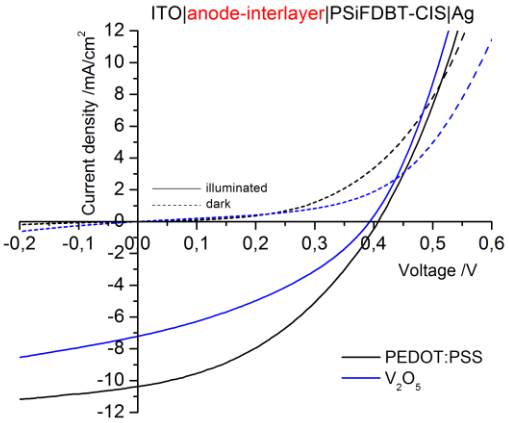

Figure 54: IV-curves of PSiFDBT-CIS hybrid solar cells with a PEDOT:PSS and a V_2O_5 anode interlayer under illumination and in the dark.

Figure 54 and Table 10 show IV-curves and the corresponding characteristic electric parameters of PSiFDBT-CIS hybrid solar cells with a PEDOT:PSS and a V_2O_5 anode interlayer, respectively.

Table 10: Characteristic parameters of PSiFDBT-CIS hybrid solar cells with a PEDOT:PSS and a V_2O_5 anode interlayer.

Anode-Interlayer	V_{OC} / mV	I_{SC} / mA/cm²	FF / %	PCE / %
PEDOT:PSS	408	10.4	39.6	1.66
V_2O_5	393	7.20	36.5	1.03

To get insight in the influence of the V_2O_5 anode interlayer on the stability of hybrid solar cells, the performance over time of these two cells has been monitored without encapsulation in air under permanent illumination (Figure 55).

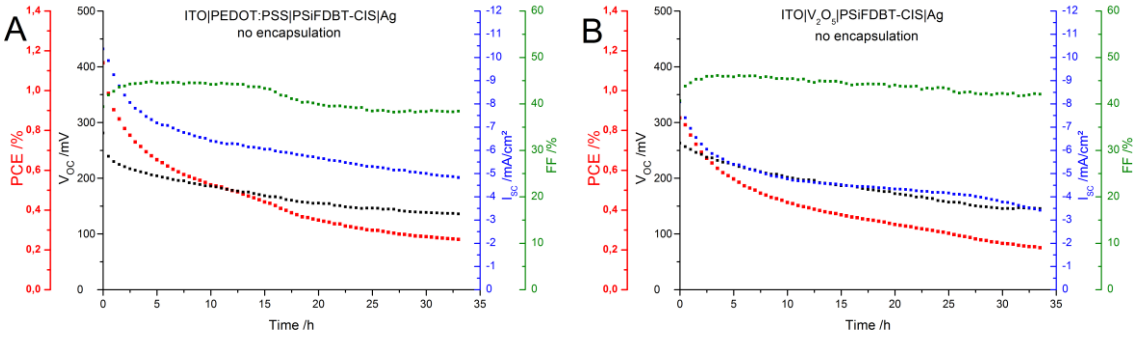

Figure 55: Lifetime tests of PSiFDBT-CIS hybrid solar cells with a PEDOT:PSS (A) and a V_2O_5 (B) anode interlayer performed in air under continuous illumination using a solar simulator.

As can be seen in Figure 55, degradation of both cells is in the same extent. As observed in previous stability experiments carried out in air without encapsulation, the V_{OC} of both solar cells drops immediately to values around 250 mV when the devices are exposed to ambient atmosphere. During the next 24 hours the V_{OC} further decreases to values below 160 mV. The FF in contrast shows stable behaviour and stays above 40% in the first 24 hours. In both cells, the I_{SC} decreases significantly during the first 5 hours of operation and reaches ~52% of its initial value after 24 hours. Thus, after 24 hours of operation, the PCE of the solar cell with a PEDOT:PSS anode interlayer shows 27% and the cell with a V_2O_5 interlayer shows 34% of its initial value in air. Compared with stability results obtained under illumination with the sulphur plasma lamp (see Figure 23 and Figure 28), it can be seen that devices without encapsulation degrade in a significantly higher degree when illuminated with the solar simulator; most likely due to the lack of UV light in the spectrum of the sulphur plasma lamp.

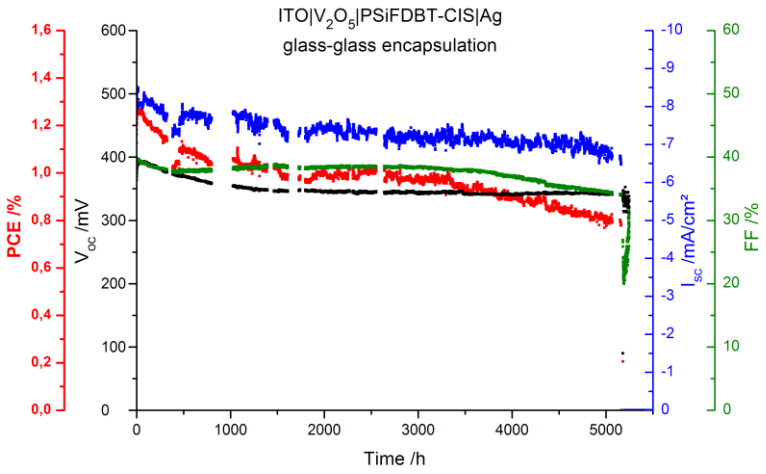

Figure 56: Lifetime test of an encapsulated PSiFDBT-CIS hybrid solar cells with a V_2O_5 anode interlayer performed under continuous illumination using a solar simulator.

An encapsulated hybrid solar cell with a V_2O_5 anode interlayer (Figure 56) exhibited initially a V_{OC} of 397 mV, an I_{SC} of 8.47 mA/cm², a FF of 39.7% and a PCE of 1.29%. After a burn in period of about 1000 hours, reducing the PCE to ~1.0%, the device showed stable behaviour for the next 2200 hours before the PCE declines to 0.8% until a fatal device failure occurred after 5000 hours of illumination.

Again, device degradation is expected to be caused by Ag migration through the absorber layer, thus the introduction of the V_2O_5 anode interlayer could not prevent the failure after ~5000 hours of testing. The result that the encapsulated solar cell with a V_2O_5 anode interlayer shows similar behaviour to devices with PEDOT:PSS interlayers led to the assumption that PEDOT:PSS does not cause enhanced device degradation within the observed periods.

3.13 Impact of oxygen and water on the stability of hybrid solar cells with Ag electrodes

To get insights into the influence of water and oxygen on the degradation behavior of hybrid solar cells with silver electrodes, ageing experiments under different atmospheres (i.e. dry nitrogen, H_2O enriched nitrogen, dry synthetic air and H_2O enriched synthetic air) have been conducted. For that purpose, a sealed measuring chamber equipped with gas inlet and outlet, a quartz glass window, electrical connections and an internal Si-photodiode has been constructed that allowed the monitoring of several individual solar cells. The gas outlet was equipped with a gas bubbler filled with silicone oil to exclude air intake from the environment and check the gas flow through the chamber (by counting the bubbles). Optionally a water reservoir was implemented into the gas inlet to enrich the gas-filled compartment with humidity. With this construction relative humidity values of >90% at 22°C could be obtained. Due to a limited H_2O reservoir volume, only the first 400 hours of operation (the burn-in period) could be studied. Figure 57A-D shows the behavior of the characteristic electric parameters (PCE, V_{OC}, I_{SC} and FF) over time of three hybrid solar cell in different environments (dry nitrogen, H_2O enriched nitrogen, dry synthetic air and H_2O enriched synthetic air).

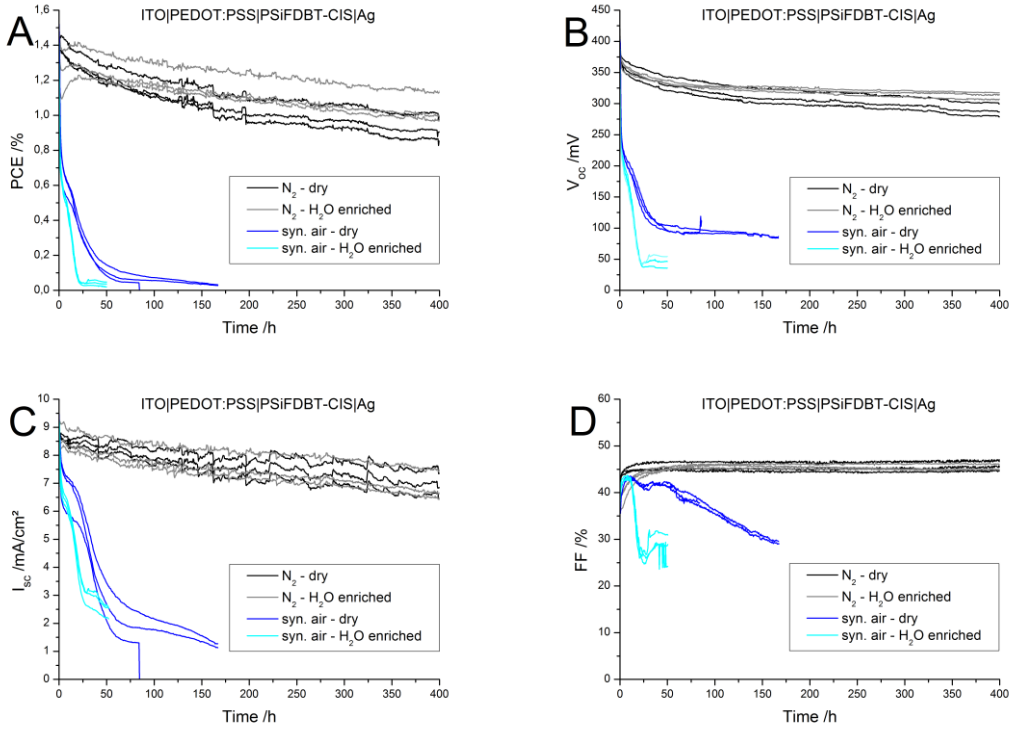

Figure 57: Characteristic parameters (A) PCE, B) V_{OC}, C) I_{SC}, D) FF) of PSiFDBT-CIS hybrid solar cells with silver electrodes over time in different gas atmospheres under permanent illumination using a solar simulator.

The dry nitrogen atmosphere acts as reference and reflects an encapsulation as comparable results to glass-glass encapsulated devices (see stability tests in previous chapters) could be obtained. PCE´s of solar cells in dry nitrogen atmosphere show a decrease to 65-75% of initial values. Interestingly, hybrid solar cells in H_2O enriched nitrogen atmosphere show absolutely no enhanced degradation compared to the dry nitrogen atmosphere at device temperatures around 55°C. From the experiments conducted in dry synthetic air environment, it can be seen that devices age in a much faster degree. The initial V_{OC} drop to ~60% of initial values occurs immediately as observed at non-encapsulated devices with silver electrodes. It can be concluded that this distinct initial voltage drop is caused by oxygen. Also the other electrical parameters (PCE, I_{SC} and FF) show similar behavior as non-encapsulated devices, thus oxygen is the predominant factor for device degradation. In the case of the H_2O enriched synthetic air environment, solar cells degrade faster compared to dry synthetic air. It can be concluded that humidity in the absence of oxygen does not cause additional device failures, while humidity in the presence of oxygen accelerates degradation.

Nikiforov et al. performed duration tests with P3HT-PCBM solar cells encapsulated with two different polymeric encapsulation materials: Kapton and polyethylene terephthalate (PET) and obtained similar results.[213] Both materials show similar oxygen diffusion coefficients (i.e. 2-7*10^{-13} m²/s and 3-6*10^{-13} m²/s, respectively) but different H_2O diffusion coefficients (i.e. 1,4-3,5*10^{-13} m²/s and 2,1-12,6 m²/s, respectively). Time required for 20% change in PCE in Kapton-encapsulation was 78 hours and in PET-encapsulation was 43 hours. The results also in accordance with the findings of Hintz et al. where humidity in the absence of oxygen does not cause significant degradation in P3HT, whereas the presence of humidity during the photo oxidation of P3HT increases the reaction rate significantly.[113]

3.14 Influence of load on the degradation behavior of hybrid solar cells with Ag electrodes

In all stability measurements presented in the previous chapters, the solar cells have been kept at open circuit conditions between collecting IV-curves. The benefit of this type of testing is that multiple devices can be electrically characterized in sequence with only one source meter. As a consequence of the open circuit condition, no charges are extracted between the measurements, what possibly falsifies real-world conditions where the solar cells operate at maximum power point (mpp). One possibility to circumvent this issue is the introduction of a passive load (resistor) that keeps the device at its mpp, however the passive load has to be disconnected during collecting IV-curves and resistance has to be adapted during degradation. Another possibility is the use of an active load, where a source meter always keeps the device at its actual mpp between collecting IV-curves. In order to evaluate the impact of the load condition during ageing of hybrid solar cells, have two identically prepared devices been monitored under different measuring conditions in parallel.

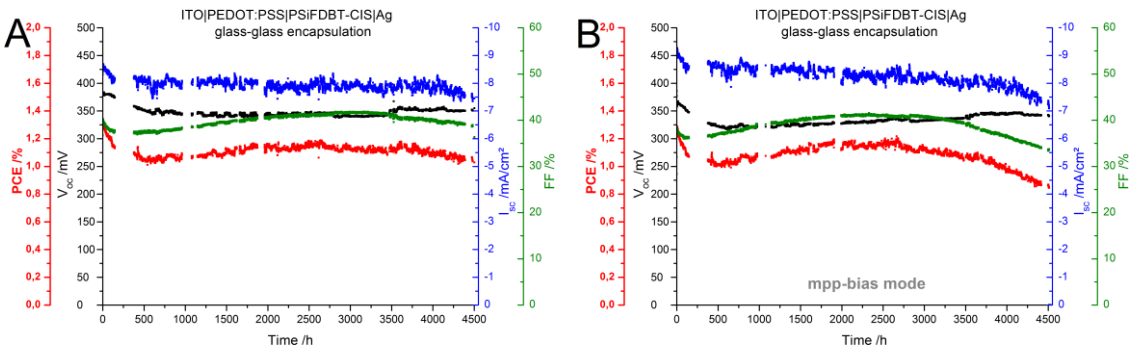

Figure 58: Lifetime tests of two glass-glass encapsulated PSiFDBT-CIS hybrid solar cells with silver electrodes performed under continuous illumination using a solar simulator. One device has been kept at open circuit conditions (A) and the other has been kept at its maximum power point (B) between collecting IV-curves.

Figure 58 shows the result of the stability measurement of encapsulated hybrid solar cells with the architecture ITO|PEDOT:PSS|PSiFDBT-CIS|Ag. One device has been kept at open circuit condition (Figure 58A) and another one has been kept at mpp condition with the aid of an active load (Figure 58B) between the electrical characterizations. As observed in earlier experiment, the solar cells show a burn-in period of ~500 hours where the PCE drops from initially 1.3% to ~1.0%, followed by a relative stable performance over the next 3000 hours; till that time, degradation of both devices is in the same range. After that period, a slight decrease in I_{SC} and a reduction in FF can be observed, particularly in the case of the device that has been kept at mpp, lowering the PCE of this device to 0.86% after 4500 hours of testing, whereas the device that has been kept at V_{OC} still shows a PCE of 1.0%. The experiment has been stopped after 4500 hours.

The findings are similar to earlier stability studies performed at TU Graz where the degradation of two identical roll-to-roll coated flexible polymer solar modules under light soaking has been tested, while one of them was kept at open circuit and the other at the maximum power point.[75] Although, devices showed differences in the dynamics of the decay, the overall the degradation of both devices was in the same range. As keeping the devices at their mpp during storage (active load) requires an expensive setup, the ISOS initiative suggests performing stability measurements at open circuit conditions or with the use of a passive load, while active load can be used in advanced testing techniques.

3.15 Influence of a lowered annealing temperature on the stability of hybrid solar cells with Ag-Al electrodes

In this experiment, the influence of a lowered annealing temperature, made possible with an n-hexylamine additive in the precursor solution, on the stability of PCDTBT-CIS solar cells hybrid solar cells is evaluated.[99] The devices have been prepared by Christopher Fradler. Both devices showed an initial PCE of ~2% prior to encapsulation.

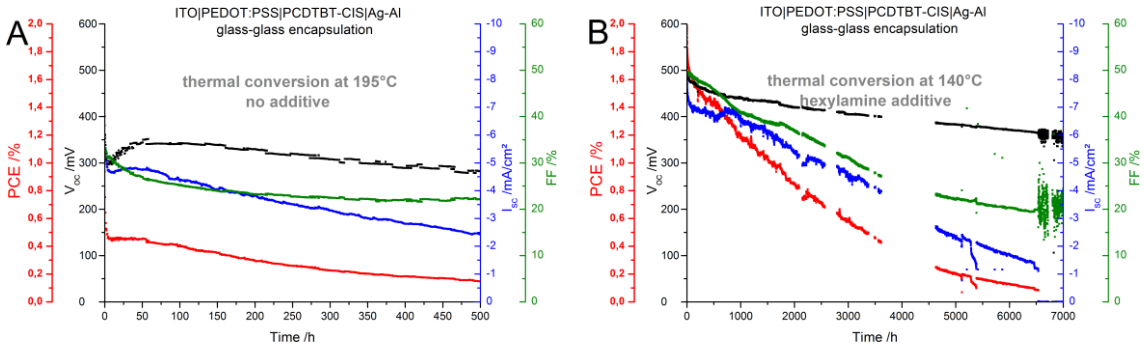

Figure 59: Lifetime tests of two glass-glass encapsulated PCDTBT-CIS hybrid solar cells with Ag-Al electrodes performed under continuous illumination using a solar simulator. The thermal conversion of the xanthates has been performed at 195°C without an additive (A) and at 140°C with an n-hexylamine additive (B).

The results of the stability study (Figure 59) show that the PCDTBT-CIS hybrid solar cell with Ag-Al electrodes that was annealed at 195°C already degraded to 0.94% during encapsulation followed by a heavy burn in phase which drops its PCE to ~0.45% within the very first hours (Figure 59A). In the following, the degradation slows, nevertheless after 500 hours the PCE is below 0.16%. In contrast, the solar cell that was prepared with the n-hexylamine additive and annealed at 140°C and is much more stable (Figure 59B). After a continuous illumination of 1000 hours the device still exhibits more than 60% of its initial PCE. After a burn in phase in the first 50 hours, the I_{SC} stayed quite constant during the first 1000 hours. From then on a steady loss in I_{SC}, FF and PCE can be observed, leading to PCE-values below 0.25% after 5000 hours of testing. For the V_{OC} only a slight decrease could be observed showing values around 530 mV after 1000 hours and 470 mV after 5000 hours.

3.16 A comparison of copper indium sulfide/polymer nanocomposite solar cells in inverted and regular device architecture

Sebastian Dunst, Thomas Rath, Angelika Reichmann, Huei-Ting Chien, Bettina Friedel, Gregor Trimmel

This chapter is submitted to Synthetic Metals.

3.16.1 Introduction

The conversion of light directly into electrical energy is one elegant solution to sustainably support covering the energy demand of the world, today and for future generations. Intense research works have brought interesting and quite diverse concepts into life how semiconductor materials and materials combinations are used to transform solar energy. In this context, nanocrystal/conjugated polymer hybrid solar cells – also called nanocomposite solar cells – are one of these new approaches, combining advantages of polymer based solar cells, e.g. use of roll-to-roll production processes, low processing temperatures, and thus the possibility to fabricate flexible and light weight solar cell foils, with those of inorganic nanocrystals, which have size-tunable optical and electronic properties.

Although this approach is somehow hidden by the success of polymer-fullerene[214] and, recently, perovskite solar cells,[27] continuous research work during the last years has augmented the understanding in synthesis, characterization and device assembly of hybrid solar cells, already summarized in various recent reviews (e.g. 55, 182, 183, 184, 185, 186, 187, 215, 216, 217). Upon the fast number of possible combinations of inorganic semiconductors and organic conjugated polymers, the most efficient solar cells have been obtained with PbS,Se nanoparticles exhibiting a power conversion efficiency of 5.5 %.[40] Examples for other promising systems are based on nanocrystals of CdS,[41,42] CdSe,[43,44,218] CdTe,[219,220] Sb_2S_3,[46] ZnO,[47] or $CuInS_2$ (CIS)[48,49] in combination with different conjugated polymers.

The to date obtained record efficiency is a very promising result considering the effect of the relatively low amount of work undertaken so far and that there are not many

materials systems with more than 10 papers published comparing for example to the several thousand articles on P3HT-PCBM solar cells.[221]

Regarding the synthesis of inorganic-organic hybrid solar cells, an *in situ* preparation route based on the thermal decomposition of metal xanthates directly in the matrix of the conjugated polymer has been introduced by us for the preparation of copper indium sulfide (CIS)-polymer solar cells and by S. A. Haque for CdS/polymer systems, see also Figure 60. This approach leads directly to a clean, ligand free nanocomposite layer, with PCEs reaching 2.2% for CdS[42] and 2.8% for CIS nanocrystals[49] in combination with P3HT and a low band gap polymer, respectively.

Because of the low conversion temperature, this versatile method can be applied for the preparation of nanocrystals in matrices of conjugated low band gap polymers[42,49] as well as small molecules,[222] for the preparation of tandem solar cells[98] and recently by lowering the conversion temperature to 160°C by adding a chemical additive, also for the preparation of flexible nanocomposite solar cells.[99] The formed copper indium sulfide nanoparticles have a size of 3-5 nm and form a well distributed network in the polymer matrix. Depending on the nanoparticle concentration in the polymer matrix, they also tend to agglomerate partly.[49,99,144,199]

Comparing the two main *in situ* prepared hybrid material combinations investigated up to now – CdS/polymer and $CuInS_2$/polymer – it is noticeable that in the CdS-system, solar cells were fabricated in the so called inverted architecture, whereas in the $CuInS_2$-systems only the regular architecture was applied. Both device architectures are also represented in the scheme in Figure 60. In the regular structure, the indium tin oxide electrode acts as anode whereas a low work function metal is used as cathode (e.g. Al, Ca/Al). Although usually also starting the device preparation from an ITO electrode, in the inverted architecture, cathode and anode are converse by the implementation of a hole blocking layer between the ITO and the active layer, such as e.g. TiO_x or ZnO, and an electron blocking layer such as PEDOT:PSS between the active layer and e.g. a silver electrode. Based on the experience from polymer-PCBM solar cells, the inverted solar cell architecture seems to be more robust and stable especially for encapsulated devices under permanent illumination[151] due to the possibility to avoid low work function electrodes. Nevertheless, using the regular architecture and silver electrodes, a remarkable long-term stability of several 1000 hours for glass-glass-encapsulated CIS/polymer solar cells has been observed.[223] Furthermore, the introduction of a thin Ti

or TiO_x layer between the active layer and the silver electrode significantly enhances the V_{OC}, showing also the importance of optimizing the metal contacts for this type of solar cells.

In this contribution, we combine the efficient solution processable solar absorber materials, copper indium sulfide nanoparticles[224] and the conjugated polymer PCDTBT[225,226] in hybrid solar cells and compare a regular device architecture with an inverted architecture regarding the performance of the solar cells. Additionally, we present first results on the stability of these solar cells. In both architectures, we use TiO_x as hole blocking layer, whereas the V_2O_5 and MoO_3 interlayers are compared to PEDOT:PSS as electron blocking layer. The widely used PEDOT:PSS hole transport layer has often been considered as a lifetime-limiting component due to its acidity and hygroscopic nature. In the regular architecture the uptake of water may lead to swelling of the interlayer and in succession to delamination of the device or may facilitate corrosion of the ITO electrode.[66] In the inverted architecture morphological changes in the adjacent Ag layer due to Ag_2S particle formation and migration has been observed, leading to a reduction of the Ag layer thickness and an electrode disconnection.[227] Metal oxides like V_2O_5,[110] MoO_3,[110] WO_3[228] or NiO_x[229] have been successfully introduced to displace PEDOT:PSS as hole transport layer in organic solar cells and an improved stability in air has been demonstrated.[212,226,230]

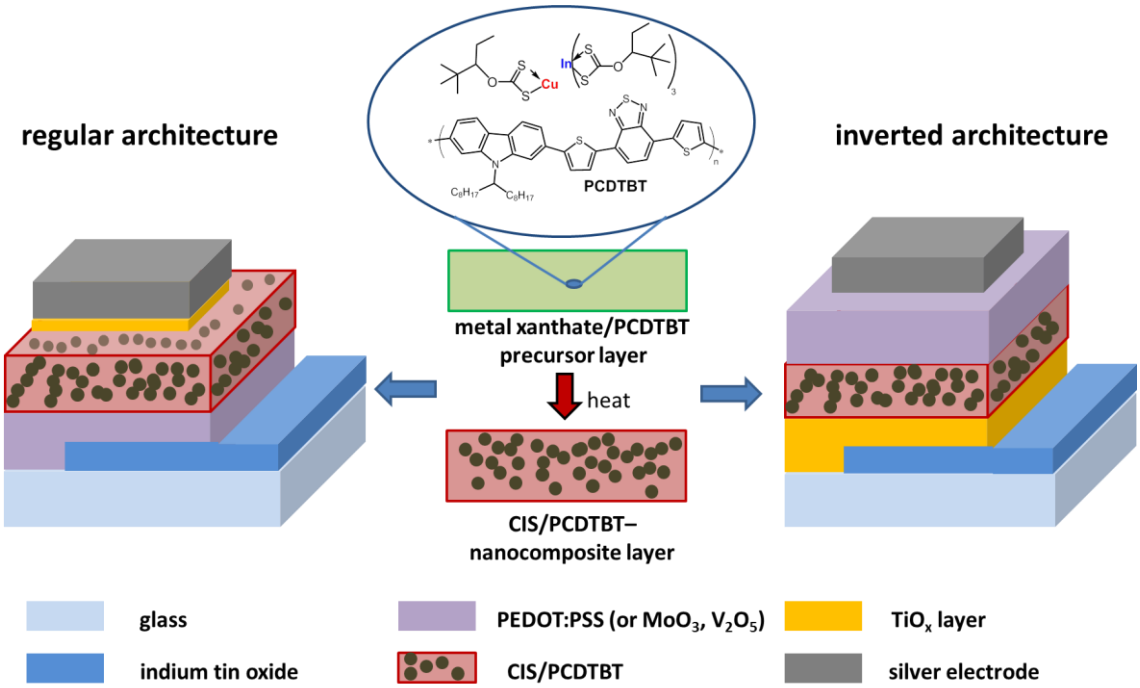

Figure 60: Schematic illustration of the regular and inverted device architectures and the *in situ* route using metal xanthates as precursors for the formation of metal sulfide nanocrystals directly in polymer matrices.

3.16.2 Experimental

Materials

Copper and indium xanthates (copper *O*-2,2-dimethylpentan-3-yl dithiocarbonate, indium *O*-2,2-dimethylpentan-3-yl dithiocarbonate) have been synthesized by Aglycon based on a published protocol[49] and recrystallized from chloroform/methanol. PCDTBT (poly[[9-(1-octylnonyl)-9H-carbazole-2,7-diyl]-2,5-thiophenediyl-2,1,3-benzothiadiazole-4,7-diyl-2,5-thiophenediyl]) was obtained from 1-Material, Chemsitech Inc., Canada. Titanium(IV)isopropoxide ($Ti(OiPr)_4$, 97%), ethanolamine (98%), 2-methoxyethanol (99.8%), vanadium(V)oxytriisopropoxide ($VO(OiPr)_3$) and MoO_3 (99.98% metal basis) were purchased from Sigma Aldrich and used without further purification. Two different formulations of PEDOT:PSS (poly(3,4-ethylenedioxythiophene)-poly(styrenesulfonate)), Clevios P VP.Al 4083 and Clevios HTL Solar, were obtained from Heraeus, Germany.

Elemental titanium (wire, 99.99%) and silver (wire, 99.99%) were obtained from ABCR. ITO-coated glass slides (10 Ω/sq) were obtained from Xinyan Technology Ltd., Hong Kong.

Solar cell preparation

ITO-coated glass slides were cleaned in isopropanol in an ultrasonic bath followed by O_2 plasma cleaning (FEMTO, Diener Electronic, Germany).

Regular architecture

Variation a: The PEDOT:PSS hole extraction layer (Clevios P VP.Al 4083, Heraeus) was spin coated (2500 rpm, 30 s) on the substrates and subsequently heated to 150°C for 10 min in a glove box (resulting layer thickness: 40 nm).

Variation b: The MoO_3 hole extraction layer (10 nm) was thermally evaporated at a rate of 0.1 Å/s – 0.5 Å/s under high vacuum ($5x10^{-6}$ - $1x10^{-5}$ mbar, residual gas: N_2)

Variation c: The V_2O_5 hole extraction layer was prepared by spin coating (3000 rpm, 30 s) 1.25 vol.% $VO(OiPr)_3$ in isopropanol on the substrates and hydrolyzed in air at room temperature for 1 hour.

For the preparation of the absorber layer, a precursor solution consisting of 5 mg/mL PCDTBT, copper xanthate (32.2 mg/mL, 1 equiv.) and indium xanthate (147.8 mg/mL, 1.7 equiv.) dissolved in chlorobenzene was deposited by doctor blading (speed: 7.5 mm/s, substrate temperature: 40°C). The thermal conversion was carried out on a hot plate at 195°C for 15 min (15 min heating time from room temperature to target temperature) under N_2 (resulting layer thickness: ~70 nm).

TiO_x interlayers (approx. 4 nm) were prepared via oxidative evaporation of titanium under medium vacuum conditions ($1x10^{-3}$ mbar, residual gas: air). Finally, the silver cathodes were deposited under high vacuum ($5x10^{-6}$ - $1x10^{-5}$ mbar, residual gas: N_2) via thermal evaporation through a shadow mask. The active area of the devices was 0.09 cm².

Inverted device architecture

For the preparation of the TiO_x films on the glass/ITO substrates, a precursor solution containing 70 µL titanium isopropoxide, 55 µl ethanolamine and 1 mL 2-methoxyethanol was used. The precursor solution was applied onto the cleaned and plasma treated ITO substrates by spin coating (4000 rpm). Subsequently, the substrates have been annealed for 1 h at 470°C in ambient conditions in a tube furnace.

The absorber layer was prepared as described in 2.2.1 with the only alteration that the speed during the doctor blading step was 10 mm/s. This slightly higher speed was necessary to obtain similar absorber layer thicknesses in the regular and inverted device

architectures due to different wetting properties of the precursor solution on the TiO_x and PEDOT:PSS films.

Optionally, additional layers have been introduced. For the preparation of CIS interlayers (between TiO_x and PCDTBT-CIS absorber layer) copper and indium xanthates were dissolved in chlorobenzene in the same ratio and concentration as for the absorber layer but without PCDTBT and doctor bladed (10 mm/s) at 40°C. The thermal conversion was done similarly to the PCDTBT-CIS absorber layer (resulting layer thickness: ~60 nm). For the preparation of the additional PCDTBT layer (between PCDTBT-CIS and the PEDOT:PSS or MoO_3 layers) a 1 mg/mL polymer solution in chlorobenzene was doctor bladed (10 mm/s) at 40°C.

Variation a: The PEDOT:PSS hole extraction layer (Clevios HTL Solar, Heraeus) was spin coated (2500 rpm, 30 s) on the absorber layer; no subsequent heating was applied.

Variation b: The MoO_3 hole extraction layer (10nm) was thermally evaporated at a rate of 0.1 Å/s – 0.5 Å/s under high vacuum ($5x10^{-6}$ - $1x10^{-5}$ mbar, residual gas: N_2)

Variation c: The V_2O_5 hole extraction layer was prepared by spin coating (3000 rpm, 30 s) 1.25 vol.% $VO(OiPr)_3$ in isopropanol on the absorber layer and hydrolyzed in air at room temperature for 1 hour.

Silver electrodes were deposited under high vacuum ($5x10^{-6}$ - $1x10^{-5}$ mbar, residual gas: N_2) via thermal evaporation through a shadow mask. The active area of the devices was 0.09 cm².

Characterization

Solar cell characterization

PCE values of prepared solar cells were determined from IV curves recorded inside a glovebox directly after preparation using a Keithley 2400 SourceMeter, a custom made LabVIEW software and a Dedolight DLH400D lamp. Irradiation intensity (100 mW/cm^2) was calibrated with a pyranometer (Kipp & Zonen).

The external quantum efficiency (EQE) was measured as a function of wavelength, using a monochromatic light source (250 W tungsten filament lamp, passed through a monochromator), with a final spot size smaller than the device active area. The short-circuit current was recorded with a Keithley 2636A source measure unit. Incident light

intensity was continuously monitored during measurement and referenced against a calibrated Si-photodiode (Thorlabs Inc., SM05PD1A-cal).

SEM

Cross-sectional SEM images were recorded on a Zeiss Ultra 55 scanning electron microscope, which was operated at 2 kV to prevent damage of the organic parts of the sample. The cross sections of the solar cells were prepared by large area ion milling using a Gatan Ilion^{+TM} followed by coating with a thin carbon film.

Lifetime tests

For the lifetime tests, the solar cells were encapsulated using a light curable epoxy resin (Ossila EE1) and an additional glass slide at the back of the solar cells. Stability data on encapsulated devices were collected under permanent illumination of 1000 W/m² using a solar simulator (Steuernagel KHS SC1200) according to ISOS-L-1 (level 1 laboratory testing).[72]

During the lifetime tests, IV curves were measured in periodic intervals of 30 min using an automated system. Between the measurements, the devices were kept in open circuit conditions. The used automated measuring system consisted of Keithley 2400 source meters, a Keithley 3706A multiplexer and custom made LabVIEW based software. Irradiation intensity was calibrated with a pyranometer (Kipp & Zonen) and monitored in intervals of 30 min using a Si-photodiode (Hamamatsu). The temperature of the solar cells was approx. 55°C during the stability tests.

3.16.3 Results and Discussion

Using an inverted device architecture, no low work function electrodes like aluminum or calcium are necessary, which improves the ambient stability of the solar cells and thus facilitates device processing and characterization.[23] These advantages have been extensively demonstrated for organic polymer/fullerene solar cells in recent years and also roll-to-roll processing of organic devices with respectable stabilities became viable due to the inverted device design.[71] This motivated us to investigate the influences of device design on *in situ* prepared polymer/CIS hybrid solar cells.

Initially, when the material system was introduced in 2011, aluminum electrodes were used as cathode material.[49] However, due to the limited lifetime of the solar cells a thin silver layer[97] or titanium-based interlayers[223] were introduced between absorber layer

and the Al cathode, or the aluminum electrode was replaced by Ag electrodes in combination with Ti or TiO_x interlayers to improve the open circuit voltage of the solar cells compared to bare Ag electrodes. The stability of the devices could be significantly improved using combined Ti/Ag or TiO_x/Ag electrodes, and promising lifetimes of approx. 4000 h with only 10% loss compared to the initial PCE values could be obtained. However, the open circuit voltage still remained significantly lower. Typical values of the V_{OC} of polymer/CIS hybrid solar cells having Ag electrodes with Ti-based interlayers range between 440 and 450 mV,[223] while using aluminum electrodes led to V_{OC} values up to 540 mV.[49]

First, we focused on the influence of different hole transport layers on the performance of solar cells in regular architecture. In Figure 61 typical IV curves of polymer/CIS solar cells prepared using TiO_x/Ag electrodes and PEDOT:PSS, MoO_3 or V_2O_5, respectively, as anode interlayers are presented. The highest V_{OC} in this series could be obtained with a PEDOT:PSS interlayer reaching 445 mV, the V_2O_5 interlayer yielded only slightly lower values of approx. 435 mV. MoO_3 as interlayer leads to V_{OC}s of only 395 mV. Also the highest photocurrents (8.6 mA/cm^2) and fill factors (55%) are obtained with PEDOT:PSS interlayers. The corresponding values for the other two investigated interlayers are lower, approx. 6.8 mA/cm^2 and 50%, respectively. This leads to PCE values of 2.1% for devices with PEDOT:PSS interlayer and to 1.5 or 1.4% for the solar cells with V_2O_5 or MoO_3 (see also Table 12 in the supplementary data in which the mean values and standard deviations of the best ten devices prepared in this study are summarized).

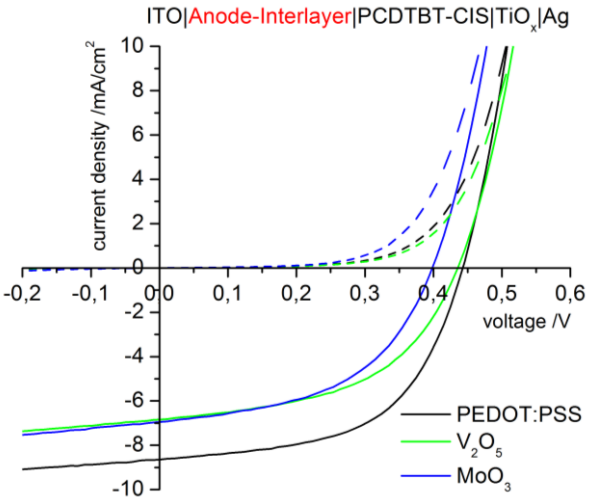

Figure 61: IV curves of typical PCDTBT-CIS hybrid solar cells in regular device architecture with PEDOT:PSS, V_2O_5 and MoO_3 as anode interlayers in the dark (dashed lines) and under 100 mW/cm² illumination (solid lines).

Next, we focused on the preparation of inverted solar cells using these different interlayers to study their performance in comparison to the solar cells in regular architecture. While the TiO_x interlayers are prepared by oxidative evaporation of titanium under medium vacuum conditions without any additional annealing in the discussed devices with regular architecture, the TiO_x interlayers in the inverted device design can be annealed at high temperatures.

In a first step, we applied a PEDOT:PSS interlayer between the absorber layer and the silver electrode to achieve the following inverted device: glass/ITO/TiO_x/PCDTBT-CIS/PEDOT:PSS/Ag. Figure 62 shows typical IV characteristics of these devices. When measured directly after the preparation, V_{OC} as well as I_{SC} of these devices are rather low (black curve in Figure 62). However, after several hours of light soaking (overnight; characteristic samples were selected and encapsulated between glass slides using UV-curable epoxy resin) under continuous AM1.5 illumination (100 mW/cm^2) both values increased significantly, an I_{SC} of slightly above 10 mA/cm^2 was obtained and the V_{OC} increased from 300 mV to 550 mV. The FF (36%) is lower in the inverted devices compared to the ones in regular geometry, which leads also to a PCE of 2.1%. This PCE is comparable to the devices with TiO_x/Ag electrodes prepared within this study in regular architecture.

Without having a low work function electrode in an inverted device architecture, the obtained V_{OC} value of 550 mV is even slightly higher than the V_{OC}-values (540 mV) of devices in regular architecture with aluminum electrodes.[49] Comparing the characteristic parameters of the solar cells prepared in inverted and regular geometry, it is apparent that the FF is significantly lower in the inverted architecture. This originates from a higher series resistance and lower shunt resistance of the device which might be because of the thicker TiO_x film (20 nm instead of 4 nm for the regular architecture) or a slight degradation of the conductivity of the ITO layer because of the annealing process. Interestingly, light soaking of the prepared inverted solar cells improves the V_{OC} and I_{SC} rather than the FF, as it is reported for inverted polymer/fullerene solar cells.[231,232] However, this might be related to the fact that the IV curves do not have a pronounced inflection point in the initial measurement before light soaking as commonly observed in polymer/fullerene solar cells.

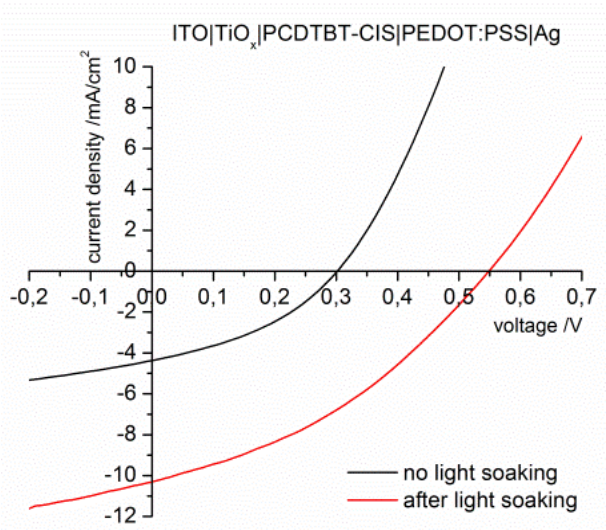

Figure 62: IV curves of PCDTBT-CIS hybrid solar cells in inverted device architecture using PEDOT:PSS as anode interlayer directly after the preparation and after several hours of light soaking.

When comparing the EQE spectra of devices with regular and inverted architecture (Figure 63), it is observed that the shape of the EQE spectrum looks slightly different, even though the same PCDTBT-CIS absorber layer is used in the devices. In the wavelength range from approx. 650 to 850 nm, the photocurrent is generated in the CIS phase, as the used polymer PCDTBT has a band gap of 1.9 eV[226] and a corresponding absorption onset slightly above 650 nm. At wavelengths lower than that, the photocurrent stems from both the polymer and the CIS phase and a peak around the absorption maximum of PCDTBT is observed in the EQE spectrum. Compared to the device with regular architecture, the more pronounced increase in the EQE spectrum of the inverted device around 450 nm is most likely due to optical effects in the device stack consisting of several thin films or a more pronounced contribution of the CIS phase to photocurrent generation in this wavelength range in the solar cell in inverted architecture. The absorption spectra of a PCDTBT, a CIS and a PCDTBT-CIS nanocomposite film can be found in the supplementary data (Figure 68).

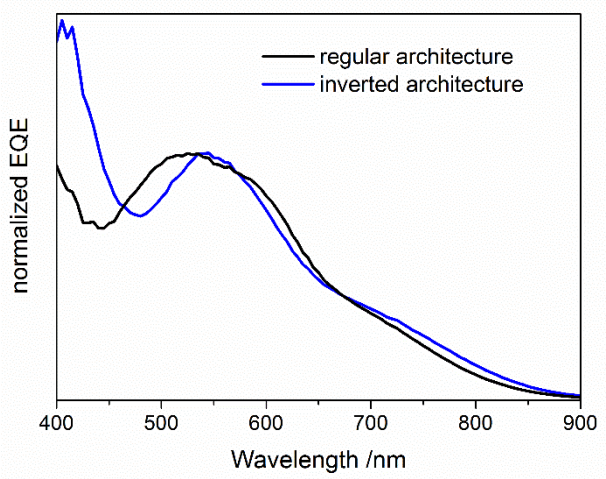

Figure 63: Comparison of the EQE spectra of a device with regular architecture (glass/ITO/PEDOT:PSS/PCDTBT-CIS/TiO_x/Ag) and one with inverted architecture (glass/ITO/TiO_x/PCDTBT-CIS/PEDOT:PSS/Ag).

By replacing PEDOT:PSS with V_2O_5 as hole extraction layer in the inverted architecture, it was not possible to prepare any working solar cells up to now. There are two possible reasons for that. First, the liquid precursor solution of $VO(OiPr)_3$ in isopropanol might diffuse into the underlying absorber layer and thus leads to short circuits in the devices. Second, the precursor has to be oxidized in ambient conditions for one hour, which could also induce oxidative degradation. However, due to the very low series resistance observed in these devices, the first reason is more likely to cause the problems to achieve diode characteristics in the inverted devices prepared with V_2O_5 interlayers.

Using MoO_3 as anode interlayer bears the advantage in the device fabrication that the absorber layer does not have to be brought in contact with an aqueous solution when coating of the PEDOT:PSS-layer or with isopropanol when applying the V_2O_5 layer, as MoO_3 is deposited by thermal evaporation. However, also devices in inverted architecture with MoO_3 hole extraction layers have been consistently short circuited. As no solvents are involved in the deposition of the MoO_3 interlayer, which could interfere with the hybrid absorber layer, we assume that this is likely to be due to MoO_3 or silver contacting ITO/TiO_x through the thin absorber layers of these devices which are only between 60 and 80 nm. The MoO_3 layers (10 nm) are much thinner as the PEDOT:PSS films (40 nm) and the thin MoO_3 films cannot even up possible inhomogeneities or pinholes in the absorber layers as for example a polymeric PEDOT:PSS film can.

Therefore, in a further step, we incorporated an additional CIS layer between the TiO_x layer and the polymer/CIS absorber layer to counteract short circuiting of the device. This concept is also applied in the closely related materials system P3HT/CdS prepared using the xanthate route, additionally observing an increase in V_{OC} by the incorporation of a CdS layer.[42]

The solar cells with an additional CIS layers exhibited diode characteristics and the achieved photocurrents are comparable to solar cells in regular architecture with MoO_3 interlayers. However, the fill factor and especially the V_{OC} with 229 mV are significantly reduced yielding to power conversion efficiencies of 0.4%. In a next step we additionally place a layer of pure PCDTBT between the nanocomposite layer and the MoO_3 layer resulting in the following sequence in the absorber layer: CIS – PCDTBT-CIS nanocomposite - PCDTBT. This stack leads to an increase in all solar cell parameters with a V_{OC} of 440 mV, an I_{SC} of 6 mA/cm^2 and a fill factor of 44% resulting in a PCE of almost 1.2% after light soaking. The results obtained for this series of inverted solar cells prepared with MoO_3 interlayer can be found in Figure 64 and Table 11.

In the case of the solar cells with CIS interlayer, the reason for the lower V_{OC} is mainly the poor stability of the device most likely due to partial short circuiting of the device (possibly due to direct contact of cathode and anode through pinholes in the absorber layer), which we think could be also the reason for the fact that we could not successfully realize diode characteristics with solar cells with MoO_3 interlayer without additional CIS or PCDTBT layer. In this solar cell, the V_{OC} decreased from 325 mV to 229 mV during light soaking, which we ascribe to an increased leakage current and a decreased shunt resistance in the device. In the solar cell with CIS and PCDTBT interlayer, the light soaking showed a positive effect on I_{SC}, V_{OC} as well as FF.

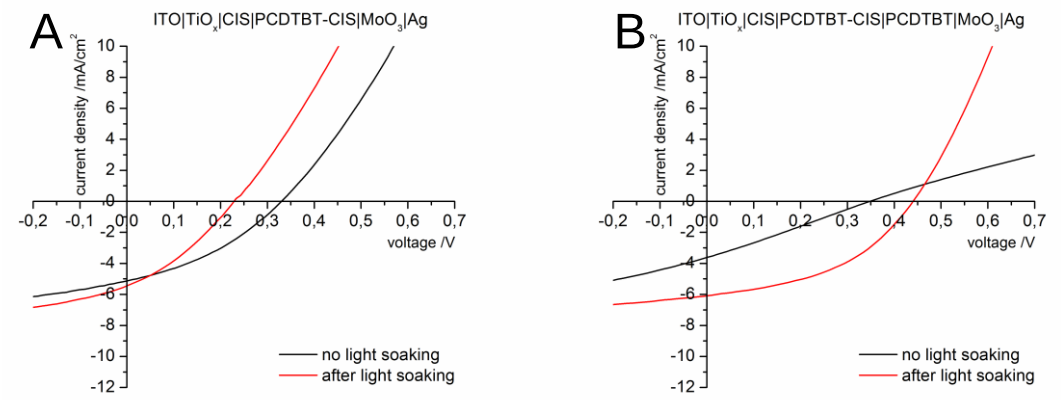

Figure 64: Characteristic IV curves of PCDTBT-CIS hybrid solar cells in inverted device architecture using MoO_3 as anode interlayer directly after the preparation and after several hours of light soaking. (A) glass/ITO/TiO_x/CIS/PCDTBT-CIS/MoO_3/Ag; (B) glass/ITO/TiO_x/CIS/PCDTBT-CIS/PCDTBT/MoO_3/Ag.

As the incorporation of an additional CIS and PCDTBT layer has increased the performance of the solar cells using MoO_3, we also introduced these layers in inverted devices with V_2O_5 and PEDOT:PSS as hole extraction layer. However, it was still not possible to obtain working solar cells with V_2O_5 interlayers. Thus, we think that the chosen solution based route for the preparation of the V_2O_5 interlayer is not ideal in the inverted architecture, while we obtained working devices in the regular device design. In the case of PEDOT:PSS as anode interlayer, functioning solar cells have been obtained.

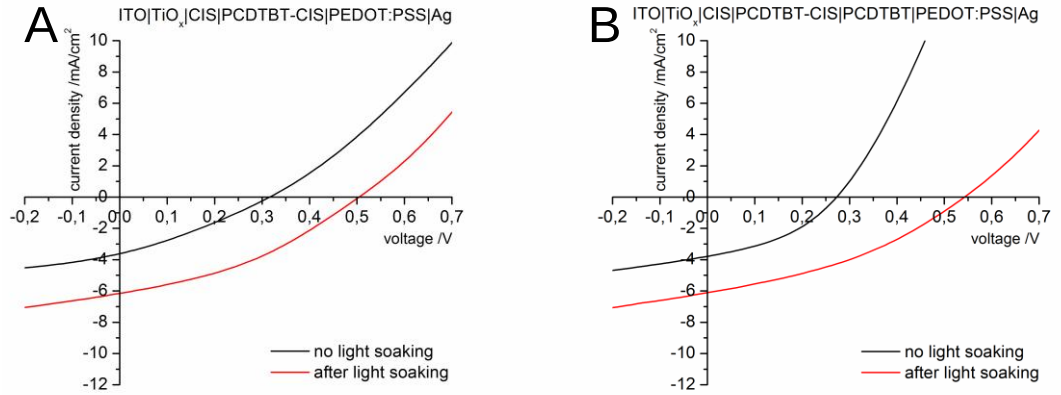

Figure 65: IV curves of inverted devices using PEDOT:PSS as anode interlayer. (A) glass/ITO/TiO_x/CIS/PCDTBT-CIS/PEDOT:PSS/Ag; (B) glass/ITO/TiO_x/CIS/PCDTBT-CIS/PCDTBT/PEDOT:PSS/Ag.

The IV curves represented in Figure 65 show that the introduction of additional interlayers lead to a reduction of the solar cell performance, especially the I_{SC} exhibits

only values of approx. 6 mA/cm^2, similar to the devices with MoO_3 interlayer. The V_{OC} of the device with both additional layers (CIS and PCDTBT) has a value of 540 mV (see Figure 65B) similar to the device without these two additional layers. Having only the additional CIS layer, the V_{OC} was found to be approx. 500 mV. The corresponding characteristic parameters of the solar cells are summarized in Table 11.

Table 11: Characteristic solar cell parameters of PCDTBT/CIS hybrid solar cells prepared in regular (reg.) and inverted (inv.) device architecture with different interlayers.

	Interlayers	V_{OC} / mV	I_{SC} / mA/cm²	FF / %	PCE / %	R_s / Ω*cm²	R_{sh} / Ω*cm²
	PEDOT:PSS	445	8.64	55.5	2.13	9.8	464
reg.	MoO_3	395	6.94	50.3	1.38	12.3	471
	V_2O_5	435	6.83	50.8	1.50	12.3	555
	PEDOT:PSS	549	10.3	36.3	2.08	27.9	141
inv.	CIS* / PEDOT:PSS	507	6.19	36.6	1.17	45.4	200
	CIS* / PCDTBT** / PEDOT:PSS	543	6.11	36.4	1.25	45.0	190
	MoO_3	-	-	-	-	-	-
inv.	CIS* / MoO_3	229	5.45	32.6	0.41	24.9	80
	CIS* / PCDTBT** / MoO_3	440	6.09	43.8	1.18	23.9	289

*** CIS layer is introduced between TiO_x and the absorber layer**

**** PCDTBT layer is introduced between the absorber layer and the PEDOT:PSS or MoO_3 interlayer**

In the case of MoO_3 interlayers, these two additional layers are absolutely necessary to circumvent short-circuiting. However, in the case of the devices with PEDOT:PSS interlayer, these two additional layers lead to a significant reduction of the photocurrent stemming from the limited mobility in the nanocrystalline CIS and PCDTBT in the thicker device stack, which results in a higher series resistance in the solar cells.

Due to the significant differences in performance and stability of the inverted devices using PEDOT:PSS or MoO_3 interlayers, we also investigated the device structure and the thicknesses and homogeneities of the individual layers in the device stack using SEM.

Therefore, we selected an inverted device with a PEDOT:PSS interlayer, and one with a MoO_3 interlayer and an additional CIS layer between TiO_x and absorber layer.

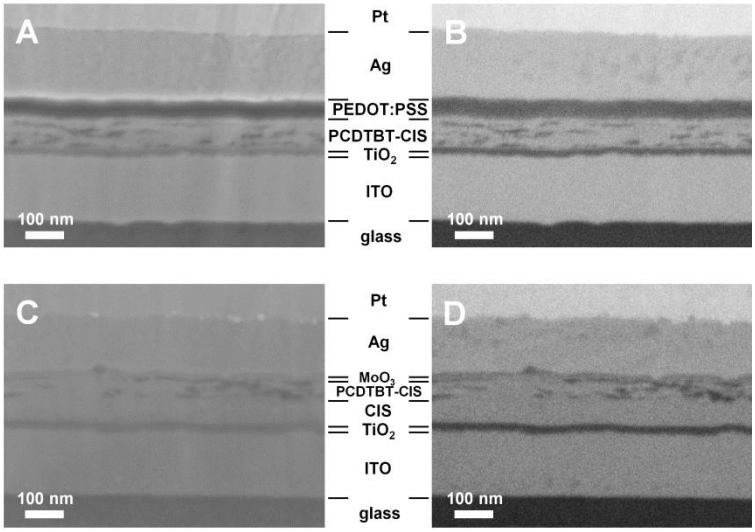

Figure 66: Cross-sectional SEM images of PCDTBT/CIS hybrid solar cells in inverted architectures (A, B: glass/ITO/TiO_x/PCDTBT-CIS/PEDOT:PSS/Ag and C, D: glass/ITO/TiO_x/CIS/PCDTBT-CIS/MoO_3/Ag). Images A and C were acquired using an in lens secondary electron detector while images B and D were recorded using a back-scattered electron detector.

The SEM images of the cross sections of the respective devices depicted in Figure 66 show that the layers are smooth and the thicknesses of the different layers are homogenous. Images A and C are recorded using an in lens secondary electron detector and for images B and D a back-scattered electron detector was used to achieve better element contrast. It can be noticed in the SEM images of both solar cells that the PCDTBT-CIS absorber layer consists of brighter and darker areas. The brighter areas represent the well mixed polymer/CIS nanocrystal nanocomposite, while the darker areas are polymer aggregates with very low concentration of or free from CIS nanocrystals.[144]

In the solar cell with the PEDOT:PSS interlayer, the ITO layer is 170 nm thick, the TiO_x film is about 15-20 nm. The PCDTBT/CIS absorber layer has a thickness of 70 nm followed by a 40 nm thick PEDOT:PSS film and the Ag electrode (170 nm). In the solar

cell with the MoO_3 interlayer and an additional CIS layer the following thicknesses are found: ITO (170 nm), TiO_x (15-20 nm), CIS (60 nm), PCDTBT-CIS (60 nm), MoO_3 (10 nm), Ag (140 nm). The Pt film was coated on the solar cells prior to ion milling to protect the device. The images also reveal that the MoO_3 interlayer is thinner than 10 nm in some areas of the sample (see left part of Figure 66D), while the PEDOT:PSS film has a constant thickness of 40 nm over the investigated sample area (Figure 66B), which is supporting our assumption of PEDOT:PSS being more effective than MoO_3 in preventing direct contact of Ag with the absorber layer or the cathode in the case of possible pinholes in the absorber layer. Using a thicker MoO_3 interlayer might also prevent direct contact of silver to the absorber layer or the other electrode, however, device performance would be lowered by the thicker MoO_3 interlayer.[228]

The open circuit voltages (up to 550 mV) obtained in the inverted PCDTBT/CS hybrid solar cells with PEDOT:PSS interlayer and sliver electrode are the highest obtained so far for this material system and it should be emphasized that this could be obtained without using a low work function electrode (e.g. aluminum). Therefore, we also started testing the lifetime of the devices with PEDOT:PSS interlayers. The changes of V_{OC}, I_{SC}, FF and PCE of the devices over time are summarized in Figure 67. The solar cell without additional CIS interlayer (Figure 67A) shows stable behavior for 45 h of continuous illumination, before the V_{OC} of the device suddenly decreased from 550 mV to 45 mV, most likely due to short circuiting of the device due to diffusion/migration of silver, which was also already observed before for a polymer/CIS hybrid solar cells with silver electrodes in regular device geometry.[223] A further lifetime test of a device with the same architecture revealed a very similar behavior. The V_{OC} also suddenly decreased after approx. 65 h of illumination (see Figure 69 in the supplementary data).

The introduction of an additional CIS layer into the device stack seems to prevent this behavior and thus the solar cell with CIS layer shows relatively stable values for I_{SC} and FF after a short burn in phase of about 20 h and only a moderate decline for V_{OC} leading to a PCE reduction from 1.16% to 0.80% after 2500 h of continuous illumination (see Figure 67B). The minor irregularities in the I_{SC} during the lifetime test (from 180 h onwards) stem from changes in illumination intensity caused by the lamp in this phase of the test.

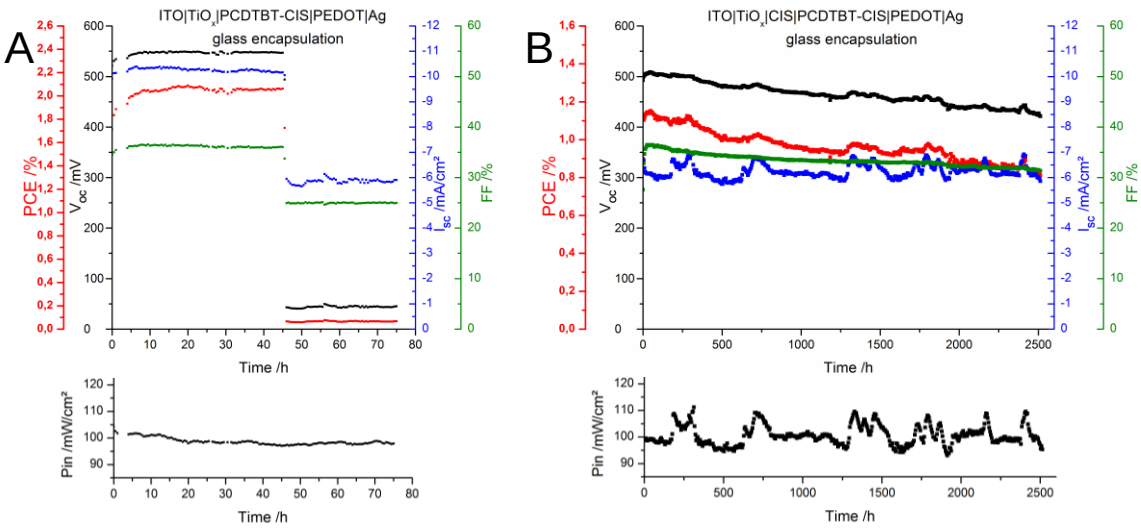

Figure 67: Characteristic parameters (V_{OC}, I_{SC}, FF, PCE) over time of a glass/glass encapsulated inverted PCDTBT/CIS hybrid solar cell with different device architectures performed under continuous illumination using a solar simulator (P_{in} in mW/cm^2 over time is also shown in the graph). (A) glass/ITO/TiO$_x$/PCDTBT-CIS/PEDOT:PSS/Ag; (B) glass/ITO/TiO$_x$/CIS/PCDTBT-CIS/PEDOT:PSS/Ag.

3.16.4 Summary

By preparing PCDTBT/CIS hybrid solar cells in inverted device architecture, open circuit voltages up to 550 mV could be obtained. Using this hybrid nanomaterials combination this was so far only possible using low work function metal electrodes like aluminum. Using the inverted device design, the low work function metal electrode could be replaced by silver electrodes in combination with a PEDOT:PSS interlayer, without losses in open circuit voltage and short circuit current. In the solar cells prepared in the regular design, the V_{OC}s were limited to lower values (up to 445 mV). However, in the inverted devices, the fill factor is lower compared to solar cells in regular geometry, which is limiting the PCE of the inverted solar cells to 2.1% up to now. Working with MoO_3 as interlayer leads to similar photocurrents compared to solar cells with PEDOT:PSS interlayer, however, the photovoltages are significantly lower.

Solar cells in inverted architecture having a PEDOT:PSS interlayer and an additional CIS layer show good stability and maintain their high open circuit voltage over hundreds of hours of continuous illumination. Due to the shorter lifetime of the device without CIS layer, we suspect that diffusion of silver through the absorber layer leading to short circuiting of the device is a crucial factor limiting the solar cell lifetime. In

further research, we will closely study this issue and will elaborate strategies to modify the silver electrode (with e.g. a Ti interlayer) or to completely replace it to further improve long-term device stability of this type of solar cells.

3.16.5 Supplementary data for: A comparison of copper copper indium sulfide/polymer nanocomposite solar cells in inverted and regular device architecture

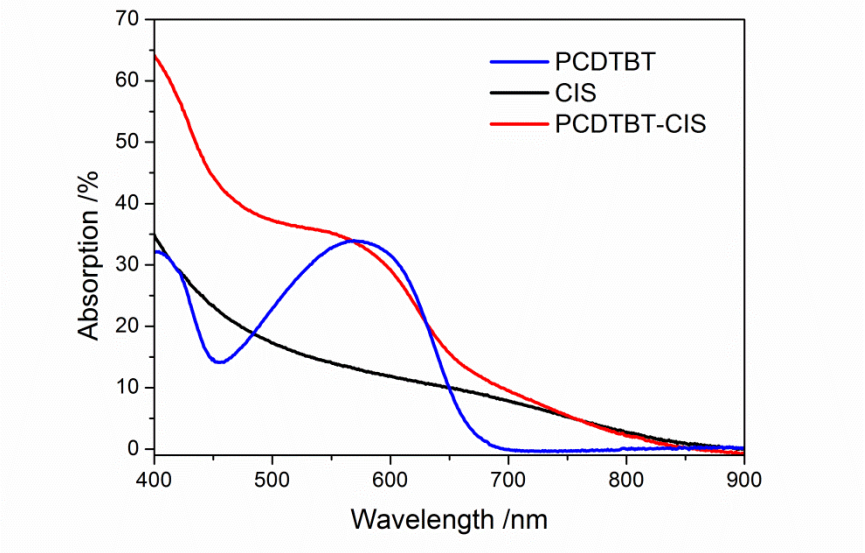

Figure 68: UV-VIS absorption data of PCDTBT, CIS and the PCDTBT-CIS nanocomposite.

Table 12: Mean values and standard deviations of solar cells prepared with regular device architecture (best 10 of each configuration) prepared in this study.

	Interlayers	V_{OC} /mV	I_{SC} /mA/cm²	FF /%	PCE /%
	PEDOT:PSS	449 ± 0	8.30 ± 0.28	55.3 ± 0.6	2.06 ± 0.05
reg.	MoO_3	386 ± 0	6.77 ± 0.50	51.0 ± 1.1	1.31 ± 0.04
	V_2O_5	433 ± 0	6.53 ± 0.22	50.1 ± 0.9	1.43 ± 0.05

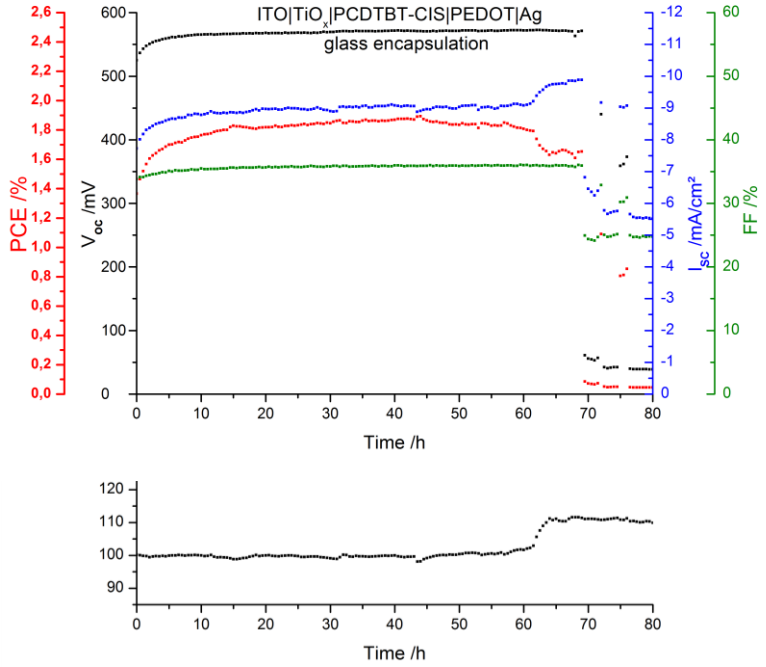

Figure 69: Lifetime test of a solar cell prepared in the inverted architecture glass/ITO/TiO_x/PCDTBT-CIS/PEDOT:PSS/Ag. The degradation behaviour matches the one of a similarly prepared device presented in Figure 67.

3.17 Nanoimprinted comb structures in a low bandgap polymer: thermal processing and their application in hybrid solar cells

Sebastian Dunst, Thomas Rath, Andrea Radivo, Enrico Sovernigo, Massimo Tormen, Heinz Amenitsch, Benedetta Marmiroli, Barbara Sartori, Angelika Reichmann, Astrid-Caroline Knall, Gregor Trimmel

This chapter was first published in ACS Applied materials & interfaces 6, 10 (2014) 7633 – 7642.

Reproduced by permission of the American Chemical Society.

3.17.1 Introduction

Inorganic-organic hybrid solar cells consisting of a mixture of an inorganic nanostructured semiconductor and an organic semiconductor have been researched since more than 15 years. In particular, in the last 5 years major progress has been achieved by pursuing different strategies[182,185,216] and power conversion efficiencies have now reached 4 – 5.5%.[40,43,45]

The key parameters for obtaining efficient solar cells and the starting points for further improvements are similar to those of polymer-fullerene solar cells: (1) the adjustment of the electronic and optical properties of the donor (usually the organic semiconductor) and the acceptor (inorganic semiconductor), (2) the optimization of the morphology between donor and acceptor and (3) the optimum extraction of the carriers by adjusted electrodes.

Especially the second point, the optimum phase separation and the understanding of its importance to the power conversion efficiencies (PCEs) has tremendously improved the efficiencies of polymer-PCBM ([6,6]-phenyl C_{61} butyric acid methyl ester) solar cells. The optimum phase separation between donor and acceptor is a compromise between a large interface for efficient charge separation (necessary for exciton dissociation in the polymer phase) and continuous (and larger) domains for fast charge transport. There is a plenitude of studies focusing on the issue of how to optimize this nanomorphology (for reviews see references 233, 234, 235 and 236).

In the context of organic/inorganic hybrid solar cells, inorganic nanostructures of non-spherical shape (nanorods, tetrapods, clusters) are of interest since these could facilitate charge transport while keeping a large interface.[237] However, a simple mixing of donor and acceptor might lead to isolated nanoparticles in the polymer matrix, which cannot contribute to electricity generation as electrons will not find a path to the electrodes. In addition to these issues, the surface of the nanoparticles and in turn also the interface between nanoparticle and polymer phase make this field more complicated.[238] Capping ligands are isolating, while uncapped nanoparticles may have defects which may act as trap sites.

So far, mainly three methods for the fabrication of hybrid solar cells have been developed.[55] In the classical approach the nanoparticles are prepared via colloidal synthesis routes, are then subjected to a purification or ligand exchange process in a second step and are finally mixed with a conjugated polymer to form the active layer of the hybrid solar cell. In this approach, a solution of the nanoparticles and polymers is coated onto the electrodes during device fabrication. The ligand-free *in situ* approach, in which the nanoparticles are directly prepared from precursor materials in the polymer matrix, intends to overcome the problems of ligand exchange and is an interesting alternative route to the classical colloidal approach.[55,186] Following this route, a solution of a nanoparticle-precursor and the conjugated polymer is used for device fabrication. In both methods the possibilities to control the absorber layer morphology are limited. In the classical approach different morphologies can be obtained by changing the shape of the nanoparticles (dots, rods, tetrapods), in the *in situ* route changing the shape of the nanostructure is more challenging, however, also nanorod-type structures have been already obtained with this method.[202]

The third approach, the „infiltration approach“ provides the possibility to obtain highly ordered absorber layers without ligands between the inorganic and organic phase. Here, in a first step, inorganic nanostructured layers are prepared using different techniques like (template assisted) nanorod or nanotube growth,[239,240] UV-lithography,[241] etching,[242,243] or selected area epitaxy processes[244] and are then infiltrated with an organic conjugated polymer to complete the active layer of the solar cell.[245]

Alternatively, the polymeric semiconductor can be nanostructured with techniques like nanoimprint lithography (NIL). The resulting polymer nanostructures are in turn infiltrated with the inorganic component, similar to how it is done for polymer/PCBM

solar cells.[234,246,247,248] This approach, including NIL-structuring, has, regarding possible future large scale production of organic or hybrid solar cells, the advantage that, roll-to-roll structuring and processing can be realized.[234] However, in this case the soft organic material is situated at the bottom of the absorber layer and the hard inorganic material at the top, which is challenging for the processing procedure.

In this study, we explore the preparation of nanostructured polymer/metal sulfide hybrid solar cells by using thermal decomposition of metal xanthates for the formation of the metal sulfide phase on a NIL-structured polymer layer. Metal xanthates have recently been used for the ligand-free fabrication of bulk heterojunction polymer/metal sulfide nanoparticle hybrid solar cells[42,46,49,199,222] and can be also used for this approach because of their ability to be converted into the metal sulfide without byproducts remaining in the metal sulfide layer already at comparably low temperatures.[49] Regarding the thermal management, it would be more convenient to structure the metal xanthate layer first, but due to the crystallinity and the low thermal stability of the metal xanthates, this is not possible.

3.17.2 Experimental

Sample Preparation

Poly[(2,7-silafluorene)-alt-(4,7-di-2-thienyl-2,1,3-benzothiadiazole)] (PSiF-DBT) films deposited either on silicon for the GISAXS study or on glass/ITO/PEDOT:PSS for the solar cell study were patterned by thermal nanoimprint lithography (NIL).[249]

For the GISAXS study, the PSiF-DBT films on silicon were imprinted using a PW 20 E press (Paul-Otto Weber GmbH) at 125°C and 6 MPa in ambient atmosphere. To prevent potential deterioration of the electronic properties of the conjugated polymer by oxidative degradation, for the hybrid solar cells the PSiF-DBT films were imprinted in a glove box filled with nitrogen at 5 MPa and 150°C using a homemade thermal NIL press. As NIL stamps, silicon gratings with periodicities of 180, or 500 nm or their copies on glass/Ormostamp (microresist technologies GmbH) were used after functionalization of their surfaces with a monolayer of octadecyl trichlorosilane assembled from vapor phase as antiadhesion agent. Ormostamp replica of the silicon masters were prepared by UV-NIL structuring of an Ormostamp resist on glass substrates.[250,251]

Describing the NIL-structuring process briefly, stamp and sample are put face-to-face onto the plate of the press, the heating ramp is started and after reaching the pre-set imprinting temperature, pressure is applied and maintained for 5 minutes. Subsequently, the hot plates are cooled down to 40°C, the pressure is released and the stamp and sample are manually separated.

The hybrid solar cells were fabricated on glass/ITO substrates (Xinyan Technology Ltd., Hong Kong) with a sheet resistance of 10 Ω/sq, which were cleaned in deionised water and isopropanol in an ultrasonic bath followed by O_2 plasma cleaning (FEMTO, Diener Electronic, Germany). The PEDOT:PSS layer (Clevios P VP.Al 4083, Heraeus) was spin coated on the glass/ITO layer and subsequently annealed at 150°C for 10 min in a glove box. As a second layer PSiF-DBT (1-Material, Chemsitech Inc., Canada) was coated by doctor blading on the PEDOT:PSS layer from a chloroform solution (10 mg/mL), which was partly nanostructured by NIL (as described above) in a further step.

The precursor layer for the copper indium sulfide (CIS) layer, consisting of a copper and indium xanthate mixture (12.1 mg/mL, 1 equiv. copper *O*-2,2-dimethylpentan-3-yl dithiocarbonate; 54.6 mg/mL, 1.6 equiv. (for annealing at 160°C) or 55.4 mg/mL, 1.7 equiv. (for annealing at 195°C) indium *O*-2,2-dimethylpentan-3-yl dithiocarbonate; metal xanthates were obtained from Aglycon, Austria) dissolved in the solvent mixture isopropanol:dichloromethane:pyridine = 4:2:1 (vol:vol:vol) was deposited by doctor blading. The coating step was followed by a thermal conversion step at a temperature of 160 or 195°C on a programmable heating plate (CAT Ingenieurbüro M. Zipperer GmbH, Germany; temperature program: heating with a rate of 11°C/min to a temperature of 160°C or 195°C and a holding time at this temperature for 30 min (160°C) and 15 min (195°C), respectively). The synthesis of the xanthate precursors and the thermal conversion step in order to obtain CIS nanoparticles has been described previously.[49] The about 200 nm thick aluminum electrodes were deposited via thermal evaporation.

Characterization

SEM images of the NIL-structured polymer layers were acquired on a Zeiss Supra 40 scanning electron microscope, analyses of cross sections of the prepared solar cells were conducted on a Zeiss Ultra 55 electron microscope; the cross sections for these

characterizations were realized by large area ion milling using a Gatan Ilion^{+TM}. Layer thicknesses were determined on a Bruker DekTak XT surface profiler.

2D grazing incident small angle X-ray scattering (GISAXS) measurements were performed at the Austrian SAXS Beamline 5.2L of the electron storage ring ELETTRA (Italy),[252] using a similar setup as described before.[253] The beamline has been adjusted to a q-resolution ($q=4\pi/\lambda*\sin(2\Theta/2)$, 2Θ represents the scattering angle) between 0.1 and 3.1 nm^{-1} (GISAXS). The X-ray energy was 8 keV. The nanostructured samples were placed in a modified heating cell (DHS 1100 from Anton Paar GmbH, Graz, Austria) with custom-made dome with a grazing angle of about 0.18° and were heated from 35°C up to 200°C at a heating rate of approx. 10°C min^{-1} under nitrogen atmosphere. The NIL-imprinted line structures were aligned parallel to the X-ray beam. During the temperature scan, data were recorded with 11 s time resolution using an image intensified CCD detector (GemStar/XIDIS model, Photonic Science Ltd., Millham / UK). For detection of the GIWAXS signal, a two-dimensional hybrid pixel array detector system (Pilatus 100K, Dectris) was used. The angular calibration of the detectors was carried out using silver behenate powder (d-spacing of 58.38 Å).

PCE values of the solar cells were determined from IV curves recorded using a Keithley 2400 SourceMeter, a custom made Lab-View software and a Dedolight DLH400D lamp. The light intensity was set to 100 mW/cm^2 providing a spectrum quite similar to AM1.5G (determined using a KippZonen-CMP-11 pyranometer, no spectral mismatch was considered).

3.17.3 Results and discussion

Figure 70 schematically depicts the process steps for the fabrication of nanostructured polymer/metal sulfide absorber layers for hybrid solar cells using NIL for structuring of the polymer and metal xanthates as precursors for the metal sulfide. Firstly, a comb structure is imprinted in the conjugated polymer PSiF-DBT. Secondly, the structured layer is coated with a metal xanthate solution and finally, the metal xanthates are thermally converted to a metal sulfide layer. During this preparation process, besides the NIL-structuring, the stability of the nanostructures against solvents used for coating the metal xanthates as well as the thermal stability of the nanostructures during the

thermal conversion of the metal xanthates to the sulfides are critical issues, which are investigated in this work.

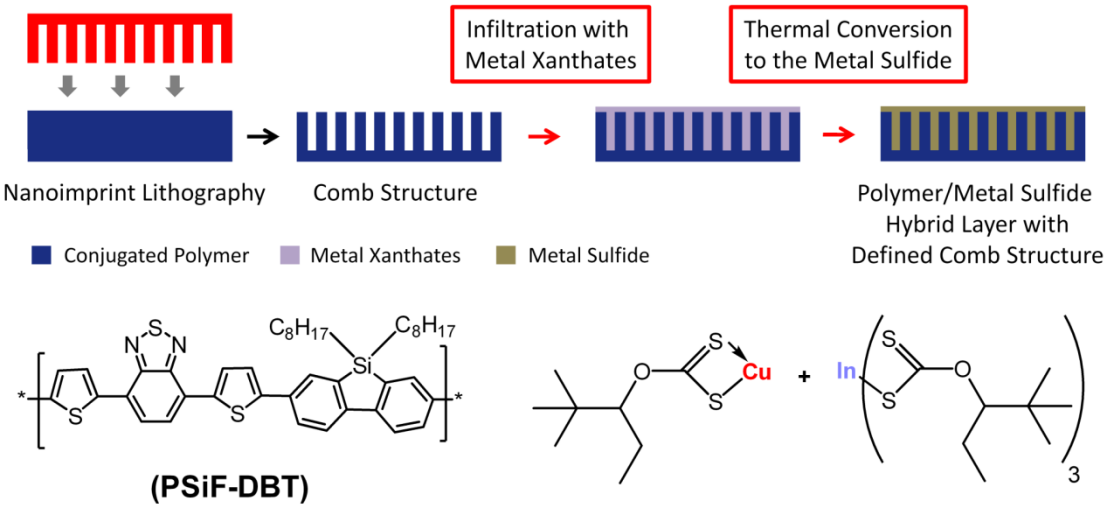

Figure 70: Schematic illustration of the NIL-process for the preparation of comb structures and the infiltration process towards defined hybrid layers and chemical structures of the used polymer PSiF-DBT and the Cu- and In-xanthates.

For the NIL-structuring of the low bandgap polymer PSiF-DBT (poly[(2,7-silafluorene)-alt-(4,7-di-2-thienyl-2,1,3-benzothiadiazole)], the chemical structure is given in Figure 70), we started with the optimized standard parameters for thermal nanoimprint lithography (NIL) used for structuring of poly (3-hexylthiophene) P3HT, i.e. 100°C and 6 MPa.

From these starting values, we found that for PSiF-DBT the temperature had to be increased to or above 125°C to accurately reproduce gratings of 500 and 180 nm periodicity. The actual samples used in the GISAXS study were made in ambient atmosphere and consisted of PSiF-DBT film on silicon imprinted at 13 MPa and 125°C. The samples used for the fabrication and the study of photovoltaic cells were made on ITO coated glass substrates, and the PSiF-DBT film was imprinted at 5 MPa and 150°C in a glove box with nitrogen atmosphere, owing to reduced concerns about polymer degradation and better imprinting results.

For optimizing the processing parameters and preliminary thermal stability studies, defined comb structures with a periodicity of 500 nm were imprinted in the PSiF-DBT layer. A SEM image of such a layer is shown in Figure 71A. The height of the

structures is approx. 260 – 270 nm (see Figure 79 in the supporting information). For further studies and fabrication of solar cells, comb structures with a periodicity of 180 nm were prepared.

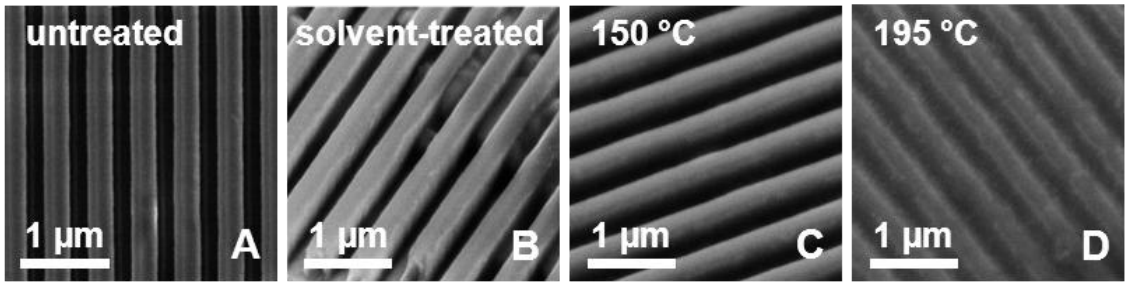

Figure 71: SEM images of NIL-imprinted comb structures (periodicity 500 nm); (A) after the NIL step, (B) after NIL and solvent treatment, and (C, D) after NIL and subsequent temperature treatment at 150°C or 195°C.

After the NIL-structuring process, for the realization of nanostructured hybrid solar cells via the "xanthate route", it was important to find a suitable solvent for applying the metal xanthate layer on the nanostructured polymer layer, which provides sufficient wettability, but does not harm or even erase the imprinted nanostructures. Therefore, in a first step, experiments were conducted to find proper solvents for this process step by immersing non-structured flat polymer layers on glass substrates in a series of different solvents and solvent combinations, which have the capability of readily dissolving the copper as well as the indium xanthate. Among the tested solvents (chloroform, dichloromethane, toluene, chlorobenzene, DMF, aceton, THF, isopropanol) a mixture of isopropanol, dichloromethane and pyridine (4:2:1 vol:vol:vol) turned out to be the most promising one, as it did not dissolve the polymer layer at all even after immersion for more than 24 hours. Additionally, we also evaluated the stability of the nanostructured layer against this solvent combination by immersing the layer for one minute, which is about the time for which the nanostructured sample is actually in contact with the solvent during the doctor blading step in the course of solar cell fabrication. The SEM image in Figure 71B proves that the nanostructured layer withstands the solvent treatment and the defined rectangular shape of the comb structure is retained. The partial filling of the nanostructures (visible in the upper right part of the image) can be assigned to undefined drying of the layer after solvent treatment and will not have an influence on the nanostructured polymer/CIS heterojunction.

A further crucial issue to realize hybrid solar cells following this route is a sufficient thermal stability of the nanostructures in the conjugated polymer layer, as the metal xanthates have to be thermally converted to yield the metal sulfide. Thus, we characterized the influence of thermal treatment of the structured polymer layers by means of SEM and time resolved GISAXS. Comparing the SEM micrographs of a pristine NIL-structured polymer layer (Figure 71A) with those of layers after heat treatment for 15 min at 150°C (Figure 71C) and 195°C (Figure 71D), it is clearly visible that the untreated sample has line structures with comparably sharp edges, which appear softer in the sample annealed at 150°C and which became quite blurred in the sample heated to 195°C. This rough analysis suggests that the line structures are still present after a temperature treatment of 150°C, which is sufficient for the formation process of the copper indium sulfide layer without destroying the polymer nanostructures. However, also a remaining of the structural motif is still clearly visible after heating to 195°C.

For the time resolved GISAXS study on the thermal stability of the imprinted line structures, a nanostructured layer was heated in a measuring cell (under nitrogen atmosphere) directly in the X-ray beam. For these measurements, nanostructured layers with a periodicity of 180 nm were used as it was intended to apply layers with this periodicity in hybrid solar cells. Thus, these results are not directly comparable with the SEM measurements presented in Figure 71. The GISAXS patterns of a nanostructured PSiF-DBT film on a silicon substrate at different temperatures (65, 105, 143 and 200°C) during the heating run to 200°C (heating rate: 10°C/min) are shown in Figure 72.

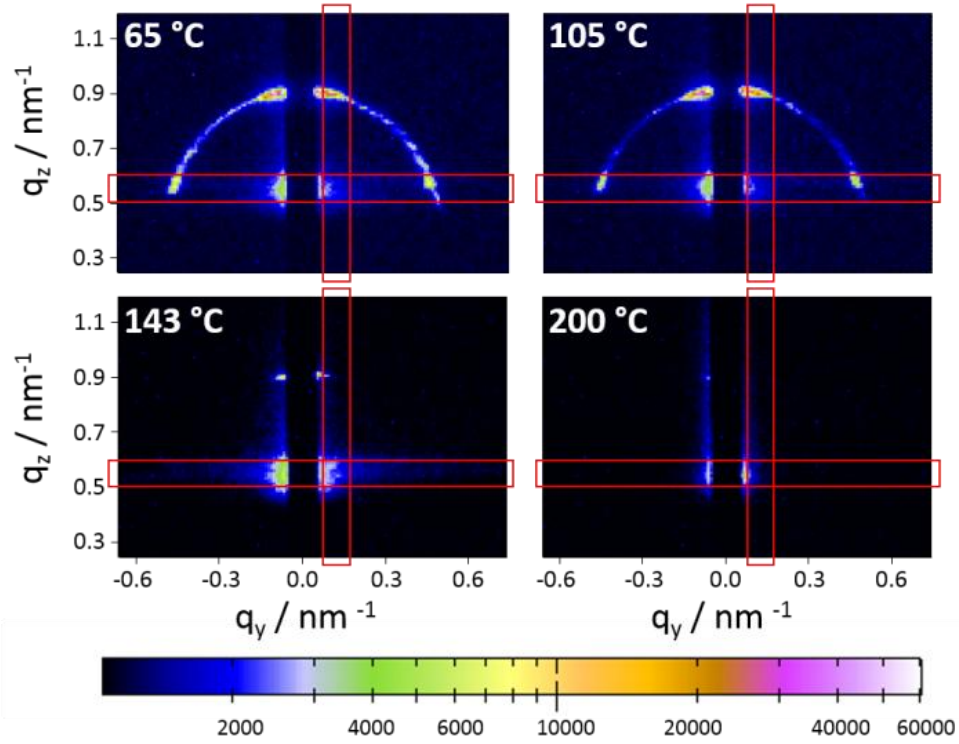

Figure 72: GISAXS images of a NIL-structured PSiF-DBT film (periodicity: 180 nm) at 65, 105, 143 and 200°C. The red boxes indicate the vertical and horizontal areas for integration.

At temperatures lower than 120°C, a semicircle like chain of intensity maxima is visible, which is typical for periodic line structures oriented parallel to the X-ray beam.[254,255] The maximum in the out-of-plane position is given by the intersection of the truncation rods inclined with the grazing angle and the Ewald spheres. The inclination angle was 0.63° in this case. Similar patterns have been observed for NIL-structured polymer layers.[256] Further, the thermal stability has also been investigated for 4 µm NIL structures by the group of Müller-Buschbaum.[257] By further increasing the temperature, this semicircle like pattern vanishes and only a feature near to the beam stop, which represents also the most intense area of the semicircle at lower temperatures, remains.

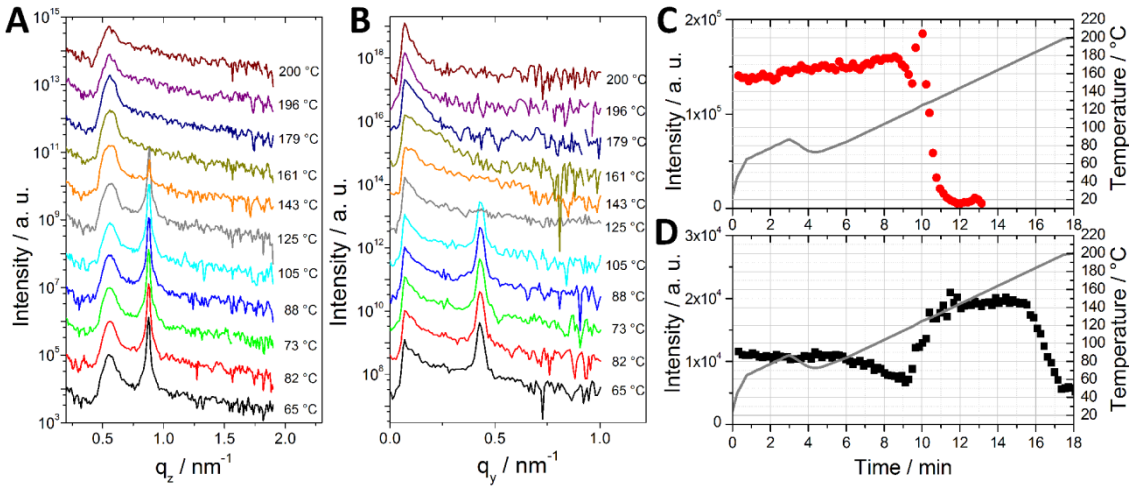

Figure 73: Evolution of the out-of-plane (A) and in-plane (B) scattering signal of a NIL-structured PSiF-DBT film (periodicity: 180 nm) during a heating run to 200°C with a heating rate of 10°C/min, approx. every 10th measurement is shown, the curves are shifted vertically for better visibility; (C) Temperature-dependent changes in out-of-plane intensity of the "line structure peak" at approx. q_z = 0.9 nm^{-1}; (D) Temperature-dependent changes in out-of-plane intensity of the wings of the Yoneda Peak at approx. q_z=0.55 nm^{-1}.

In Figure 73A, the evolution of the out-of-plane scattering (retrieved by integration of vertical cuts of the GISAXS patterns) with increasing temperature is shown. At low temperatures, the scattering signal exhibits two distinct peaks, the contribution of the in-plane wings of the Yoneda peak integrated in the out-of-plane direction at around q_z = 0.55 nm^{-1} and the peak stemming from the periodic line structure caused by the truncation rod scattering at approx. q_z = 0.9 nm^{-1}. The latter is visible up to a temperature of 143°C, before it vanishes. The in-plane cuts showing a similar behaviour are presented in Figure 73B. The effect of the NIL structure decomposition is visualized in more detail in Figure 73C, where the temperature-dependent intensity of this peak (obtained from fitting of the peak with Lorentzian function) is plotted. The intensity stays almost constant up to a temperature of about 110°C. At this temperature, the peak starts to become weaker until it decreases steeply at 130°C. From these changes, it can be assumed that the glass transition temperature of PSiF-DBT is about 110°C or even below, although it could not be experimentally determined by differential scanning calorimetry (DSC) measurements by us and others.[258] Above a temperature of 140-145°C the peak is not detectable any more in the out-of-plane scattering signal. The intensity of the wings of the Yoneda peak with increasing temperature is shown in Figure 73D. The intensity increases in the same temperature range in which the "line structure peak" steeply decreases. The increase in the out-of-plane intensity of the wings

of the Yoneda peak indicates that the nanostructured polymer layer becomes rougher in this temperature range, which leads to the conclusion that the ordered well defined layer has changed to a rougher and more disordered structure. At a later stage of the heating run, at about 180°C, the out-of-plane intensity decreases again, which is an artefact as observed in the in-plane-cuts of Figure 73B. Here the roughness increases again due to the changes of the slope, which might be an indication for a further blurring of the material.

As already stated before, the results on the thermal stability obtained from GISAXS measurements cannot be directly compared with these obtained from SEM images. The SEM images were mainly acquired to get a first indication about the thermal behavior of samples and were done with samples having periodic line structures of 500 nm, which were annealed on a simple laboratory heating plate without cover, while the GISAXS measurements were done inside a calibrated heating cell using samples with a periodic line structure of 180 nm. Both the small uncertainty concerning temperature of the laboratory heating plate and the different periodicities of the line structures can explain the slightly higher temperature stability of the nanostructures observed by SEM.

However, according to the results of the SEM as well as the GISAXS analyses, the two criteria for a possible realization of a nanostructured polymer/CIS hybrid layer - a reasonable thermal and solvent stability - are fulfilled.

In a further step, the formation of a CIS layer on the nanostructured polymer film from copper and indium xanthates was investigated by a combined time resolved GIWAXS/GISAXS experiment. Therefore, a nanostructured polymer layer on a silicon substrate was coated with a copper and indium xanthate layer via doctor blading and after drying, the sample was subsequently heated to 200°C (heating rate 10°C/min) in the same measuring cell.

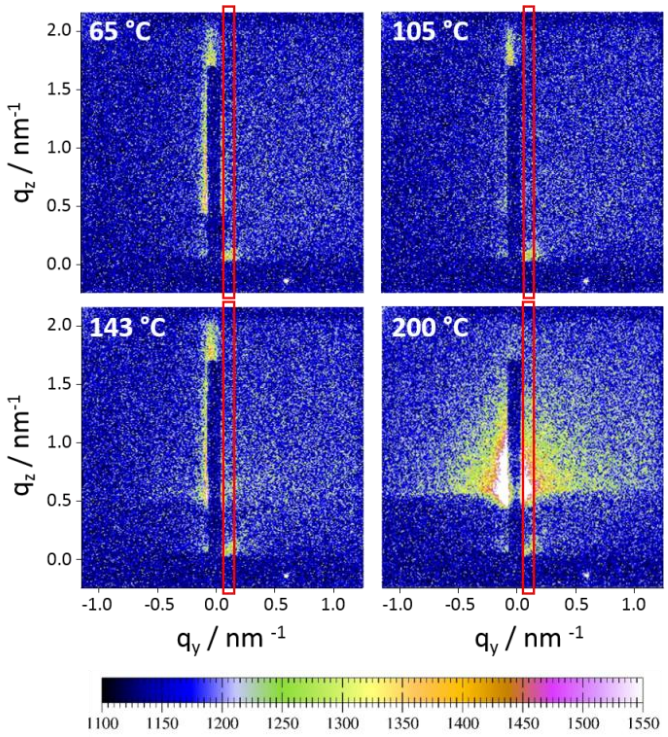

Figure 74: GISAXS images of the nanostructured polymer film (periodicity: 180 nm) covered with metal xanthates at different temperatures during the heating run from room temperature to 200°C. The red boxes indicate the vertical areas for integration.

The GISAXS images of the sample at different temperatures during one heating run are presented in Figure 74 and the areas for vertical integration are indicated with red boxes. The resulting out-of-plane at qy=0.058 nm^{-1} of the GISAXS patterns are shown in Figure 75A. Because the nanoimprinted comb structure is now covered by a dense layer of the metal xanthates and later in the heating run with a metal sulfide layer, no signal of the comb structure is detected in this case. The pronounced change in the GISAXS pattern at a temperature between 155 and 173°C stems from increased diffuse scattering of the sample. This can be explained by the fact that the metal xanthates decompose during the heating run, organic decomposition products evaporate out of the layer and a film consisting of CIS nanocrystals is formed. Due to the evaporation of decomposition products and the increased density of the CIS nanoparticles compared to the metal xanthates, the volume of the film shrinks, going along with an increase of porosity, which is visible in the GISAXS patterns. The patterns at higher temperatures follow a power law behavior ($I(q) \propto (q_y^2+q_z^2)^{-\alpha/2}$) with a Porod exponent of 2.72. This value is typical for porous structures with a large size distribution. One power law fit is exemplarily shown as a red line in Figure 75A for the GISAXS pattern measured at 200°C. No indications of particle scattering have been observed in the measured

q-regime. The small peak at q_z=0.46 nm^{-1} is due to the broadening of the specular reflected beam caused in the in-plane direction by the increased surface roughness of the copper and indium xanthate layer after decomposition and heating, therefore, it becomes visible in the out-of-plane cuts.

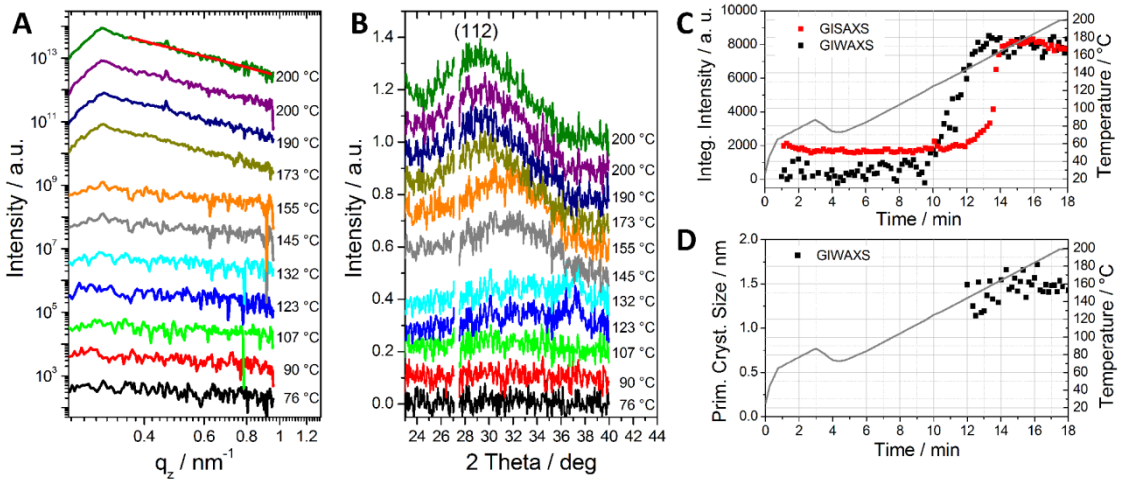

Figure 75: Temperature-dependent evolution of the vertical cuts of the GISAXS patterns of the nanostructured polymer film (periodicity: 180 nm) covered with metal xanthates (A) and the (112) peak of CIS in the GIWAXS signal (B) during a heating run to 200°C with a heating rate of 10°C/min. Approx. every 10th measurement is shown. For better visibility, the vertical cuts as well as the X-ray patterns are shifted vertically; (C) Porod invariant of the GISAXS as well as integrated intensity of the GIWAXS patterns calculated between 0.58 and 1.70 nm^{-1} as well as 24 and 38° 2 theta, respectively, plotted versus reaction time and temperature; (D) Primary crystallite size in the nanocrystalline CIS layer estimated using Scherrer equation.

The GIWAXS signals acquired during the heating run are depicted in Figure 75B. It is clearly visible that the (112) peak of CIS is detectable in the 2 theta range of 29-30° starting at a temperature of about 140°C. This issue is outlined in more detail in Figure 75C, where the evolution of the integrated intensity of the GIWAXS pattern calculated between 24 and 38° 2 theta is plotted versus reaction time and temperature. Additionally, the Porod invariant "Q" [259] (see supporting information), which represents the volume fraction of the structures, has been plotted for comparison. The intensity of the GIWAXS signal starts to increase at a heating time of about 10 min, which corresponds to a temperature of 125-130°C. At a temperature of about 150°C, the increase of the signal ceases. From then on, the signal stays constant until the end of the heating run, which indicates that the formation of the CIS phase seems to be completed at about this temperature. The Porod invariant derived from the GISAXS measurements

increases a bit later in the heating run (at approx. 155°C), when the formation of the CIS nanoparticles has been just completed and also the decomposition products have evaporated from the layer, indicating an increasing porosity of the film in this stage of the heating run.

Figure 75D shows that the primary crystallite size in the nanocrystalline CIS layer, which was estimated using the Scherrer equation and the full width at half maximum of the (112) peak obtained from fitting of the peak with Lorentzian function, is about 1.5 nm. Therefore, these structures are too small to be resolved by the GISAXS measurements due to the limited q-range. Nevertheless, this finding points out that the conversion of the metal xanthates to the CIS phase is initiated shortly before the nanoimprinted line structure starts to become slightly blurred, which is at about 140-145°C. This, in turn, leads to the conclusion that a realization of a nanostructured polymer/CIS absorber layer should be possible, as we also assume that once the CIS layer is formed on the polymeric nanostructure, it should provide a certain support to the polymer line structure, even at higher temperatures.

Thus, the next step was to prepare hybrid solar cells with a NIL-structured polymer/CIS hybrid absorber layer. For this purpose, nanoimprinted line structures in PSiF-DBT were prepared on glass/ITO/PEDOT:PSS/PSiF-DBT samples. The total sample area was 7.5 x 2.4 cm, whereby only about 2.4 x. 2.4 cm in the middle of the substrate were nanostructured. Thus, the influence of the nanostructuring compared to a flat polymer/CIS bilayer geometry on the solar cell performance could be directly determined and compared on a single substrate, on which the structured and non-structured parts were further processed in exactly the same way. After NIL-structuring, a mixed copper- and indium xanthate solution (solvent mixture: isopropanol, dichloromethane, pyridine (4:2:1 vol:vol:vol)) was applied to the partly nanostructured PSiF-DBT layer by doctor blading, whereby no differences in wetting were observed during the coating process between structured and non-structured areas. Subsequently, the substrates were heated to 160°C to form the CIS layer on the polymer and the solar cell fabrication was finally finished with the deposition of aluminum electrodes via thermal evaporation.

The SEM images of ion polished cross sections of as prepared hybrid solar cells with nanostructured and flat interfaces, respectively, are presented in Figure 76.

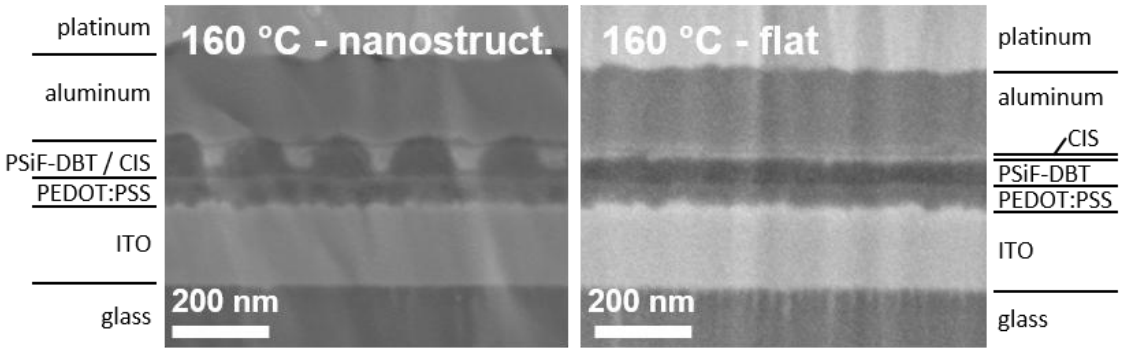

Figure 76: SEM images of cross sections of hybrid solar cells comprising a polymer/CIS absorber layer with nanostructured (periodicity: 180 nm) as well as flat interface prepared at 160°C.

The about 150 nm thick ITO layer is covered by an approx. 30 nm thick PEDOT:PSS layer. In the cross section of the nanostructured solar cell it is evident that the approx. 100 nm thick nanostructured polymer layer is filled with CIS. In the flat bilayer absorber layer, the 50 nm thick polymer layer is covered by a CIS layer with a thickness of about 20 nm. The aluminum electrode has a thickness of approx. 170 nm.

Figure 77A shows the IV curves of the hybrid solar cells with flat and nanostructured hybrid interface prepared at an annealing temperature of 160°C.

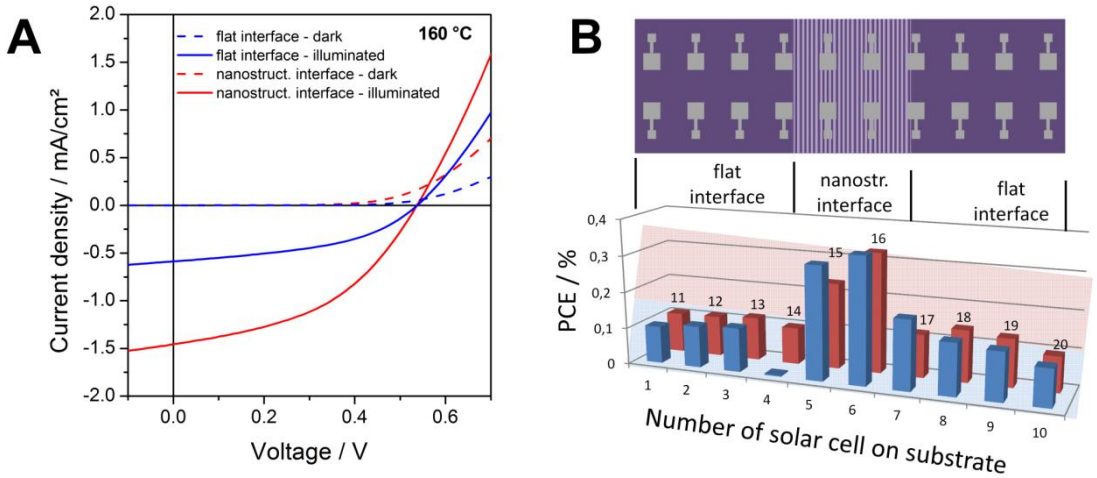

Figure 77: (A) IV curves measured in the dark and under 100 mW/cm² illumination of hybrid solar cells with flat and nanostructured (periodicity: 180 nm) interfaces prepared at 160°C and (B) distribution of PCEs of solar cells with flat and nanostructured interfaces over one typical substrate; position 4 was short circuited.

The characteristic parameters extracted from the IV curves are summarized in Table 13. Figure 77B shows the power conversion efficiencies of all 20 solar cells prepared on one substrate. The positions 5, 6 as well as 15 and 16 had a nanostructured absorber layer, while the other solar cells had a flat interface between PSiF-DBT and CIS. It can be clearly seen that the average PCE of the solar cells with flat interface lies between 0.1 and 0.15%, while the devices with nanostructured interface exhibit values around 0.3%. This improvement in PCE is attributable to an increased I_{SC} in the nanostructured device (I_{SC} – flat interface: 0.5 – 0.6 mA/cm²; I_{SC} – nanostructured interface: 1.4 – 1.5 mA/cm²). The V_{OC} as well as the FF stay constant at values of 537 mV and 45%, respectively. The mean values and their standard deviations of the characteristic parameters of typical solar cells with flat and nanostructured interface prepared at 160°C are also given in Table 13.

Table 13: Characteristic parameters of hybrid solar cells with flat and nanostructured (periodicity: 180 nm) interfaces prepared at 160°C.

	Temp. / °C	Interface	V_{OC} / V	I_{SC} / mA/cm²	FF / %	PCE / %
values from IV curves in Figure 77A	160	flat	0.537	0.59	45.5	0.14
		nanostr.	0.537	1.46	44.6	0.34
mean values and std. deviations	160	flat	0.532 ± 0.009	0.58 ± 0.02	43.7 ± 2.0	0.13 ± 0.1
		nanostr.	0.537 ± 0.007	1.32 ± 0.18	43.4 ± 1.1	0.30 ± 0.04

Furthermore, it is interesting to note that the slope of both the dark and the illuminated IV curves of the nanostructured device is significantly steeper, which suggests a decreased series resistance (R_S) in the nanostructured devices (R_S – flat interface: ~235 Ω*cm²; R_S – nanostructured interface: ~125 Ω*cm²).

Furthermore, we investigated polymer/CIS hybrid solar cells prepared at 195°C instead of 160°C, a temperature at which the imprinted nanostructure in the PSiF-DBT layer is definitely not well defined (see Figure 71D).

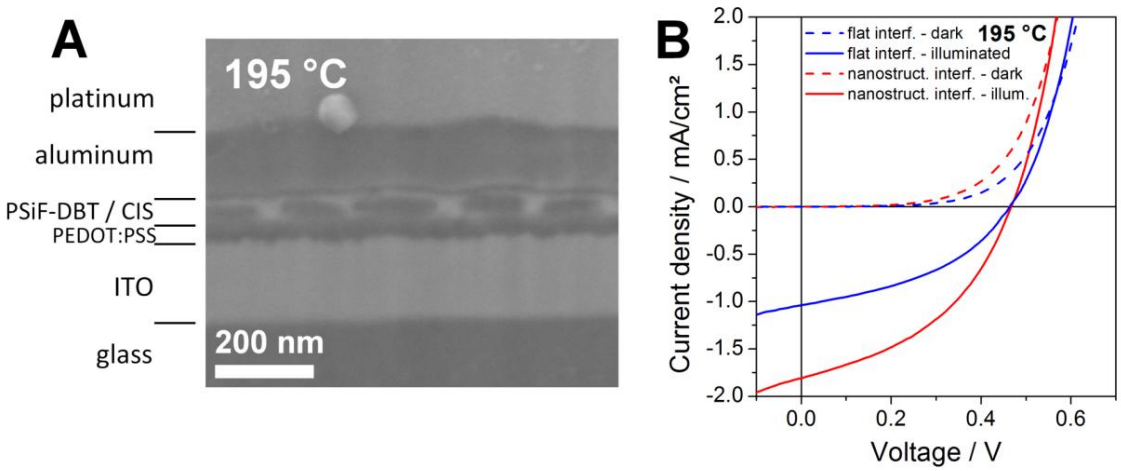

Figure 78: (A) SEM image of an ion polished cross section of a hybrid solar cell with nanostructured interface prepared at 195°C, (B) IV curves measured in the dark and under 100 mW/cm² illumination of hybrid solar cells with flat and nanostructured interface prepared at 195°C. The solar cells were prepared using nanostructured polymer films with a periodicity of 180 nm.

The SEM image of a cross section of such a solar cell prepared at 195°C (Figure 78A) exhibits, as expected, that the nanostructure has changed significantly. It seems that the comb structures deliquesce, though remains of the periodic structures are still visible. The IV curves of the prepared solar cells, shown in Figure 78B, exhibit a similar picture to the one described for the devices prepared at 160°C. Also in this case the R_S of the solar cell with the nanostructured interface is lower (R_S – flat interface: ~150 Ω*cm²; R_S – nanostructured interface: ~80 Ω*cm²) and the I_{SC} of the device with nanostructured interface is about 80% higher than that of the device with flat interface. The V_{OC} as well as FF are similar, which results in a significant difference in PCE - flat interface: 0.2%, nanostructured interface: 0.35% (see Table 14).

Table 14: Characteristic parameters of hybrid solar cells with flat and nanostructured interfaces prepared at 195°C. The solar cells were prepared using nanostructured polymer films with a periodicity of 180 nm.

	Temp. / °C	Interface	V_{OC} / V	I_{SC} / mA/cm²	FF / %	PCE / %
values from IV curves in Figure 78B	195	flat	0.467	1.04	41.3	0.20
		nanostr.	0.467	1.81	42.3	0.35
mean values and std. deviations	195	flat	0.474 ± 0.008	1.10 ± 0.08	41.7 ± 0.4	0.22 ± 0.01
		nanostr.	0.459 ± 0.008	1.74 ± 0.08	41.9 ± 0.6	0.33 ± 0.01

3.17.4 Conclusion

Based on this study, it can be concluded that the preparation of nanostructured polymer/metal sulfide hybrid solar cells using NIL for structuring a conjugated polymer layer, which is coated with a metal xanthate solution and subsequently thermally annealed at moderate temperatures to form the inorganic metal sulfide on the nanostructure, is generally feasible. The performed temperature resolved GISAXS study revealed that a very good thermal stability of the polymer nanostructures is given up to a temperature of 130 – 140°C. Above this temperature, the nanostructure is slightly blurred, as was seen in the SEM images. SEM images also indicated that the polymer nanostructures are sufficiently thermally stable, so that at an annealing temperature of 160°C the imprinted line structure is largely maintained in the polymer phase. At an annealing temperature of 195°C, the nanostructure appears much more blurred in the SEM images. Moreover, the stability of the nanostructures against the solvent used for dissolving the metal xanthates, a mixture of isopropanol, dichloromethane and pyridine turned out not to be a critical issue in the solar cell fabrication process.

The nanostructured solar cells prepared at 160°C and 195°C show a significantly improved power conversion efficiency compared to similarly prepared flat bilayer devices, which is based on a distinct improvement of the short circuit current in the nanostructured solar cells. To further optimize nanostructured hybrid solar cells

prepared via this approach, the temperature of the annealing step has to be kept as low as possible in order to retain a very defined nanostructure. A reduction of the annealing temperature could be achieved by addition of amines to the metal xanthate solution, which were recently shown to facilitate crystallization of the metal sulfide at lower temperatures.[260] Therefore, we assume that by optimizing the imprinting process and imprinting nanostructures with smaller periodicities as well as applying lower annealing temperatures to form the metal sulfide phase, the power conversion efficiencies of such nanostructured hybrid solar cells should be significantly improved.

3.17.5 Supporting Information to: Nanoimprinted comb structures in a low bandgap polymer: thermal processing and their application for hybrid solar cells

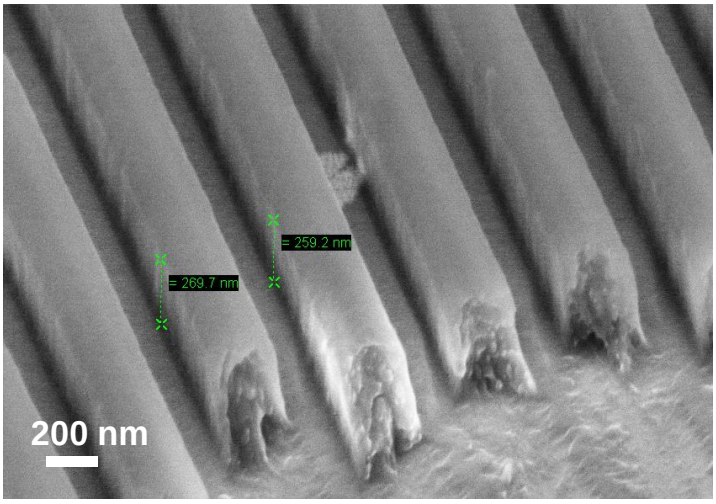

Figure 79: SEM image (measured in a 45° angle) of a NIL-structured PSiF-DBT layer (periodicity: 500 nm) to determine the height of the imprinted line structures, which is 260 - 270 nm.

Analytical expression for the Porod invariant "Q":

"Porod invariant" "Q" is given by the second moment of the scattered intensity and is related to the electron density contrast $\Delta\rho$ and the volume fraction ϕ_p of the particles or precipitates in a two phase system (Ref. 259).

$$"Q" = \int dq \cdot q^2 \cdot I(q) \propto \Delta\rho^2 \cdot \phi_p \cdot \left(1 - \phi_p\right)$$

with I(q) as scattered intensity and q as scattering vector

4. Summary and outlook

This work focused on the stability of hybrid solar cells consisting of conjugated polymers and inorganic semiconducting nanoparticles. Hybrid solar cells combine the beneficial properties of inorganic solar cell materials with the easy processability of polymeric materials and show already encouraging efficiencies of up to 5%.[40]

The hybrid solar cells have been prepared according to a novel route for the direct formation of CIS nanoparticles within the polymer matrix.[85] A mixture of precursor chemicals for the formation of CIS (i.e copper and indium xanthates) and a semiconducting polymer gets dissolved together and coated on a substrate. During a moderate thermal annealing step below 200°C the precursor chemicals are decomposed into CIS and a hybrid nanocomposite layer is obtained. No additional nanoparticles-capping ligands that may alter device performance are needed; the polymer acts as capping agent and thus prevents extensive particle growth.

Polymer-CIS hybrid solar cells in the architecture ITO|PEDOT:PSS|PSiFDBT-CIS|Al showed the best PCEs so far,[49] however, the limited stability of these devices was an issue. Under permanent illumination in atmospheric atmosphere conditions or even in inert gas, solar cells degraded within hours. In the first experiments selective parts of the complete device architecture have been replaced and the influence on the operational stability has been examined. The results revealed that the absorber layer - cathode interface plays a crucial rule for device stability. The replacement of aluminum with silver as cathode material lead to significantly enhanced stability of the devices under permanent illumination in air. However, the stability measurements in air and photo-bleaching studies by the means of UV-VIS spectroscopy demonstrated that hybrid solar cells have to be protected against oxygen and water to prevent oxidation reactions, otherwise device degradation within days occurs.

Glass-glass encapsulated devices with Ag electrodes showed, if no catastrophic failure due to Ag migration and device shunting occurs, extraordinary stable behavior. A PSiFDBT-CIS hybrid solar cell with Ag electrodes was tested over a time range of about 3 years (28500 h, whereof 16900 h under illumination with 1000 W/m^2) and still approximately 50% of its initial PCE has been maintained.

From accelerated ageing tests of encapsulated PSiFDBT-CIS hybrid solar cells with Ag electrodes, it was found that elevated temperatures of 75°C and 85°C without raised

humidity do not cause device degradation, whereas an encapsulated device that has been undertaken 3 damp-heats test (85°C, 85%RH) has lost ~30% of PCE during each week of exposure. Ageing experiments under different atmospheres (i.e. dry nitrogen, H_2O enriched nitrogen, dry synthetic air and H_2O enriched synthetic air) revealed that oxygen is the predominant factor for device degradation and humidity in the absence of oxygen does not cause additional device failures at moderate temperatures, while humidity in the presence of oxygen accelerates degradation.

However solar cells with Ag electrodes show lower V_{OC}-values compared to Al electrodes, which limit their PCEs. To circumvent this issue, different cathode interlayers (Cs_2CO_3, Mg, Ti and TiO_x) have been introduced and the influence on the performance and stability has been evaluated.

In respect of performance and operating stability, solar cells with Ti or TiO_x interlayers showed the most promising results and have been studied in detail. The TiO_x interlayers in these series have been prepared via thermal evaporation of titanium under moderate vacuum conditions in oxygen containing atmosphere, whereas Ti interlayers have been deposited under high vacuum conditions. Devices with Ti and TiO_x interlayers have been characterized in a depth profile analysis by the means of XPS combined with argon ion sputtering. By introducing TiO_x as well as Ti interlayers between absorber layer and Ag electrodes, enhanced V_{OC} and FF values of the devices could be observed, which led to an increase in PCE from 1.6% to about 2.1%. Glass-glass encapsulated hybrid solar cells with TiO_x or Ti interlayer showed stable performance over a testing period of several thousand hours of continuous illumination. The introduction of TiO_x and Ti cathode interlayers enhanced also the stability of solar cells with Al electrodes, but their lifetimes are still not comparable with devices using Ag electrodes.

In further experiments a solution processed TiO_x cathode interlayer was introduced and the influence on the performance and stability on hybrid solar cells with Ag as well as Al electrodes has been evaluated; however, better results regarding efficiency and stability have been obtained from solar cells with evaporated TiO_x interlayers.

As in all stability measurements presented in this work, the solar cells have been kept at open circuit conditions between collecting IV-curves. In order to evaluate the impact of the load condition during ageing of PSiFDBT-CIS hybrid solar cells with Ag electrodes, one device has been kept at open circuit condition and another, parallel prepared one

has been kept at maximum power point condition between collecting IV-curves during the lifetime tests. The solar cells have been monitored in a time frame of 4500 hours and the device that has been kept at V_{OC} showed stable behaviour over the whole testing period, while at the device that has been kept at mpp showed a slight decrease in PCE after 3500 hours of operation. Overall, no large difference in degradation was observable between the different types of measuring.

In further studies, the influence of device architecture (regular versus inverted) and different interlayers on performance and lifetime of PCDTBT-CIS hybrid solar cells was explored. The anode interlayers PEDOT:PSS, V_2O_5, MoO_3 have been used as hole extraction layers between absorber and anode and TiO_x has been used as electron extraction layer between absorber and cathode. Depending on the position of the interlayers in the device stack, the ITO-glass substrate acts as anode (regular architecture) or cathode (inverted architecture). All three anode interlayers were successfully applied in solar cells in regular architecture. Using an inverted device design, a PEDOT:PSS interlayer and Ag electrodes, open circuit voltages of 550 mV could be obtained; however, while showing current densities above 10 mA/cm², the FF-values were lower compared to solar cells in regular geometry, which was limiting the PCE of the inverted solar cells to 2.1%. However, inverted solar cells with V_2O_5 hole extraction layers could not be obtained due to possible incompatibility of the V_2O_5 coating process with the underlying absorber layer. In the case of MoO_3 anode interlayers, the introduction of additional layers led to working inverted solar cells. In both regular and inverted device architectures, hybrid solar cells with PEDOT:PSS anode interlayer showed the best results. A solar cell in inverted architecture having a PEDOT:PSS interlayer and an additional CIS layer showed promising stability and maintained its high open circuit voltage over 2500 hours of continuous illumination. Similar inverted devices without additional CIS layer showed only 45-60 hours of stable behavior before the devices suddenly lost their open circuit voltages, most likely due to short circuiting of the device due to migration of silver.

Overall, the obtained results concerning stability of polymer-nanoparticle hybrid solar cells are quite encouraging. As the annual solar irradiation in the Meddle European latitude accounts to 1100-1200 kWh/m^2,[261] is a testing period of 1000 hours under permanent illumination of 1000 W/m^2 in terms of absorbed photons nearly equivalent with one year of outdoor exposure. The lifetimes are comparable with lifetimes of

polymer-PCBM solar cells, if appropriate interlayer-electrode combinations and proper encapsulation are used.

The performance and stability of hybrid solar cells strongly dependent on electrodes and interlayers extracting the charges generated in the absorber layer. It has been shown that the use of "low" work function metals, commonly used as cathode materials in organic photovoltaics can be avoided by the introduction of cathode-interlayer in combination with more noble metal electrodes or the realization of the so called inverted architecture. In both cases, relative efficient and stable hybrid solar cells could be fabricated. Still a crucial factor limiting the solar cell lifetime is the migration of silver through the thin absorber layers (50-70 nm) leading to short circuiting of the device. This issue still has to be overcome, possibly with an adequate substitute of silver as electrode material. Interestingly also a reduced conversion temperature of the xanthates at 140°C, made possible with an n-hexylamine additive,[99] turned out to be a further parameter that positively influences the performance and lifetime of the devices and has thus to be studied in more detail.

Additional stability testing procedures like outdoor testing (ISOS-O), thermal cycling testing (ISOS-T) and solar-thermal-humidity cycling (ISOS-LT) have not been undertaken up to now and have to be conducted. Up to now only glass-glass encapsulated hybrid solar cells have been tested regarding their operational stability. The introduction of flexible devices opens new challenges. Flexible encapsulation materials typically show distinct higher OTR and WVTR values, furthermore additional aspects like maximum bending radius of such devices would be an issue.

In the second part of the work conjugated polymer layers structured by nanoimprint lithography (NIL) have been investigated toward their suitability for the fabrication of nanostructured polymer-metal sulfide hybrid solar cells.

Major prerequisites for optimal function of hybrid solar cells include large interfaces between the organic and inorganic phase, providing effective charge separation, as well as continuous pathways for transporting the separated charge carriers to the respective electrodes. A vertically bicontinuous and interdigitated heterojunction between the organic and inorganic phase is regarded to as an ideal structure for optimal charge separation as well as charge transport.[234] Such interdigitated structure can be prepared by NIL.

In a first approach the thermal stability of the nanoimprinted structures with a periodicity of 180 nm in PSiFDBT layers has been studied by means of scanning electron microscopy and grazing incidence small angle X-ray scattering, which revealed a reasonable thermal stability up to 145°C and sufficient robustness against the solvent mixture used in the subsequent fabrication process. Subsequently, nanostructured PSiFDBT-CIS hybrid solar cells have been fabricated via the infiltration and thermal decomposition of a mixture of copper and indium xanthates. Although this step needs temperatures of more than 160°C the nanostructures are retained in the final polymer-CIS layers. The nanostructured solar cells show significantly improved power conversion efficiency compared to similarly prepared flat bilayer devices, which is based on a distinct improvement of the short circuit current in the nanostructured solar cells due to an increased donor-acceptor interface area. Next steps for optimization of hybrid solar cells in nanostructured bilayer architecture could be a reduction of the periodicity to the range of the exciton diffusion length of the semiconductors as well as a reduction of the conversion temperature of the xanthates due to an n-hexylamine additive.

5. Experimental

5.1 Solar cell preparation

The preparation of the hybrid solar cells presented in the chapters 3.1 - 3.8 has been prepared as follows. The preparation of the hybrid solar cells presented in the chapters 3.9 - 3.15 have been prepared as described in 3.10.2.

5.1.1 Etching

Solar cells have been fabricated on ITO covered glass slides (Delta Technologies). The ITO layer has a thickness in the range of 100 nm, showing a resistance of 15-25 Ω/sq. In order to avoid shorts during contacting the metal electrodes with contact pins, defined parts of the ITO electrode have been etched. The etching step was done using hydrochloric acid and zinc powder. The hydrogen *in statu nascendi* that is formed during the occurring redox reaction offers a reduction potential that is high enough to decompose the ITO layer. Parts of ITO that should not be removed via etching have been protected with adhesive tape.

5.1.2 Cleaning

After etching, residues from the adhesive tape have been removed with acetone and the substrates have been subsequently cleaned by ultrasonic treatment (VWR ultrasonic cleaner) in deionized water and isopropanol for 20 min at room temperature, respectively.

5.1.3 Preparation of hole transport layer (optional)

A PEDOT:PSS hole extraction layer (Clevios P VP.Al 4083, Heraeus) was spin coated (2500 rpm, 30 s) on the substrates using a Karl Suss Technique S.A. CT62 spin coater and subsequently heated to 150°C for 10 min inside a glove box. Depending on the lot of the PEDOT:PSS aqueous solution, the formulation has been diluted with deionized H_2O up to 1:1 to achieve similar layer thicknesses in the range of 40 nm. The PEDOT:PSS solution was filtered through a 0.45 µm pore size PVDF filter prior to coating.

Alternatively, a Plexcore® OC hole extraction layer solution was applied pure, has not been filtered but was spin coated and heated at the same conditions as PEDOT:PSS.

5.1.4 Preparation of the absorber precursor layer

For the preparation of the absorber layer, a two-step coating has been applied. The precursor solution for the first coating consisting of 5 mg/mL polymer (PSiFDBT, 1-Material; PCDTBT, ADS or TPPEPPE, Jenpolymer Materials), copper xanthate (25.0 mg/mL, 1 equiv.) and indium xanthate (114.9 mg/mL, 1.7 equiv.) dissolved in chlorobenzene was deposited by doctor blading (speed: 7.5-10 mm/s, substrate temperature: 40°C, wet film thickness: 150 µm) using a Erichsen model 509-1 doctor blading machine. After the first coating, the substrates were dried on the heating plate for 20 seconds at a temperature of 60°C. For the second coating step, a precursor solution consisting of 2.5 mg/mL polymer (PSiFDBT, PCDTBT or TPPEPPE), copper xanthate (17.9 mg/mL, 1 equiv.) and indium xanthate (82.1 mg/mL, 1.7 equiv.) dissolved in chlorobenzene has been doctor bladed at the same conditions. The second coating with lower polymer concentration but, in relation to the polymer, higher inorganic content generates on the one hand side a gradient of the donor-acceptor composition and on the other hand side fills pores in the first layer and thus prevents shorts. The coating procedure has been performed under inert conditions inside a glove box.

5.1.5 Thermal conversion step

The thermal conversion of the xanthates was carried out in a tube furnace (Heraeus) under dynamic vacuum conditions. The coated substrates were annealed at 200°C using a heating rate of 28.5°C/min and holding the final temperature at 200°C for 15 minutes.

5.1.6 Deposition of the back electrodes and cathode interlayer

200 nm thick aluminum or silver back electrodes were thermally evaporated (Baltec MED020) through a shadow mask onto the absorber layer to get defined single solar cells with an active area of 3x3 mm. The evaporations of the metals have been carried out at evaporation rates between 0.1 and 10 nm/s (starting with lower values and increasing the rate during deposition) at air pressures around $5*10^{-5}$ mbar. The evaporation rates and the final thicknesses have been measurement with a crystal oscillator.

The deposition of the Cs_2CO_3 (1 nm) and Mg (20 nm) and Ti (5 nm) interlayers has been done at evaporation rates between 0.1 and 1.5 nm/s at air pressures around $5*10^{-5}$ mbar.

5.1.7 Encapsulation

For encapsulation, external electrical connectors (copper conductive adhesive tape, Christine Gröpl) have been mounted at the ITO and the metal electrode, respectively, and an additional backsheet glass slide has been glued onto the device stack glass|ITO|anode-interlayer|absorber-layer|cathode. For that purpose an ultrafast curing super glue (UHU sofortfest) and two different dedicated encapsulation epoxy glues for organic electronic devices, a one component light curable epoxy (Ossila EE1) and a two component epoxy (Epotek 302-3M) have been employed. To avoid device degradation due to the malfunction of the encapsulation and the electrical contacts, different device geometry was chosen in experiments starting from chapter 3.10. (Figure 80).

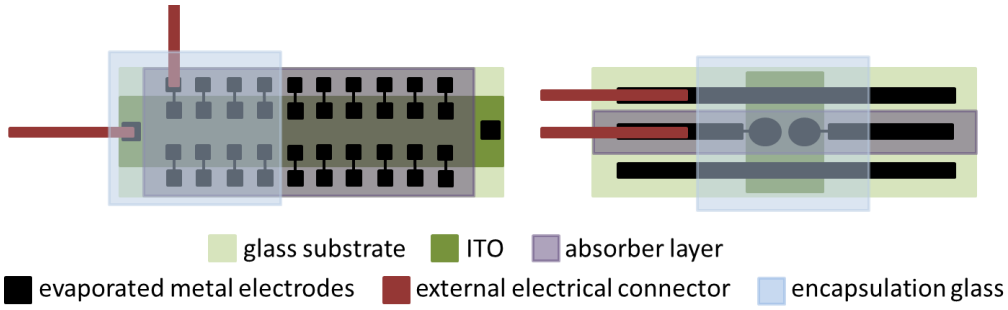

Figure 80: Schematic depiction of glass-glass encapsulated hybrid solar cells in different device geometries.

The divergent geometry was chosen in order to increase the active area of the solar cells (i.e. 0.238 cm² vs. 0.09 cm²), to increase the surface of the sealing area and to increase contact area for the external electrical connections. Additionally, the raised step height due to the external connector is avoided and thus a direct planar application of the protection glass slide is realizable as the external electrical connection can be applied outside the framework of the absorber layer encapsulation.

5.1.8 Synthesis of the solution processed TiO_x precursor in chapter 3.11

The solution processes TiO_x precursor was synthesized in a three-necked flask (100 mL) that was heated at 80°C for 1 hour prior to usage and flushed with dry N_2 during the synthesis. 5 mL of titanium(IV)isopropoxide (Sigma-Aldrich), followed by 20 mL of 2-methoxyethanol (Sigma-Aldrich) and 2 mL of ethanolamine (Aldrich) have been injected into the three-necked flask connected with a water condenser and nitrogen gas inlet and outlet. After 1 hour stirring at room temperature, the solution was heated at

80°C for 1 hour. In the following the low boiling components have been removed by distillation at 120°C under atmospheric pressure. After cooling to room temperature, 10 mL of methanol (Sigma-Aldrich) was injected to extract the TiOx sol-gel product, which was further diluted by 1:100 in methanol prior to spin coating on the absorber layer (2500 rpm, 30 s).

5.1.9 Preparation of the solution processed V_2O_5 precursor in chapter 3.12

The preparation of the solution processed precursor has been adapted from Zilberberg et al.[212] As the described route stipulates a deposition of the precursor solution via spincoating at 5000 rpm what may not be applicable with the substrate size in this work, the concentration of vanadium(V)oxytriisopropoxide (Sigma-Aldrich) in isopropanol (Sigma-Aldrich) was raised to 1.25 vol.% and rotation speed during spin coating was lowered to 3000 rpm. After deposition, the precursor layer was hydrolyzed in air at room temperature for 1 hour.

5.2 Characterization

5.2.1 Solar cell characterization

PCE values of prepared solar cells were determined from current-voltage curves recorded inside a glovebox directly after preparation using a Keithley 2400 SourceMeter, a custom made LabVIEW software and a halogen lamp (Diaprojector Braun Praximat Multimag, chapters 3.1 - 3.8) as well as a metal halide gas discharge lamp (Dedolight DLH400D, chapters 3.9ff) according to ISOS-L-1 (level 1 laboratory testing). Irradiation intensity (100 mW/cm^2) was calibrated with a pyranometer (KippZonen-CMP-11). Spectral mismatch was not considered. IV-curves have been collected by sweeping the potential from positive to negative bias voltages. No additional light masks have been applied and cells have not been cooled during measurement.

5.2.2 Stability measurements

Stability data on hybrid solar cells were collected under permanent illumination of 100 mW/cm² using a sulphur plasma lamp (LG PSH0731WA, chapters 3.1 – 3.8) and a solar simulator (Steuernagel KHS1200, chapters 3.11 - 3.16) according to ISOS-L-1 (level 1 laboratory testing). IV-curves were measured by sweeping the potential from positive to negative bias voltages using an automated system in periodic intervals 15 min, 30 min

or 60 min) and the devices were kept under open circuit conditions between the measurements. The automated system consists of Keithley 2400 source meters, a Keithley 3706A multiplexer and a custom made LabVIEW based software. Irradiation intensity was calibrated with a pyranometer (Kipp & Zonen CMP-11) and monitored in 30 min intervals using a Si-photodiode (Hamamatsu). No additional cooling was applied, resulting in a device temperature of approximately 55°C during the stability tests.

5.2.3 Light sources

In the following, emission spectra of the light sources used in this work are presented.

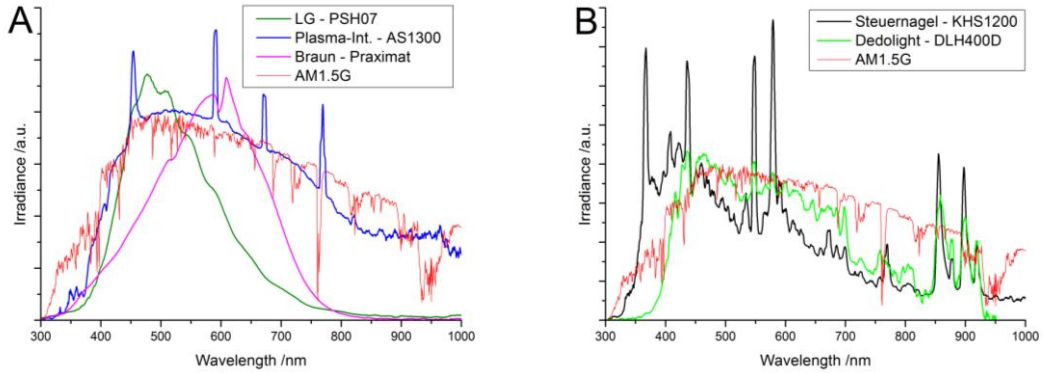

Light source spectra have been recorded with an Avantes - AvaSpec-2048 spectrometer calibrated with an Avantes - AvaLight HAL-CAL reference light source. AM1.5G spectrum was derived from Ref. 61.

5.2.4 Profilometry

Layer thickness and roughness measurements have been conducted on a Bruker DekTak XT surface profiler.

5.2.5 UV-VIS spectroscopy

Absorbance spectra presented in chapter 3.3 were recorded on a Shimadzu UV-1800 photometer. Absorption spectra presented in chapter 3.16.5 were calculated from transmittance and reflectance measurements (Absorption /% = 100% - Transmittance /% - Reflectance /%) on a Perkin Elmer Lambda 35 photometer equipped with an integrating sphere.

6. Appendix

6.1 List of abbreviations

a-Si	amorphous silicon
Alq_3	tris(8-hydroxyquinolinato)aluminum
AM	air mass
AZO	aluminium-doped zinc oxide
BCP	bathocuproine
BE	binding energy
Bphen	bathophenanthroline
C_{60}	buckminsterfullerene
CB	conduction band
CDL	Christian Doppler Labor
CIGS	copper indium gallium sulphide, selenide
CIS	$CuInS_2$
DMF	dimethylformamide
EQE	external quantum efficiency
ESR	electron spin resonance
F8T2	poly[(9,9-dioctylfluorenyl-2,7-diyl)-*co*-bithiophene]
FF	fill factor
FTO	fluorine-doped tin oxide
GISAXS	grazing incident small angle X-ray scattering
GIWAXS	grazing incident wide angle X-ray scattering
h	hour
HOMO	highest occupied molecular orbital
IEC	International Electrotechnical Committee
IPCE	incident photon to current efficiency
I_{SC}	short circuit current
ISC	intersystem crossing
ISOS	International Summit on Organic Photovoltaic Stability
IV	current-voltage
LIOS	Linz Institute for Organic Solar Cells
LUMO	lowest unoccupied molecular orbital
MDMO-PPV	poly[2-methoxy-5-(3′,7′-dimethyloctyloxy)-1,4-phenylenevinylene]

MEH-PPV	poly[2-methoxy-5-(2-ethylhexyloxy)-1,4-phenylenevinylene]
NIL	nanoimprint lithography
OLED	organic light emitting diode
OPV	organic photovoltaic
OTR	oxygen transmission rate
mpp	maximum power point
PCBM	phenyl-C_{61}-butyric acid methyl ester
PCDTBT	poly[[9-(1-octylnonyl)-9H-carbazole-2,7-diyl]-2,5-thiophenediyl-2,1,3-benzothiadiazole-4,7-diyl-2,5-thiophenediyl]
PCE	power conversion efficiency
PEDOT:PSS	poly(3,4-ethylene-dioxythiophene)-poly(styrenesulfonate)
PET	polyethylene terephthalate
$\mathbf{P_{max}}$	maximum power output
PSiFDBT	poly[2,1,3-benzothiadiazole-4,7-diyl-2,5-thiophenediyl-(9,9-dioctyl-9H-9-silafluorene-2,7-diyl)-2,5-thiophenediyl]
PPV	poly(*p*-phenylen-vinylen)
PV	photovoltaic
RH	relative humidity
$\mathbf{R_s}$	series resistance
$\mathbf{R_{sh}}$	shunt resistance
SEM	scanning electron microscopy
TCO	transparent conductive oxide
TEM	transmission electron microscopy
THF	tetrahydrofuran
TOF-SIMS	time-of-flight secondary ion mass spectrometry
TPPEPPE	poly[(2,3-diphenylthieno[3,4-b]pyrazin-5,7-diyl)-1,2-ethindiyl[2,5-bis(dodecyloxy)-1,4-phenylen]-1,2-ethindiyl]
VB	valence band
$\mathbf{V_{OC}}$	open circuit voltage
WVTR	water vapor transmission rate
XPS	X-ray photoelectron spectroscopy

6.2 List of figures

6.3 List of tables

6.4 List of publications

Papers

2016

S. Dunst, T. Rath, A. Reichmann, H.-T. Chien, B. Friedel, G. Trimmel, A comparison of copper indium sulphide/polymer nanocomposite solar cells in inverted and regular architecture, submitted to Synt. Met.

2014

M.V. Madsen, S.A.Gevorgyan, R. Pacios, J. Ajuria, I. Etxebarria, J. Kettle, N.D. Bristow, M. Neophytou, S.A. Choulis, L. Stolz Roman, T. Yohannes, A. Cester, P. Cheng, X. Zhan, J. Wu, Z. Xie, W.-C. Tu, J.-H. He, C.J. Fell, K. Anderson, M. Hermenau, D. Bartesaghi, L.J.A. Koster, F. Machui, I. González-Valls, M. Lira-Cantu, P.P. Khlyabich, B.C. Thompson, R. Gupta, K. Shanmugam, G.U. Kulkarni, Y. Galagan, A. Urbina, J. Abad, R. Roesch, H. Hoppe, P. Morvillo, E. Bobeico, E. Panaitescu, L. Menon, Q. Luo, Z. Wu, C. Ma, A. Hambarian, V. Melikyan, M. Hambsch, P.L. Burn, P. Meredith, T. Rath, S. Dunst, G. Trimmel, G. Bardizza, H. Müllejans, A.E. Goryachev, R.K. Misra, E.A. Katz, K. Takagi, S. Magaino, H. Saito, D. Aoki, P. M. Sommeling, J.M. Kroon, Tim Vangerven, J. Manca, J. Kesters, W. Maes, O.D. Bobkova, V.A. Trukhanov, D.Y. Paraschuk, F.A. Castro, J. Blakesley, S.M. Tuladhar, J.A. Röhr, J. Nelson, J. Xia, E.A. Parlak, T.A. Tumay, H.-J. Egelhaaf, D.M. Tanenbaum, G.M. Ferguson, R. Carpenter, H. Chen, B. Zimmermann, L. Hirsch, G. Wantz, Z. Sun, P. Singh, C. Bapat, T. Offermans, F.C.Krebs, Worldwide outdoor round robin study of organic photovoltaic devices and modules, Sol. Energy Mater. Sol. Cells 130 (2014) 281–290.

C. Fradler, T. Rath, S. Dunst, I. Letofsky-Papst, R. Saf, B. Kunert, F. Hofer, R. Resel, G. Trimmel, Flexible polymer/copper indium sulfide hybrid solar cells and modules based on the metal xanthate route and low temperature annealing, Sol. Energy Mater. Sol. Cells 124 (2014) 117-125.

S. Dunst, T. Rath, S. Moscher, L. Troi, M. Edler, T. Griesser, G. Trimmel, Influence of TiO_x and Ti cathode interlayers on the performance and stability of hybrid solar cells, Sol. Energy Mater. Sol. Cells 130 (2014) 217-224.

S. Dunst, T. Rath, A. Radivo, E. Sovernigo, M. Tormen, H. Amenitsch, B. Marmiroli, B. Sartori, A. Reichmann, A.-C. Knall, G. Trimmel, Nanoimprinted comb structures in a low bandgap polymer: Thermal processing and their application in hybrid solar cells, ACS Appl. Mater. Interfaces 6, 10 (2014) 7633-7642.

Posters

2015

G. Trimmel, T. Rath, C. Fradler, S. Dunst, I. Letofsky-Papst, R. Saf, B. Kunert, R. Resel, F. Hofer, Copper indium sulphide/polymer hybrid solar cells via the metal xanthate route, International Conference on Hybrid and Organic Photovoltaics (HOPV) 2015 Rome, Italy.

2013

S. Dunst, S. Moscher, T. Rath, T. Grießer, G. Trimmel, Ti and TiOx as cathode interlayer for efficient and stable nanocomposite solar cells, 15. Österreichische Chemietage 2013 Graz, Austria.

2012

T. Rath, M. Edler, W. Haas, S. Moscher, R. Trattnig, M. Jäger, A. Pein, V. Kaltenhauser, S. Dunst, M. Arar, C. Fradler, R. Saf, M. Postl, M. Seidl, N. Bansal, S.A. Haque, F. Hofer, E. List, G. Trimmel, Polymer/copper indium sulphide hybrid solar cells, EMRS Spring Meeting 2012 Strasbourg, France.

M. Arar, A. Pein, W. Haas, V. Kaltenhauser, C. Fradler, S. Dunst, F. Hofer, K. Norrman, F.C. Krebs, T. Rath, G. Trimmel, Fill factor enhancement for PSiF-DBT/CIS solar cells through silver-modified aluminum electrodes, Plastic Electronics 2012 Dresden, Germany.

T. Rath, M. Edler, W. Haas, S. Moscher, A. Pein, V. Kaltenhauser, S. Dunst, M. Arar, C. Fradler, R. Saf, R. Trattnig, M. Jäger, M. Postl, M. Seidl, N. Bansal, S.A. Haque, F. Hofer, E. List, G. Trimmel, A direct in situ-preparation route for organic-inorganic hybrid solar cells based on metal sulfides and conjugated polymers, Plastic Electronics 2012 Dresden, Germany.

2011

V. Kaltenhauser, T. Rath, S. Dunst, S. Moscher, A. Pein, W. Haas, F. Hofer, G. Trimmel, Influence of different interlayers on the performance of nanocomposite solar cells, EMRS Spring Meeting 2011 Nice, France.

S. Dunst, S. Nestl, A. Pein, S. Moscher, V. Kaltenhauser, T. Rath, G. Trimmel, Influence of electrode materials and different interlayers on the stability of nanocomposite solar cells, International Summit On OPV Stability (ISOS) 2011 Denver, USA.

T. Rath, A. Fischereder, M. Edler, S. Moscher, R. Trattnig, G. Mauthner, W. Haas, S. Dunst, F. Hofer, E. List, G. Trimmel, Metal xanthates as precursors for efficient solution processed $CuInS_2$-polymer nanocomposite solar cells, MRS Fall Meeting 2011 Boston, USA

G. Trimmel, V. Kaltenhauser, S. Dunst, T. Rath, S. Moscher, A. Pein, W. Haas, F. Hofer, Influence of different interlayers on the performance of nanocomposite solar cells, 26th European Photovoltaic Solar Energy Conference and Exhibition (26th EU PVSEC) 2011 Hamburg, Germany.

2009

A. Fischereder, E. Maier, S. Dunst, T. Rath, W. Haas, J. Albering, F. Hofer, G. Trimmel, Comparison of metal sulfides in organic - inorganic nanocomposite solar cells by and in-situ formation process, E-MRS 2009 Strassbourg, France.

Oral Presentations

2015

G. Trimmel, C. Fradler, T. Rath, S. Dunst, I. Letofsky-Papst, R. Saf, B. Kunert, F. Hofer, R. Resel, Flexible copper-indium-sulfide/polymer hybrid solar cells via a low temperature conversion route of metal xanthates, Nano and Photonics 2015 Mauterndorf, Austria.

D. Reishofer, H. Ehmann, S. Dunst, G. Trimmel, S. Spirk, In-situ synthesis of Bi_2S_3-nanoparticles in a polysaccharide matrix, EPNOE International Polysaccharide Conference 2015 Warsaw, Poland.

2014

C. Fradler, T. Rath, S. Dunst, I. Letofsky-Papst, R. Saf, B. Kunert, F. Hofer, R. Resel, G. Trimmel, Flexible polymer/copper indium sulfide hybrid solar cells based on the metal xanthate route and low temperature annealing using hexylamine, E-MRS Spring Meeting 2014 Lille, France.

2013

M. Arar, A. Pein, S. Dunst, W. Haas, F. Hofer, K. Norrman, F.C. Krebs, T. Rath, G. Trimmel, Comparing efficiency and stability of conventional cathodes with a novel silver nanoparticle/aluminum cathode in hybrid solar cells, IEEE Photovoltaic Specialists Conference 2013 Tampa, USA.

2012

S. Dunst, S. Nestl, S. Moscher, C. Fradler, T. Rath, G. Trimmel, Stability issues of $CuInS_2$-polymer hybrid solar cells, EMRS Spring Meeting 2012 Strassbourg, France.

T. Rath, M. Arar, A. Pein, C. Fradler, V. Kaltenhauser, M. Edler, S. Moscher, R. Trattnig, E. List, W. Haas, S. Dunst, F. Hofer, G. Trimmel, Copper indium sulphide/polymer nanocomposite solar cells, 27th European PV Solar Energy Conference and Exhibition 2012 Frankfurt, Germany.

2011

S. Dunst, A. Pein, E. Maier, S. Nestl, T. Rath, G. Trimmel, Einfluss von Elektrodenmaterialien auf die Stabilität von Nanokomposit-Solarzellen, PCCL-Symposium 2011 Leoben, Austria.

6.5 Curriculum vitae

Personal Details

Name	Sebastian Dunst
Address	Maiffredygasse 4/6, 8010 Graz
E-mail	dunst@gmx.at
Date of birth	25.07.1980
Citizenship	Austria

Education and Qualifications

1986-1990	Elementary school in Pressguts
1990-1998	Gymnasium in BG Gleisdorf
1998-1999	Graz University – Study of Laws (discontinued)
2000-2003	Graz University of Technology – Study of Technical Chemistry (discontinued)
2006-2008	Chemieingenieurschule Graz, Kolleg for Chemistry
2008-2010	Fresenius University of Applied Sciences Idstein (D) - Chemical Engineering, Diploma Thesis at Joanneum Research Forschungsgesellschaft mbH Weiz: 6,13-Bis(triisopropylsilyl-ethynyl)pentacene as semiconducting material in organic field effect transistors.
2010-2016	Doctoral School at Graz University of Technology (PhD supervisor: Assoc. Prof. DI Dr. Gregor Trimmel)

6.6 References

[1] International Energy Agency, Key world energy statistics 2015,

[2] International Energy Agency – Photovoltaic Power System Program, Trends 2015 in photovoltaic applications - Survey Report of Selected IEA Countries between 1992 and 2.014, Report IEA-PVPS T1-27:2015.

[3] International Energy Agency, Technology Roadmap Solar Photovoltaic Energy - 2014 edition, www.iea.org/roadmaps, 21.02.2016.

[4] W. Smith, Effect of light on selenium during the passage of an electric current, Nature 7 (1873) 303.

[5] W.G. Adams, R.E. Day, The action of light on selenium, Phil. Trans. R. Soc. Lond. 167 (1877) 313-349.

[6] C.E. Fritts, On a new form of selenium photocell, American Journal of Science 26 (1883) 465.

[7] H.R. Hertz, Über einen Einfluss des ultravioletten Lichtes auf die electrische Entladung, Annalen der Physik 267, 8 (1887) 983–1000.

[8] A.E. Becquerel, Recherches sur les effets de la radiation chimique de la lumiére solaire, au moyen des courants électriques, Compt. Rend. Acad. Sci. 9 (1839) 145–149.

[9] A. Einstein, Über einen die Erzeugung und Verwandlung des Lichtes betreffenden heuristischen Gesichtspunkt, Annalen der Physik 17 (1905) 132-148.

[10] S.J. Appleyard, Simple photovoltaic cells for exploring solar energy concepts, Phys. Educ. 41, 5 (2006) 409-419.

[11] R.S. Ohl, Light-sensitive electric device, U.S. Patent 2402662.

[12] D.M. Chapin, C.S. Fuller, G.L. Pearson, A new silicon p-n junction photocell for converting solar radiation into electrical power, J. Appl. Phys. 25 (1954) 676-677.

[13] K. Masuko, M. Shigematsu, T. Hashiguchi, D. Fujishima, M. Kai, N. Yoshimura, T. Yamaguchi, Y. Ichihashi, T. Yamanishi, T. Takahama, M. Taguchi, E. Maruyama, S. Okamoto, Achievement of more than 25% conversion efficiency with crystalline silicon heterojunction solar cell, IEEE Journal of Photovoltaics 4 (2014) 1433–1435.

[14] M.A. Green, K. Emery, Y. Hishikawa, W. Warta, E.D. Dunlop, Solar cell efficiency tables (version 47), Progress in Photovoltaics 24, 1 (2016) 3–11.

[15] R.F. Service, Outlook brightens for plastic solar cells, Science 332, 6027 (2011) 293.

[16] ZSW stellt Weltrekord-Solarzelle her - Dünnschicht-Photovoltaik überholt mit 20,8 Prozent Wirkungsgrad multikristalline Siliziumtechno (logie, http://www.zsw-bw.de/uploads/media/pi18-2013-ZSW-WeltrekordCIGS.pdf, 09.02.2016.

[17] First Solar Builds the Highest Efficiency Thin Film PV Cell on Record, http://investor.firstsolar.com/releasedetail.cfm?releaseid=864426, 09.02.2016.

[18] Leistungsstarke CIGS-Dünnschicht-Solarmodule aus der CIGSinnoline in Schwäbisch Hall, http://www.manz.com/ecomaXL/files/Manz_CIGS-Module_Broschuere_DE.pdf&download=1, 09.02.2016.

[19] First Solar Sets Thin-Film Module Efficiency World Record of 17.0 Percent, http://investor.firstsolar.com/releasedetail.cfm?ReleaseID=833971, 09.02.2016.

[20] V. Fthenakis, Sustainability of photovoltaics: The case for thin-film solar cells, IRESR 13, 9 (2009) 2746–2750.

[21] Fraunhofer Institute for Solar Energy Systems, Photovoltaics report, updated: 17. November 2015, https://www.ise.fraunhofer.de/de/downloads/pdf-files/aktuelles/photovoltaics-report-in-englischer-sprache.pdf, 23.02.2016.

[22] Fraunhofer Institute for Solar Energy Systems & National Renewable Energy Laboratory, Current status of concentrator photovoltaic (CPV) technology, https://www.ise.fraunhofer.de/de/veroeffentlichungen/veroeffentlichungen-pdf-dateien/studien-und-konzeptpapiere/current-status-of-concentrator-photovoltaic-cpv-technology-in-englischer-sprache.pdf, 03.03.2016.

[23] M.C. Scharber, N.S. Sariciftci, Efficiency of bulk-heterojunction organic solar cells, Prog. In Polymer Science 38, 12 (2013) 1929-1940.

[24] F.C. Krebs, Fabrication and processing of polymer solar cells: A review of printing and coating techniques, Sol. Energy Mat. 93 (2009) 394-412..

[25] H. Choi, J.H. Song, J. Jang, X.D. Mai, S. Kim, S. Jeong, High performance of PbSe/PbS core/shell quantum dot heterojunction solar cells: short circuit current

enhancement without the loss of open circuit voltage by shell thickness control, Nanoscale 7 (2015) 17473-17481.

[26] M.K. Nazeeruddin, E. Baranoff, M. Grätzel, Dye-sensitized solar cells: A brief overview, Solar Energy 85 (2011) 1172–1178.

[27] M.A. Green, A. Ho-Baillie, H.J. Snaith, The emergence of perovskite solar cells, Nat. Photonics 8 (2014) 506-514.

[28] N.-G. Park, Perovskite solar cells: an emerging photovoltaic technology, Materials Today 18, 2 (2015) 65-72.

[29] I. Etxebarria, J. Ajuria, R. Pacios, Solution-processable polymeric solar cells: A review on materials, strategies and cell architectures to overcome 10%, Organic Electronics 19 (2015) 34-60.

[30] H. Spanggaard, F.C. Krebs, A brief history of the development of organic and polymeric photovoltaics, Sol. Energy Mat. & Sol. Cells 83 (2004) 125-146.

[31] C.W. Tang, A.C. Albrecht, Chlorophyll-a photovoltaic cells, Nature 254 (1975) 507.

[32] C.W. Tang, Two-layer organic photovoltaic cell, Appl. Phys. Lett. 48 (1986) 183-185.

[33] N.S. Sariciftci, L. Smilowitz, A.J. Heeger, Photoinduced electron-transfer from a conducting polymer to buckminsterfullerene, Science 258 (1992) 1474-1476.

[34] G. Yu, J. Gao, J.C. Hummelen, F. Wundl, A.J. Heeger, Polymer Photovoltaic Cells: Enhanced Efficiencies via a Network of Internal Donor-Acceptor Heterojunctions, Science 270 (1995) 1789-1791.

[35] S.E. Shaheen, C.J. Brabec, N.S. Sariciftci, 2.5% efficient organic plastic solar cells, Appl. Phys. Lett. 78 (2001) 841-843.

[36] G. Li, V. Shrotriya, J. Huang, Y. Yao, T. Moriarty, K. Emery, Y. Yang, High-efficiency solution processable polymer photovoltaic cells by self-organization of polymer blends, Nature Mat. 4 (2005) 864-868.

[37] W. Ma, C. Yang, X. Gong, K. Lee, A.J. Heeger, Thermally Stable, Efficient Polymer Solar Cells with Nanoscale Control of the Interpenetrating Network Morphology, Adv. Funct. Mater. 15 (2005) 1617-1622.

[38] M. Hosoya, H. Oooka, H. Nakao, S. Mori, T. Gotanda, N. Shida, M. Saito, Y. Nakano, K. Todori, Module development for polymer solar cells, Abstract O-PV 6.2 - Grand Renewable Energy Conference (2014) 21–37.

[39] http://www.heliatek.com/de/presse/pressemitteilungen/details/neuer-weltrekord-fuer-organische-solarzellen-heliatek-behauptet-sich-mit-12-zelleffizienz-als-technologiefuehrer, 23.09.2015

[40] Z. Liu, Y. Sun, J. Yuan, H. Wie, X. Huang, L. Han, W. Wang, H. Wang, W. Ma, High-Efficiency Hybrid Solar Cells Based on Polymer/PbSxSe1-x Nanocrystals Benefiting from Vertical Phase Segregation, Adv. Mater. 25 (2013) 5772-5778.

[41] S. Ren, L.-Y. Chang, S.-K. Lim, J. Zhao, M. Smith, N. Zhao, V. Bulović, M. Bawendi, S. Gradecak, Inorganic–organic hybrid solar cell: bridging quantum dots to conjugated polymer nanowires, Nano Lett. 11 (2011) 3998–4002.

[42] S. Dowland, T. Lutz, A. Ward, S.P. King, A. Sudlow, M.S. Hill, K.C. Molloy, S.A. Haque, Direct growth of metal sulfide nanoparticle networks in solid-state polymer films for hybrid inorganic-organic solar cells, Adv. Mater. 23 (2011) 2739–2744.

[43] R. Zhou, R. Stalder, D. Xie, W. Cao, Y. Zheng, Y. Yang, M. Plaisant, P.H. Holloway, K.S. Schanze, J.R. Reynolds, J. Xue, Enhancing the Efficiency of Solution-Processed Polymer:Colloidal Nanocrystal Hybrid Photovoltaic Cells Using Ethanedithiol Treatment, ACS Nano 7 (2013) 4846-4854.

[44] K.F. Jeltsch, M. Schädel, J.-B. Bonekamp, P. Niyamakom, F. Rauscher, H.W.A. Lademann, I. Dumsch, S. Allard, U. Scherf, K. Meerholz, Efficiency Enhanced Hybrid Solar Cells Using a Blend of Quantum Dots and Nanorods, Adv. Funct. Mater. 22 (2012) 397–404.

[45] Z. Chen, H. Zhang, X. Du, X. Cheng, X. Chen, Y. Jiang, B. Yang, From planarheterojunction to n-i structure: an efficient strategy to improve short-circuit current and power conversion efficiency of aqueous-solution-processed hybrid solar cells, Energy Environ. Sci. 6 (2013) 1597–1603.

[46] N. Bansal, F.T.F. O'Mahony, T. Lutz, S.A. Haque, Solution Processed Polymer-Inorganic Semiconductor Solar Cells Employing Sb_2S_3 as a Light Harvesting and Electron Transporting Material, Adv. Energy Mater. 3 (2013) 986–990.

[47] S.D. Oosterhout, M.M. Wienk, S.S. van Bavel, R. Thiedmann, L.J.A. Koster, J. Gilot, J. Loos, V. Schmidt, R.A.J. Janssen, The effect of three-dimensional morphology on the efficiency of hybrid polymer solar cells, Nat. Mater. 8 (2009) 818–824.

[48] E. Maier, T. Rath, W. Haas, O. Werzer, R. Saf, F. Hofer, D. Meissner, O. Volobujeva, S. Bereznev, E. Mellikov, H. Amenitsch, R. Resel, G. Trimmel, $CuInS_2$–Poly(3-(ethyl-4-butanoate)thiophene) nanocomposite solar cells: Preparation by an in situ formation route, performance and stability issues, Sol. Energy Mater. Sol. Cells 95 (2011) 1354–1361.

[49] T. Rath, M. Edler, W. Haas, A. Fischereder, S. Moscher, A. Schenk, R. Trattnig, M. Sezen, G. Mauthner, A. Pein, D. Meischler, K. Bartl, R. Saf, N. Bansal, S.A. Haque, F. Hofer, E.J.W. List, G. Trimmel, A Direct Route Towards Polymer/Copper Indium Sulfide Nanocomposite Solar Cells, Adv. Energy Mater. 1 (2011) 1046-1050.

[50] H. Shirakawa, E.J. Louis, A.G. MacDiarmid, C.K. Chiang, A.J. Heeger, Synthesis of electrically conducting organic polymers: Halogen Derivatives of Polyacetylene, $(CH)_x$, J. Chem. Soc., Chem. Commun. (1977) 578-580.

[51] M. Skompska, J. Mieczkowski, R. Holze, J. Heinze, In situ conductance studies of p- and n-doping of poly(3,4-dialkoxythiophenes), Journal of Electroanalytical Chemistry 577 (2005) 9–17.

[52] S.B Darling, F. You, The case for organic photovoltaics, RCD Advances 3 (2013) 17633-17648.

[53] B.R. Saunders, Hybrid polymer/nanoparticle solar cells: Preparation, principles and challenges J. Coll. Interf. Sci. 369 (2012) 1-15.

[54] V.D. Mihailetchi, L.J.A. Koster, P.W.M. Blom, Photocurrent Generation in Polymer-Fullerene Bulk Heterojunctions, Applied Physics Letters 85 (2004) 970–972.

[55] T. Rath, G. Trimmel, In situ syntheses of semiconducting nanoparticles in conjugated polymer matrices and their application in photovoltaics, Hybrid Mater. 1 (2014) 15-36.

[56] H. Hoppe, M. Niggemann, C. Winder, J. Kraut, R. Hiesgen, A. Hinsch, D. Meissner, N.S. Sariciftci, Nanoscale Morphology of Conjugated Polymer/Fullerene-Based Bulk-Heterojunction Solar Cells, Adv. Funct. Mater. 14, 10 (2004) 1005-1011.

[57] H. Hoppe, N.S. Sariciftci, Morphology of polymer/fullerene bulk heterojunction solar cells, J. Mater. Chem. 16 (2006) 45-61.

[58] J.M. Nunzi, Organic photovoltaic materials and devices, C.R. Physique 3 (2002) 523-542.

[59] B.R. Saunders, M.L. Turner, Nanoparticle–polymer photovoltaic cells, Advances in Colloid and Interface Science 138 (2008) 1–23.

[60] C. Gueymard, D. Myers, K. Emery, Proposed reference irradiance spectra for solar energy systems testing, Solar Energy 73, 6 (2002) 443–467.

[61] ASTM G173-03(2012), Standard tables for reference solar spectral irradiances: Direct normal and hemispherical on 37° tilted surface, ASTM International, West Conshohocken, PA, 2012, www.astm.org, 23.02.2016.

[62] M. Helgesen, R. Søndergaard, F.C. Krebs, Advanced materials and processes for polymer solar cell devices, J. Mater. Chem. 20 (2010) 36–60.

[63] O. Haillant, Accelerated weathering testing principles to estimate the service life of organic PV modules, Sol. Energy Mat. & Sol. Cells 95 (2011) 1284-1292.

[64] S. Schuller, P. Schilinsky, J. Hauch, C.J. Brabec, Determination of the degradation constant of bulk heterojunction solar cells by accelerated lifetime measurements, Appl. Phys. A (2004) 37-40.

[65] F.J. Pern, S.H. Glick, Photothermal stability of encapsulated Si solar cells and encapsulation materials upon accelerated exposures, Sol. Energy Mat. Sol Cells 61 (2000) 153-188.

[66] M. Jorgesen, K. Norrman, S.A. Gevorgyan, T. Tromholt, B. Andreasen, F.C. Krebs, Stability of polymer solar cells, Adv. Mater. 24 (2012) 580-612.

[67] E.L. Meyer, E.E. van Dyk, Characterization of degradation in thin-film photovoltaic module performance parameters, Renewable Energy 28 (2003) 1455–1469.

[68] K.W. Jansen, A.E. Delahoy, A laboratory technique for the evaluation of electrochemical transparent conductive oxide delamination from glass substrates, Thin Solid Films 423 (2003) 153–160.

[69] T.J. McMahon, Accelerated testing and failure of thin-film PV modules, Prog. Photovolt. 12 (2004) 235–248.

[70] D.L. Staebler, C.R. Wronski, Reversible conductivity changes in discharge-produced amorphous Si, Appl. Phys. Let. 31 (1977) 292-294.

[71] M. Jorgesen, K. Norrman, S.A. Gevorgyan, T. Tromholt, B. Andreasen, F.C. Krebs, Stability of polymer solar cells, Adv. Mater. 24 (2012) 580-612.

[72] M.O. Reese, S.A. Gevorgyan, M. Jørgensen, E. Bundgaard, S.R. Kurtz , D.S. Ginley , D.C. Olson, M.T. Lloyd , P. Morvillo, E.A. Katz, A. Elschner, O. Haillant, T.R. Currier, V. Shrotriya, M. Hermenau, M. Riede, K.R. Kirov, G. Trimmel, T. Rath, O. Inganas, F. Zhang, M. Andersson, K. Tvingstedt, M. Lira-Cantu, D. Laird, C. McGuiness, S.(J.) Gowrisanker, M. Pannone, M. Xiao, J. Hauch, R. Steim, D.M. DeLongchamp, R. Rösch, H. Hoppe, N. Espinosa, A. Urbina, G. Yaman-Uzunoglu, J.-B. Bonekamp, A.J.J.M. van Breemen, C. Girotto, E. Voroshazi, F.C. Krebs, Consensus stability testing protocols for organic photovoltaic materials and devices, Sol. Energy Mater. Sol. Cells 95 (2011) 1253-1267.

[73] C.H. Peters, I.T. Sachs-Quintana, J.P. Kastrop, S. Beaupré, M. Leclerc, M.D. McGehee, High efficiency polymer solar cells with long operating lifetimes, Adv. Energy Mater. 1 (2011) 491–494.

[74] F.C. Krebs, S.A. Gevorgyan, B. Gholamkhass, S. Holdcroft, C. Schlenker, M.E. Thompson, B.C. Thompson, D. Olson, D.S. Ginley, S.E. Shaheen, H.N. Alshareef, J.W. Murphy, W.J. Youngblood, N.C. Heston, J.R. Reynolds, S. Jia, D. Laird, S.M. Tuladhar, J.G.A. Dane, P. Atienzar, J. Nelson, J.M. Kroon, M.M. Wienk, R.A.J. Janssen, K. Tvingstedt, F. Zhang, M. Andersson, O. Inganäs, M. Lira-Cantu, R. de Bettignies, S. Guillerez, T. Aernouts, D. Cheyns, L. Lutsen, B. Zimmermann, U. Würfel, M. Niggemann, H.-F. Schleiermacher, P. Liska, M. Grätzel, P. Lianos, E.A. Katz, W. Lohwasser, B. Jannon, A round robin study of flexible large-area roll-to-roll processed polymer solar cell modules, Sol. Energy Mater. Sol. Cells 93 (2009) 1968–1977.

[75] S.A. Gevorgyan, A.J. Medford, E. Bundgaard, S.B. Sapkota, H. Schleiermacher, B. Zimmermann, U. Würfel, A. Chafiq, M. Lira-Cantu, T. Swonke, M. Wagner, C.J. Brabec, O. Haillant, E. Voroshazi, T. Aernouts, R. Steim, J.A. Hauch, A. Elschner, M.

Pannone, M. Xiao, A. Langzettel, D. Laird, M.T. Lloyd, T. Rath, E. Maier, G. Trimmel, M. Hermenau, T. Menke, K. Leo, R. Rösch, M. Seeland, H. Hoppe, T.J. Nagle, K.B. Burke, C.J. Fell, D. Vak, T. B. Singh, S.E. Watkins, Y. Galagan, A. Manor, E.A. Katz, T. Kim, K. Kim P.M. Sommeling, W.J.H. Verhees, S.C. Veenstra, M. Riede, G.M. Christoforo, T. Currier, V. Shrotriya, G. Schwartz, F.C. Krebs, An inter-laboratory stability study of roll-to-roll coated flexible polymer solar modules, Sol. Energy Mater. Sol. Cells 95 (2011) 1398-1416.

[76] M.V. Madsen, S.A.Gevorgyan, R. Pacios, J. Ajuria, I. Etxebarria, J. Kettle, N.D. Bristow, M. Neophytou, S.A. Choulis, L. Stolz Roman, T. Yohannes, A. Cester, P. Cheng, X. Zhan, J. Wu, Z. Xie, W.-C. Tu, J.-H. He, C.J. Fell, K. Anderson, M. Hermenau, D. Bartesaghi, L.J.A. Koster, F. Machui, I. González-Valls, M. Lira-Cantu, P.P. Khlyabich, B.C. Thompson, R. Gupta, K. Shanmugam, G.U. Kulkarni, Y. Galagan, A. Urbina, J. Abad, R. Roesch, H. Hoppe, P. Morvillo, E. Bobeico, E. Panaitescu, L. Menon, Q. Luo, Z. Wu, C. Ma, A. Hambarian, V. Melikyan, M. Hambsch, P.L. Burn, P. Meredith, T. Rath, S. Dunst, G. Trimmel, G. Bardizza, H. Müllejans, A.E. Goryachev, R.K. Misra, E.A. Katz, K. Takagi, S. Magaino, H. Saito, D. Aoki, P. M. Sommeling, J.M. Kroon, Tim Vangerven, J. Manca, J. Kesters, W. Maes, O.D. Bobkova, V.A. Trukhanov, D.Y. Paraschuk, F.A. Castro, J. Blakesley, S.M. Tuladhar, J.A. Röhr, J. Nelson, J. Xia, E.A. Parlak, T.A. Tumay, H.-J. Egelhaaf, D.M. Tanenbaum, G.M. Ferguson, R. Carpenter, H. Chen, B. Zimmermann, L. Hirsch, G. Wantz, Z. Sun, P. Singh, C. Bapat, T. Offermans, F.C.Krebs, Worldwide outdoor round robin study of organic photovoltaic devices and modules, Sol. Energy Mater. Sol. Cells 130 (2014) 281–290.

[77] L. Qian, J. Yang, R. Zhou, A. Tang, Y. Zheng, T.-K. Tseng, D. Bera, J. Xue, P.H. Holloway, Hybrid polymer-CdSe solar cells with a ZnO nanoparticles buffer layer for improved efficiency and lifetime, J. Mater. Chem. 21 (2011) 3814-3817.

[78] R. Zhou, Y. Zheng, L. Qian, Y. Yang, P.H. Holloway, J. Xue, Solution-processed, nanostructured hybrid solar cells with broad spectral sensitivity and stability, Nanoscale 4 (2012) 3507-3514.

[79] J. Yang, A. Tang, R. Zhou, J. Xue, Effects of nanocrystal size and device aging on performance of hybrid poly(3-hexylthiophen):CdSe nanocrystal solar cells, Sol. Energy Mater. Sol. Cells 95 (2011) 476-482.

[80] E. Maier, T. Rath, W. Haas, O. Werzer, R. Saf, F. Hofer, D. Meissner, O. Volobujeva, S. Bereznev, E. Mellikov, H. Amenitsch, R. Resel, G. Trimmel, $CuInS_2$–Poly(3-(ethyl-4-butanoate)thiophene) nanocomposite solar cells: Preparation by an in situ formation route, performance and stability issues, Sol. Energy Mater. Sol. Cells 95 (2011) 1354–1361.

[81] S. Kwon, K.-G. Lim, M. Shim, H.C. Moon, J. Park, G. Jeon, J. Shin, K. Cho, T. Lee, J.K. Kim, Air-stable inverted structure of hybrid solar cells using a cesium-doped ZnO electron transport layer prepared by a sol–gel process, J. Mater. Chem. A 1 (2013) 11802-11808.

[82] B. Reeja-Jayan, A. Manthiram, Understanding the improved stability of hybrid polymer solar cells fabricated with copper electrodes, ACS Appl. Mater. Interfaces 3 (2011) 1492-1501.

[83] J. Wu, G. Yue, Y. Xiao, J. Lin, M. Huang, Z. Lan, Q. Tang, Y. Huang, L. Fan, S. Yin, S. Tsugio, An ultraviolet responsive hybrid solar cell based on titania/poly(3-hexylthiophene), Sci. Rep. 3 (2013) 1283.

[84] E. Arici, H. Hoppe, F. Schäffler, D. Meissner, M.A. Malik, N.S. Sariciftci, Hybrid solar cells based on inorganic nanoclusters and conjugated polymers, Thin Solid Films 451–452 (2004) 612–618.

[85] E. Maier, A. Fischereder, W. Haas, G. Mauthner, J. Albering, T. Rath, F. Hofer, E.J.W. List, G. Trimmel, Metal sulfide–polymer nanocomposite thin films prepared by a direct formation route for photovoltaic applications, Thin Solid Films 519 (2011) 4201–4206.

[86] A. Schenk, Novel metal-xanthates for preparation of metal sulphides for photovoltaic applications, Graz University of Technology (2011).

[87] B. Stickler, Theoretical investigation of the competition between electron-hole generation and recombination effects in organic and organic-inorganic solar cells, Graz University of Technology (2009).

[88] M. Gruber, Simulation of the charge carrier transport in organic semiconductor devices, University of Technology (2012).

[89] A. Fischereder, Synthesis and characterization of metal sulfides for photovoltaic applications, Graz University of Technology (2011).

[90] M. Edler, Preparation and characterization of nanostructured solar energy materials and nanocomposite solar cells, Graz University of Technology (2011).

[91] A. Pein, Synthesis and characterization of materials for optoelectronic devices, Graz University of Technology (2011).

[92] M. Arar, Investigations on morphology and electrode modification in organic/inorganic hybrid solar cells, Graz University of Technology (2013).

[93] C. Fradler, Strategies to improve the efficiency of hybrid solar cells, Graz University of Technology (2014).

[94] V. Kaltenhauser, In situ synthesis of metal sulphide / polymer nanocomposites in single junction and tandem solar cells, Graz University of Technology (2013).

[95] W. Haas, Morphology control of high-performance polymer solar cells, Graz University of Technology (2013).

[96] E. Maier, Development and optimization of organic-inorganic hybrid nanocomposite solar cells, Graz University of Technology (2010).

[97] M. Arar, A. Pein, W. Haas, F. Hofer, K. Norrman, F.C. Krebs, T. Rath, G. Trimmel, Comprehensive Investigation of Silver Nanoparticle/Aluminum Electrodes for Copper Indium Sulfide/Polymer Hybrid Solar Cells, J. Phys. Chem. C 116 (2012) 19191-19196.

[98] V. Kaltenhauser, T. Rath, M. Edler, A. Reichmann, G. Trimmel, Exploring polymer/nanoparticle hybrid solar cells in tandem architecture, RSC Adv. 3 (2013) 18643 18650.

[99] C. Fradler, T. Rath, S. Dunst, I. Letofsky-Papst, R. Saf, B. Kunert, F. Hofer, R. Resel, G. Trimmel, Flexible polymer/copper indium sulfide hybrid solar cells and modules based on the metal xanthate route and low temperature annealing, Sol. Energy Mater. Sol. Cells 124 (2014) 117-125.

[100] S.A. Gevorgyan, M.V. Madsen, B. Roth, M. Corazza, M. Hösel, R.R. Søndergaard, M. Jørgensen, F.C. Krebs, Lifetime of organic photovoltaics: Status and predictions, Adv. Energy Mater. 6 (2016) 150120801-150120817.

[101] H.M. Lemire, K.A. Peterson, S. Sprawls, K. Singer, I.T. Martin, R.H. French, Degradation of transparent conductive oxides: Mechanistic insights across configurations and exposures, Proc. SPIE, Reliability of Photovoltaic Cells, Modules, Components, and Systems 6 (2013) 882502-882510.

[102] G.-F. Wang, X.-M. Tao, R.-X. Wang, Flexible organic light-emitting diodes with a polymeric nanocomposite anode, Nanotechnologies 19 (2008) 1452011-1452015.

[103] B. Ecker , J.C. Nolasco, J. Pallarés, L.F. Marsal, J. Posdorfer, J. Parisi, E. von Hauff, Degradation effects related to the hole transport layer in organic solar cells, Adv. Funct. Mater. 21 (2011) 2705–2711.

[104] A.M. Nardes, M. Kemerink, M.M. de Kok, E. Vinken, K. Maturova, R.A.J. Janssen, Conductivity, work function, and environmental stability of PEDOT:PSS thin films treated with sorbitol, Organic Electronics 9 (2008) 727–734.

[105] E. Voroshazi, B. Verreet, A. Buri, R. Müller, D. Di Nuzzo, P. Heremans, Influence of cathode oxidation via the hole extraction layer in polymer:fullerene solar cells, Organic Electronics 12 (2011) 736–744.

[106] M.P. de Jong, L.J. van Ijzendoorn, M.J.A. de Voigt, Stability of the interface between indium-tin-oxide and poly(3,4-ethylenedioxythiophene)/poly(styrenesulfonate) in polymer light-emitting diodes, Appl. Phys. Lett. 77 (2000) 2255-2257.

[107] F.C. Krebs, K. Norrman, Analysis of the failure mechanism for a stable organic photovoltaic during 10 000 h of testing, Prog. Photovol. Res. Appl. 15 (2007) 697-712.

[108] S. Wu, S. Han, Y. Zheng, H. Zheng, N. Liu, L. Wang, Y. Cao, J. Wang, pH-neutral PEDOT:PSS as hole injection layer in polymer light emitting diodes, Organic Electronics 12 (2011) 504–508.

[109] M.G. Varnamkhasti, H.R. Fallah, M. Mostajaboddavati, R. Ghasemi, A. Hassanzadeh, Comparison of metal oxides as anode buffer layer for small molecule organic photovoltaic cells, Sol. Energy Mat. & Sol. Cells 98 (2012) 379–384.

[110] V. Shrotriya, G. Li, Y. Yao, C.-W. Chu, Y. Yang, Transition metal oxides as the buffer layer for polymer photovoltaic cells, Appl. Phys. Lett. 88 (2008) 073508.

[111] K. Norrman, M.V. Madsen, S.A. Gevorgyan, and F. C. Krebs, Degradation patterns in water and oxygen of an inverted polymer solar cell, J. Am. Chem. Soc. 132 (2010) 16883-16892.

[112] N. Grossiord, J.M. Kroon, R. Andriessen, P.W.M. Blom, Degradation mechanisms in organic photovoltaic devices, Organic Electronics 13 (2012) 432–456.

[113] H. Hintz, H.-J. Egelhaaf, L. Lüer, J. Hauch, H. Peisert, T. Chass, Photodegradation of P3HT - A systematic study of environmental factors, Chem. Mater. 23 (2011) 145–154.

[114] J. Razzell-Hollis, J. Wade, W.C. Tsoi, Y. Soon, J. Durrant, J.-S. Kim, Photochemical stability of high efficiency PTB7:PC70BM solar cell blends, J. Mater. Chem. A 2 (2014) 20189–20195.

[115] Wang, N.; Tong, X.; Burlingame, Q.; Yu, J.; Forrest, S.R. Photodegradation of small-molecule organic photovoltaics, Sol. Energy Mat. 125 (2014) 170-175.

[116] M.S.A. Abdou, F.P. Orfino, Y. Son, S. Holdcroft, Interaction of Oxygen with Conjugated Polymers: Charge Transfer Complex Formation with Poly(3-alkylthiophenes), J. Am. Chem. Soc. 119 (1997) 4518-4524.

[117] J. Schafferhans, A. Baumann, A. Wagenpfahl, C. Deibel, V. Dyakonov, Oxygen doping of P3HT:PCBM blends: influence on trap states, charge carrier mobility and solar cell performance, Org. Electronics 11 (2010) 1693–1700.

[118] A. Aguirre, S.C.J. Meskers, R.A.J. Janssen, H.-J. Egelhaaf, Formation of metastable charges as a first step in photoinduced degradation in π-conjugated polymer:fullerene blends for photovoltaic applications, Organic Electronics 12 (2011) 1657–1662.

[119] M.G. Matturro, R.P. Reynolds, R.V. Kastrup, C.F. Pictroski, Thioozonide decomposition. Sulfur and oxygen atom transfer. Evidence for the formation of a carbonyl O-sulfide intermediate, J. Am. Chem. Soc. 108 (1986) 2775-2776.

[120] T. Konishi, M. Fujitsuka, O. Ito, Evaluation of rate constant for electron transfer from C60-anion radical to molecular oxygen by laser flash photolysis method, Chem. Lett. 29 (2000) 202-203.

[121] G. Dennler, C. Lungenschmied, H. Neugebauer, N.S. Sariciftci, M. Latreche, G. Czeremuszkin, M.R. Wertheimer, A new encapsulation solution for flexible organic solar cells, Thin Solid Films 511 (2006) 349 – 353.

[122] M. Manceau, E. Bundgaard, J.E. Carlé, O. Hagemann, M. Helgesen, R. Søndergaard, M. Jørgensen, F.C. Krebs, Photochemical stability of π-conjugated polymers for polymer solar cells: a rule of thumb, J. Mater. Chem. 21 (2011) 4132-4141.

[123] J. Kesters, P. Verstappen, J. Raymakers, W. Vanormelingen, J. Drijkoningen, J. D'Haen, J. Manca, L. Lutsen, D. Vanderzande, W. Maes, Enhanced organic solar cell stability by polymer (PCPDTBT) side chain functionalization, Chem. Mater. 27 (2015) 1332−1341.

[124] M. Manceau, M. Helgesen, F.C. Krebs, Thermo-cleavable polymers: materials with enhanced photochemical stability, Polym. Degrad. Stab. 95 (2010) 2666–2669.

[125] M. Manceau, A. Rivaton, J.-L. Gardette, S. Guillerez, N. Lemaitre, The mechanism of photo- and thermooxidation of poly(3-hexylthiophene) (P3HT) reconsidered, Polymer Degradation and Stability 94 (2009) 898–907.

[126] D. He, X. Du, W. Zhang, Z. Xiao, L. Ding, Improving the stability of P3HT/PC61BM solar cells by a thermal crosslinker J. Mater. Chem. A 1 (2013) 4589–4594.

[127] J.C. Hummelen, J. Knol, L. Sánchez, Stability issues of conjugated polymer/fullerene solar cells from a chemical viewpoint, Proc. of SPIE 4108 (2001) 76-87.

[128] M. Hermenau, M. Riede, K. Leo, S.A. Gevorgyan, F.C. Krebs, K. Norrman, Water and oxygen induced degradation of small molecule organic solar cells, Sol. Energy Mat. Sol. Cells 95 (2011) 1268–1277.

[129] C.X. Zhao, L.L. Deng, M.Y. Ma, J.R. Kish, G. Xu, Multiple-interface tracking of degradation process in organic photovoltaics, AIP ADVANCES 3 (2013) 1021211-1021217.

[130] M. Lögdlund, J.L. Bredas, Theoretical studies of the interaction between aluminum and poly(p-phenylenevinylene) and derivatives, J. Chem. Phys. 101 (1994) 4357-4364.

[131] M. Jørgensen, K. Norrman, F.C. Krebs, Stability/degradation of polymer solar cells, Sol. Energy Mater. Sol. Cells 92 (2008) 686-714.

[132] F.C. Krebs, J.E. Carlé, N. Cruys-Bagger, M. Andersen, M.R. Lilliedal, M.A. Hammond, S. Hvidt, Lifetimes of organic photovoltaics: photochemistry, atmosphere effects and barrier layers in ITO-MEHPPV:PCBM-aluminium devices, Sol. Energy Mat. Sol. Cells 86 (2005) 499–516.

[133] W.M Haynes, CRC Handbook of Chemistry and Physics: A ready-reference book of chemical and physical data, CRC Press (2009).

[134] S. van Reenen, S. Kouijzer, R.A.J. Janssen, M.M. Wienk, M. Kemerink, Origin of work function modification by ionic and amine-based interface layers, Adv. Mat. Interfaces 8, 1 (2014) 14001891-140018911.

[135] K.A. Nagamatsu, S. Avasthi, J. Jhaveri, J.C. Sturm, A 12% efficient silicon/PEDOT:PSS heterojunction solar cell fabricated at <100°C, IEEE J. of Photovolt. 4, 1 (2014) 260-264.

[136] E. Wang, L. Wang, L. Lan, C. Luo, W. Zhuang, J. Peng, Y. Cao, High-performance polymer heterojunction solar cells of a polysilafluorene derivative, Appl. Phys. Lett. 92 (2008) 0333071-0333073.

[137] E. Arici, N.S. Sariciftci, D. Meissner, Hybrid Solar Cells Based on Nanoparticles of $CuInS_2$ in Organic Matrices, Adv. Funct. Mater. 13 (2003) 165–171.

[138] P.-R. Huang, Y. He, C. Cao, Z.-H. Lu, The origin of the high work function of chlorinated indium tin oxide, NPG Asia Materials 5 (2013) 1-5.

[139] M.A.M. Hassan, I.R. Agool, L.M. Raoof, Silver oxide nanostructure prepared on porous silicon for optoelectronic application, Appl. Nanosci. 4 (2014) 429–447.

[140] C.-W. Chen, P.-Y. Hsieh, H.-H. Chiang, C.-L. Lin, H.-M. Wu, C.-C. Wu, Top-emitting organic light-emitting devices using surface-modified Ag anode, Appl. Phys. Lett. 83, 25 (2003) 5127-5129.

[141] M.T. Lloyd, D.C. Olson, P. Lu, E. Fang, D.L. Moore, M.S. White, M.O. Reese, D.S. Ginley, J.W.P. Hsu, Impact of contact evolution on the shelf life of organic solar cells, J. Mater. Chem. 19 (2009) 7638–7642.

[142] A. Lachkar, A. Selmani, E. Sacher, M. Leclerc, R. Mokhliss, Metallization of polythiophenes I. Interaction of vapour-deposited Cu, Ag and Au with poly(3-hexylthiophene) (P3HT), Synth. Met. 66 (1994) 209–215.

[143] R. Roesch, K.-R. Eberhardt, S. Engmann, G. Gobsch, H. Hoppe, Polymer solar cells with enhanced lifetime by improved electrode stability and sealing, Sol. Energy Mater. Sol. Cells 117 (2013) 59-66.

[144] M. Jäger, R. Trattnig, M. Postl, W. Haas, B. Kunert, R. Resel, F. Hofer, A. Klug, G. Trimmel, E.J.W. List, Influence of the bridging atom in fluorene analogue low-bandgap polymers on photophysical and morphological properties of copper indium sulfide/polymer nanocomposite solar cells, J. Polym. Sci. Part B Polym. Phys. 51 (2013) 1400–1410.

[145] N. Blouin, A. Michaud, D. Gendron, S. Wakim, E. Blair, R. Neagu-Plesu, M. Belletete, G. Durocher, Y. Tao and M. Leclerc, Toward a rational design of poly(2,7-carbazole) derivatives for solar cells, J. Am. Chem. Soc. 130 (2008) 732-742.

[146] J. C. Bijleveld, M. Shahid, J. Gilot, M.M. Wienk, R.A.J. Janssen, Copolymers of cyclopentadithiophene and electron-deficient aromatic units designed for photovoltaic applications, Adv. Funct. Mater. 19 (2009) 3262–3270.

[147] F.C. Krebs, Encapsulation of polymer photovoltaic prototypes, Sol. Energy Mat. & Sol. Cells 90 (2006) 3633-3643.

[148] J. Lewis, M. Weaver, Thin film permeation barrier technology for flexible organic light emitting device, IEEE J. Selec. Topics. Quantum Elect. 10 (2004) 45-57.

[149] C. Lungenschmied, G. Dennler, G. Czeremuszkin, M. Latreche, H. Neugebauer, N.S. Sariciftci, Flexible encapsulation for organic solar cells**,** Proc. of SPIE 6197 (2006) 121-128.

[150] S. Cros, R. de Bettignies, S. Berson, S. Bailly, P. Maisse, N. Lemaitre, S. Guillerez, Definition of encapsulation barrier requirements: A method applied to organic solar cells, Sol. Energy Mat. & Sol. Cells 95 (2011) S65–S69.

[151] M. Corazza, F.C. Krebs, S.A. Gevorgyan, Predicting, categorizing and intercomparing the lifetime of OPVs for different ageing tests, Sol. Energy Mat. & Solar Cells 130 (2014) 99-106.

[152] R. De Bettignies, J. Leroy, M. Firon, C. Sentein, Accelerated lifetime measurements of P3HT:PCBM solar cells, Synth. Metals 156 (2006) 510-513.

[153] S.A. Gevorgyan, M. Jorgesen, F.C Krebs, A setup for studying stability and degradation of polymer solar cells, Sol. Energy Mat. & Sol. Cells 92 (2008) 736-745.

[154] I. Visoly-Fisher, A. Mescheloff, M. Gabay, C. Bounioux, L. Zeiri, M. Sansotera, A.E. Goryachev, A. Braun, Y. Galagan, E.A. Katz, Concentrated sunlight for accelerated stability testing of organic photovoltaic materials: Towards decoupling light intensity and temperature, Sol. Energy Mater. Sol. Cells 134 (2015) 99–107.

[155] G. Bardizza, A. Loi, H. Müllejans, T. Sample, E. Dunlop, Accelerated ageing test of organic photovoltaic mini-modules: Study of the electrical performances after exposure at different humidity, irradiance and temperature conditions, EU PVSEC Hamburg (2015) conference paper.

[156] R. Steim, F.R. Kogler, C.J. Brabec, Interface materials for organic solar cells, J. Mater. Chem. 20 (2010) 2499–2512.

[157] T.-H. Lai, S.-W. Tsang, J.R. Manders, S. Chen, F. So, Properties of interlayer for organic photovoltaics, Materials Today 16 (2013) 424-432.

[158] K. Lee, J.Y. Kim, S.H. Park, S.H. Kim, S. Cho, A.J. Heeger, Air-stable polymer electronic devices, Adv. Mater. 19 (2007) 2445-2449.

[159] S.K. Hau, H.-L. Yip, N.S. Baek, J. Zou, K. O'Malley, A.K. Jen, Air-stable inverted flexible polymer solar cells using zinc oxide nanoparticles as an electron selective layer, Appl. Phys. Lett. 92 (2005) 2533011-253303.

[160] M. Wang, F. Xie, W. Xie, S. Zheng, N. Ke, J. Chen, N. Zhao, J.B. Xu, Device lifetime improvement of polymer-based bulk heterojunction solar cells by incorporating copper oxide layer at Al cathode, Appl. Phys. Lett. 98 (2011) 183304.

[161] M. Wang, Q. Tang, J. An, F. Xie, J. Chen, S. Zheng, K.Y. Wong, Q. Miao, J. Xu, Performance and stability improvement of P3HT:PCBM-based solar cells by thermally evaporated chromium oxide (CrO_x) interfacial layer, ACS Appl. Mater. Interfaces 2 (2010) 2699-2702.

[162] M. Wang, F. Xie, J. Dua, Q. Tang, S. Zheng, Q. Miao, J. Chen, N. Zhao, J.B. Xu, Degradation mechanism of organic solar cells with aluminum cathode, Sol. Energy Mat. & Sol. Cells 95 (2011) 3303–3310.

[163] J. Luo, L. Xiao, Z. Chen, B. Qu, Q. Gong, Insulator MnO: Highly efficient and air-stable n-type doping layer for organic photovoltaic cells, Organic Electronics 11 (2010) 664–669.

[164] H. Cao, H. Takezoe, K. Ishikawa, Titanium-aluminum bilayer cathode for small-molecular organic solar cells with prolonged life upon exposure to air, Jpn. J. Appl. Phys. 52 (2013) 040202.

[165] B. Zimmermann, U. Würfel, M. Niggemann, Longterm stability of efficient inverted P3HT:PCBM solar cells, Sol. Energy Mat. Sol. Cells 93 (2009) 491–496.

[166] C.K. Chan, W. Zhao, A. Kahn, I.G. Hill, Influence of chemical doping on the performance of organic photovoltaic cells, Appl. Phys. Lett. 94 (2009) 2033061-2033063.

[167] M. Tavakkoli, R. Ajeian, M.N. Badrabadi, S.S. Ardestani, S.M.H. Feiz, K.E. Nasab, Progress in stability of organic solar cells exposed to air, Sol. Energy Mat. & Sol. Cells 95 (2011) 1964–1969.

[168] N. Wang, J. Yu, Y. Zang, J. Huang, Y. Jiang, Effect of buffer layers on the performance of organic photovoltaic cells based on copper phthalocyanine and C60, Sol. Energy Mat. & Sol. Cells 94 (2010) 263–266.

[169] F.-C. Chen, J.-L. Wu, S.S. Yang, K.-H. Hsieh, W.-C. Chen, Cesium carbonate as functional interlayer for polymer photovoltaic devices, J. Appl. Phys. 103 (2008) 1037211-1037215.

[170] G. Li, C.-W. Chu, V. Shrotriya, J. Huang, Y. Yang, Efficient inverted polymer solar cells, Appl. Phys. Lett. 88 (2006) 2535031- 2535033.

[171] J. Huang, G. Li, Y. Yang, A semi-transparent plastic solar cell fabricated by a lamination process, Adv. Mater. 20 (2008) 415–419.

[172] L. Yang, H. Xu, H. Tian, S. Yin, F. Zhang, Effect of cathode buffer layer on the stability of polymer bulk heterojunction solar cells, Sol. Energy Mater. Sol. Cells 94 (2010) 1831–1834.

[173] T. Hasegawa, S. Miura, T. Moriyama, T. Kimura, I. Takaya, Y. Osato, H. Mizutani, Novel electron-injection layers for top-emission OLEDs, Dig. Tech. Papers - Soc. Inf. Disp. Int. Symp. 35 (2004) 154-157.

[174] Y. Cai, H.X. Wei, J. Li, Q.Y. Bao, X. Zhao, S T. Lee, Y.Q. Li, J.X. Tang, Mechanism of Cs2CO3 as an n-type dopant in organic electron-transport film, Appl. Phys. Lett. 98 (2011) 1133041-1133043.

[175] S.Y. Chen, T.Y. Chu, J.F. Chen, C.Y. Su, C.H. Chen, Stable inverted bottom-emitting organic electroluminescent devices with molecular doping and morphology improvement, Appl. Phys. Lett. 89 (2006) 0535181-0535183.

[176] J. Huang, Z. Xu, Y. Yang, Low-work-function surface formed by solution-processed and thermally deposited nanoscale layers of cesium carbonate, Adv. Funct. Mater. 17 (2007) 1966–1973.

[177] M. Rusu, S. Wiesner, I. Lauermann, C.-H. Fischer, K. Fostiropoulos, J N. Audinot, Y. Fleming, M.C. Lux-Steiner, Formation of charge-selective Mg–Ag electrodes to CuPc:C60 blend layers, Appl. Phys. Lett. 97 (2010) 0735041-0735043.

[178] M.C.G. Passeggi Jr., L.I. Vergara, S.M. Mendoza, J. Ferron, Passivation and temperature effects on the oxidation process of titanium thin films, Surface Science 507–510 (2002) 825–831.

[179] Y. Xu, M.A.A. Schoonen, The absolute energy positions of conduction and valence bands of selected semiconducting minerals, American Mineralogist 85 (2000) 543–556.

[180] G. Li, R. Zhu, Y. Yang, Polymer solar cells, Nat. Photonics 6 (2012) 153-161.

[181] M.A. Green, K. Emery, Y. Hishikawa, W. Warta, E.D. Dunlop, Solar cell efficiency tables (version 43), Prog. Photovolt. Res. Appl. 22 (2014) 1-9.

[182] F. Gao, S. Ren, J. Wang, The renaissance of hybrid solar cells: progresses, challenges, and perspectives, Energy Environ. Sci. 6 (2013) 2020-2040.

[183] Y. Zhou, M. Eck, M. Krüger, Bulk-heterojunction hybrid solar cells based on colloidal nanocrystals and conjugated polymers, Energy Environ. Sci. 3 (2010) 1851-1864.

[184] P. Reiss, E. Couderc, J. De Girolamo, A. Pron, Conjugated polymers/semiconductor nanocrystals hybrid materials-preparation, electrical transport properties and applications, Nanoscale 3 (2011) 446-489.

[185] M. Wright, A. Uddin, Organic-inorganic hybrid solar cells: A comparative review, Sol. Energy Mater. Sol. Cells. 107 (2012) 87-111.

[186] E. Martínez-Ferrero, J. Albero, E. Palomares, Materials, nanomorphology and interfacial charge transfer reactions in quantum dot/polymer solar cell devices, J. Phys. Chem. Lett. 1 (2010) 3039-3045.

[187] A.J. Moulé, L. Chang, C. Thambidurai, R. Vidu, P. Stroeve, Hybrid solar cells: basic principles and the role of ligands, J. Mater. Chem. 22 (2012) 2351-2368.

[188] H. Yip, K. Jen, Recent advances in solution-processed interfacial materials for efficient and stable polymer solar cells, Energy Environ. Sci. 5 (2012) 5994-6011.

[189] J.Y. Kim, S.H. Kim, H.-H. Lee, K. Lee, W. Ma, X. Gong, A.J. Heeger, New architecture for high-efficiency polymer photovoltaic cells using solution-based titanium oxide as an optical spacer, Adv. Mater. 18 (2006) 572-576.

[190] J. Li, S. Kim, S. Edington, J. Nedy, S. Cho, K. Lee, A.J. Heeger, M.C. Gupta, J.T. Yates, A study of stabilization of P3HT/PCBM organic solar cells by photochemical active TiO_x layer, Sol. Energy Mater. Sol. Cells 95 (2011) 1123-1130.

[191] A. Hayakawa, O. Yoshikawa, T. Fujieda, K. Uehara, S. Yoshikawa, High performance polythiophene/fullerene bulk-heterojunction solar cell with a TiO_x hole blocking layer, Appl. Phys. Lett. 90 (2007) 163517.

[192] A. Roy, S.H. Park, S. Cowan, M.H. Tong, S. Cho, K. Lee, A.J. Heeger, Titanium suboxide as an optical spacer in polymer solar cells, Appl. Phys. Lett. 95 (2009) 013302.

[193] X. Guo, F. Liu, B. Meng, Z. Xie, L. Wang, Efficient tandem polymer photovoltaic cells using inorganic metal oxides as a transparent middle connection unit, Org. Electron. 11 (2010) 1230-1233.

[194] T. Salim, Z. Yin, S. Sun, X. Huang, H. Zhang, Y.M. Lam, Solution-processed nanocrystalline TiO_2 buffer layer used for improving the performance of organic photovoltaics, ACS Appl. Mater. Interfaces 3 (2011) 1063-1067.

[195] G.D. Sharma, M.L. Keshtov, A.R. Khokhlov, D. Tasis, C. Galiotis, Improved power conversion efficiency by insertion of RGO–TiO_2 composite layer as optical spacer in polymer bulk heterojunction solar cells, Org. Electron. 15 (2013) 348-355.

[196] S.H. Jin, G.H. Jun, S.H. Hong, S. Jeon, Conformal coating of titanium suboxide on carbon nanotube networks by atomic layer deposition for inverted organic photovoltaic cells, Carbon 50 (2012) 4483-4488.

[197] K.-L. Ou, D. Tadytin, K.X. Steirer, D. Placencia, M. Nguyen, P. Lee, N.R. Armstrong, Titanium dioxide electron-selective interlayers created by chemical vapor deposition for inverted configuration organic solar cells, J. Mater. Chem. A 1 (2013) 6794-6803.

[198] E. Ahlswede, J. Hanisch, M. Powalla, Influence of cathode sputter deposition on organic solar cells, Appl. Phys. Lett. 90 (2007) 063513.

[199] M. Arar, M. Gruber, M. Edler, W. Haas, F. Hofer, N. Bansal, L.X. Reynolds, S.A. Haque, K. Zojer, G. Trimmel, T. Rath, Influence of morphology and polymer:nanoparticle ratio on device performance of hybrid solar cells - an approach in experiment and simulation, Nanotechnology 24 (2013) 484005.

[200] H.C. Leventis, S.P. King, A. Sudlow, M.S. Hill, K.C. Molloy, S.A. Haque, Nanostructured hybrid polymer-inorganic solar cell active layers formed by controllable in situ growth of semiconducting sulfide networks, Nano Lett. 10 (2010) 1253-1258.

[201] S. Dowland, T. Lutz, A. Ward, S.P. King, A. Sudlow, M.S. Hill, K.C. Molloy, S.A. Haque, Direct growth of metal sulfide nanoparticle networks in solid-state polymer films for hybrid inorganic-organic solar cells, Adv. Mater. 23 (2011) 2739-2744.

[202] V. Kaltenhauser, T. Rath, W. Haas, A. Torvisco, S.K. Müller, B. Friedel, B. Kunert, R. Saf, F. Hofer, G. Trimmel, Bismuth sulphide–polymer nanocomposites from a highly soluble bismuth xanthate precursor, J. Mater. Chem. C 1 (2013) 7825-7832.

[203] N. Bansal, F.T.F. O'Mahony, T. Lutz, S.A. Haque, Solution processed polymer-inorganic semiconductor solar cells employing Sb_2S_3 as a light harvesting and electron transporting material, Adv. Energy Mater. 3 (2013) 986-990.

[204] M. Stefik, F.J. Heilitag, M. Niederberger, M. Grätzel, Improved nonaqueous synthesis of TiO_2 for dye-sensitized solar cells, ACS Nano 7 (2013) 8981-8989.

[205] C.D. Wagner, A.V. Naumkin, A. Kraut-Vass, J.W. Allison, C.J. Powell, J.R.Jr. Rumble, NIST Standard Reference Database 20, Version 3.4 (web version) (http:/srdata.nist.gov/xps/) 2003.

[206] H.B. Michaelson, The work function of the elements and its periodicity, J. Appl. Phys. 48 (1977) 4729-4733.

[207] M.S. White, D.C. Olson, S.E. Shaheen, N. Kopidakis, D.S. Ginley, Inverted bulk-heterojunction organic photovoltaic device using a solution-derived ZnO underlayer, Appl. Phys. Lett. 89 (2006) 143517.

[208] J.B. Kim, C.S. Kim, Y.S. Kim, Y.-L. Loo, Oxidation of silver electrodes induces transition from conventional to inverted photovoltaic characteristics in polymer solar cells, Appl. Phys. Lett. 95 (2009) 183301.

[209] S. Norioka, H. Ishii, D. Yoshimura, M. Sei, Y. Ouchi, K. Seki, S. Hasagawa, T. Miyazaki, Y. Harima, K. Yamashita, The electronic structure and energy level alignment of porphyrin/metal interfaces studied by ultraviolet photoelectron spectroscopy, Appl. Phys. Lett. 67 (1995) 1899-1901.

[210] T. Salim, Z. Yin, S. Sun, X. Huang, H. Zhang, Y.M. Lam, Solution-processed nanocrystalline TiO_2 buffer layer used for improving the performance of organic photovoltaics, ACS Appl. Mater. Interfaces 3 (2011) 1063-1067.

[211] S. Cho, K. Lee, A.J. Heger, Extended lifetime of organic field-effect transistors encapsulated with titanium sub-oxide as an ‘active’ passivation/barrier layer, Adv. Mater. 21 (2009) 1941–1944.

[212] K. Zilberberg, S. Trost , H. Schmidt, T. Riedl, Solution processed vanadium pentoxide as charge extraction layer for organic solar cells, Adv. Energy Mater. 1 (2011) 377–381.

[213] Nikiforov, M.P.; Strzalka, J.; Darling S.B. Delineation of effects of water and oxygen on the degradation of organic photovoltaic devices, Sol. Energy Mat. 110 (2013) 36-42.

[214] L. Dou, J. You, Z. Hong, Z. Xu G. Li, R.A. Street, Y. Yang, A Decade of Organic/Polymeric Photovoltaic Research, Adv. Mater. 25 (2013) 6642-6671.

[215] M.J. Greaney, R.L. Brutchey, Ligand engineering in hybrid polymer:nanocrystal solar cells, Mater. Today 18 (2015) 31-38.

[216] R. Zhou, J. Xue, Hybrid polymer-nanocrystal materials for photovoltaic applications, Chemphyschem 13 (2012) 2471-2480.

[217] J.N. Freitas, A.S. Goncalves, A.F. Nogueira, A comprehensive review of the application of chalcogenide nanoparticles in polymer solar cells, Nanoscale 6 (2014) 6371-6397.

[218] Q. Zeng, Z. Chen, Y. Zhao, X. Du, F. Liu, G. Jin, F. Dong, H. Zhang, B. Yang, Aqueous-Processed Inorganic Thin-Film Solar Cells Based on $CdSe_xTe_{1-x}$ Nanocrystals: The Impact of Composition on Photovoltaic Performance, ACS Appl. Mater. Interfaces 7 (2015) 23223-23230.

[219] Z. Chen, F. Liu, Q. Zeng, Z. Cheng, X. Du, G. Jin, H. Zhang, B. Yang, Efficient aqueous-processed hybrid solar cells from a polymer with a wide bandgap, J. Mater. Chem. A 3 (2015) 10969-10975.

[220] Z. Chen, H. Zhang, X. Du, X. Cheng, X. Chen, Y. Jiang, B. Yang, From planar heterojunction to n-i structure: an efficient strategy to improve short-circuit current and power conversion efficiency of aqueous-solution-processed hybrid solar cells, Energy Environ. Sci. 6 (2013) 1597–1603.

[221] M.T. Dang, L. Hirsch, G. Wantz, P3HT:PCBM, Best seller in polymer photovoltaic research, Adv. Mater. 23 (2011) 3597-3602.

[222] T. Rath, V. Kaltenhauser, W. Haas, A. Reichmann, F. Hofer, G. Trimmel, Solution-processed small molecule/copper indium sulfide hybrid solar cells, Sol. Energy Mater. Sol. Cells 114 (2013), 38–42.

[223] S. Dunst, T. Rath, S. Moscher, L. Troi, M. Edler, T. Griesser, G. Trimmel, Influence of TiO_x and Ti cathode interlayers on the performance and stability of hybrid solar cells, Sol. Energy Mater. Sol. Cells 130 (2014) 217-224.

[224] J.E. Halpert, F.S.F. Morgenstern, B. Ehrler, Y. Vaynzof, D. Credgington, N. C. Greenham, Charge dynamics in solution-processed nanocrystalline $CuInS_2$ solar cells, ACS Nano 9 (2015) 5857-5867.

[225] L. Lu, T. Zheng, Q. Wu, A.M. Schneider, D. Zhao, L. Yu, Recent advances in bulk heterojunction polymer solar cells, Chem. Rev. 115 (2015) 12666-12731.

[226] Y. Sun, C.J. Takacs, S.R. Cowan, J.H. Seo, X. Gong, A. Roy, A.J. Heeger, Efficient, air-stable bulk heterojunction polymer solar cells using MoO_x as the anode interfacial layer, Adv. Mater. 23 (2011) 2226-2230.

[227] Y. Suh, N. Lu, S.H. Lee, W.-S. Chung, K. Kim, B. Kim, M.J. Ko, M.J. Kim, Degradation of a thin Ag layer induced by poly(3,4-ethylenedioxythiophene):polystyrene sulfonate in a transmission electron microscopy specimen of an inverted polymer solar cell, ACS Appl. Mater. Interfaces 4 (2012) 5118−5124.

[228] M.S. Ryu, J. Jang, Enhanced efficiency of organic photovoltaic cells using solution-processed metal oxide as an anode buffer layer, Sol. Energy Mater. Sol. Cells 95 (2011) 3015–3020.

[229] M.D. Irwin, B. Buchholz, A.W. Hains, R.P.H. Chang, T.J. Marks, P-type semiconducting nickel oxide as an efficiency-enhancing anode interfacial layer in polymer bulk-heterojunction solar cells, Proc. Natl. Acad. Sci. USA 105 (2008) 2783–2787.

[230] H. Choi, B. Kim, M.J. Ko, D.-K. Lee, H. Kim, S.H. Kim, K. Kim, Solution processed WO3 layer for the replacement of PEDOT:PSS layer in organic photovoltaic cells, Org. Electronics 13 (2012) 959–968.

[231] M. Glatthaar, M. Riede, N. Keegan, K. Sylvester-Hvid, B. Zimmermann, M. Niggemann, A. Hinsch, A. Gombert, Efficiency limiting factors of organic bulk heterojunction solar cells identified by electrical impedance spectroscopy, Sol. Energy Mater. Sol. Cells 91 (2007) 390–393.

[232] M.R. Lilliedal, A.J. Medford, M.V. Madsen, K. Norrman and F.C. Krebs, The effect of post-processing treatments on inflection points in current–voltage curves of roll-to-roll processed polymer photovoltaics, Sol. Energy Mater. Sol. Cells 94 (2010) 2018–2031.

[233] F. Liu, G. Yu, J.W. Jung, W.H. Jo, T.P. Russell, T. On the morphology of polymer-based photovoltaics, J. Polym. Sci., Part B: Polym. Phys. 50 **(**2013) 1018-1044.

[234] Y. Yang, K. Mielczarek, M. Aryal, A. Zakhidov, W. Hu, Nanoimprinted polymer solar cell, ACS Nano 6 (2012) 2877-2892.

[235] M. Wang, F. Wudl, Top-Down Meets Bottom-Up: Organized donor–acceptor heterojunctions for organic solar cells, J. Mater. Chem. 22 (2012) 24297-24314.

[236] J.-T. Chen, C.-S. Hsu, Conjugated polymer nanostructures for organic solar cell Applications, Polym. Chem. 2 (2011) 2707-2722.

[237] I. Gur, N.A. Fromer, C.P. Chen, A.G. Kanaras, A.P. Alivisatos, Hybrid solar cells with prescribed nanoscale morphologies based on hyperbranched semiconductor nanocrystals, Nano Lett. 7. (2007) 409-414.

[238] H.-C. Chen, C.-W. Lai, I.-C. Wu, H.-R. Pan, I.-W.P. Chen, Y.-K. Peng, C.-L. Liu, C.-H. Chen, P.-T. Chou, Enhanced performance and air stability of 3.2% hybrid solar cells: How the functional polymer and CdTe nanostructure boost the solar cell efficiency, Adv. Mater. 23 (2011) 5451-5455.

[239] J. Conradt, J. Sartor, C. Thiele, F. Maier-Flaig, J. Fallert, H. Kalt, R. Schneider, M. Fotouhi, P. Pfundstein, V. Zibat, D. Gerthsen, Catalyst-free growth of zinc oxide nanorod arrays on sputtered aluminum-doped zinc oxide for photovoltaic applications, J. Phys. Chem. C 115 (2011) 3539-3543.

[240] N. Bao, X. Feng, C.A. Grimes, Self-organized one-dimensional TiO_2 nanotube/nanowire array films for use in excitonic solar cells: A review, J. Nanotechnol. 2012 (2012) 645931.

[241] T. Rath, C. Padeste, M. Vockenhuber, C. Fradler, M. Edler, A. Reichmann, I. Letofsky-Papst, F. Hofer, Y. Ekinci, T. Griesser, Direct extreme UV-lithographic conversion of metal xanthates into nanostructured metal sulfide layers for hybrid photovoltaics, J. Mater. Chem. A1 (2013) 11135-11140.

[242] P.R. Pudasaini, F. Ruiz-Zepeda, M. Sharma, D. Elam, A. Ponce A.A. Ayon, High efficiency hybrid silicon nanopillar–polymer solar cells, ACS Appl. Mater. Interfaces 5 (2013) 9620-9627.

[243] S. Jeong, E.C. Garnett, S. Wang, Z. Yu, S. Fan, M.L. Brongersma, M.D. McGeehe, Y. Cui, Hybrid silicon nanocone–polymer solar cells, Nano Lett. 12 (2012) 2971-2976.

[244] G. Mariani, Y. Wang, P.-S. Wong, A. Lech, C.-H. Hung, J. Shapiro, S. Prikhodko, M. El-Kady, R.B. Kaner, D.L. Huffaker, Three-dimensional core–shell hybrid solar cells via controlled in situ materials engineering, Nano Lett. 12 (2012) 3581-3586.

[245] J. Weickert, R.B. Dunbar, H.C. Hesse, W. Wiedemann, L. Schmidt-Mende, Nanostructured organic and hybrid Solar Cells, Adv. Mater. 23 (2011) 1810-1828.

[246] X. He, F. Gao, G. Tu, D.G. Hasko, S. Huettner, N.C. Greenham, U. Steiner, R.H. Friend, W.T.S. Huck, Formation of well-ordered heterojunctions in polymer:PCBM photovoltaic devices, Adv. Funct. Mater. 21 (2011) 139-146.

[247] S. Moungthai, N. Mahadevapuram, P. Ruchhoeft, G.E. Stein, Direct patterning of conductive polymer domains for photovoltaic devices, ACS Appl. Mater. Interfaces 4 (2012) 4015-4023.

[248] D. Chen, W. Zhao, T.P. Russell, P3HT nanopillars for organic photovoltaic devices nanoimprinted by AAO templates, ACS Nano 6 (2012) 1479-1485.

[249] S.Y. Chou, P.R. Krauss, P.J. Renstrom, Nanoimprint lithography, J. Vac. Sci. Technol. B: Microelectron. Nanometer Struct.-Process, Meas., Phenom. 14 (1996) 4129–4133.

[250] H. Schift, C. Spreu, M. Saidani, M. Bednarzik, J. Gobrecht, A. Klukowska, F. Reuther, G. Gruetzner, H.H. Solak, Transparent hybrid polymer stamp copies with sub-50-nm resolution for thermal and UV-nanoimprint lithography, J. Vac. Sci. Technol., B: Microelectron. Nanometer Struct.-Process, Meas., Phenom. 27 (2009) 2846-2849.

[251] M. Mühlberger, I. Bergmair, A. Klukowska, A. Kolander, H. Leichtfried, E. Platzgummer, H. Loeschner, C. Ebm, G. Grützner, R. Schöftner, UV-NIL with working stamps made from ormostamp, Microelectron. Eng. 86 (2009) 691–693.

[252] H. Amenitsch, M. Rappolt, M. Kriechbaum, H. Mio, P. Laggner, S. Bernstorff, First performance assessment of the small-angle X-ray scattering beamline at ELETTRA, J. Synchrotron Radiat. 5 (1998) 506-508.

[253] A. Fischereder, T. Rath, W. Haas, H. Amenitsch, D. Schenk, A. Zankel, R. Saf, F. Hofer, G. Trimmel, Investigation of $CuInS_2$ thin film formation by a low-temperature chemical deposition method, ACS Appl. Mater. Interfaces 4 (2012) 382-390.

[254] J. Wernecke, F. Scholze, M. Krumrey, Direct structural characterisation of line gratings with grazing incidence small-angle X-ray scattering, Rev. Sci. Instrum. 83 (2012) 103906.

[255] M. Yan, A. Gibaud, On the intersection of grating truncation rods with the ewald sphere studied by grazing-incidence small-angle X-ray scattering, J. Appl. Crystallogr. 40 (2007) 1050-1055.

[256] D.R. Rueda, I. Martín-Fabiani, M. Soccio, N. Alayo, F. Pérez-Murano, E. Rebollar, M.C. García-Gutiérrez, M. Castillejo, T.A. Ezquerra, Grazing-incidence small-angle X-ray scattering of soft and hard nanofabricated gratings, J. Appl. Crystallogr. 45 (2012) 1038-1045.

[257] R. Meier, H.-Y. Chiang, M.A. Ruderer, S. Guo, V. Körstgens, J. Perlich, P. Müller-Buschbaum, In situ film characterization of thermally Treated Microstructured Conducting Polymer Films, J. Polym. Sci., Part B: Polym. Phys. 50 (2012) 631-641.

[258] P.-L.T. Boudreault, A. Michaud, M Leclerc, A new poly(2,7-dibenzosilole) derivative in polymer solar cells, Macromol. Rapid Commun. 28 (2007) 2176–2179.

[259] O. Glatter, O. Kratky, Small angle x-ray scattering, Chapter 2 – General theory, Academic Press (1982) 46–48.

[260] N. Bansal, L.X. Reynolds, A. MacLachlan, T. Lutz, R.S. Ashraf, W. Zhang, C.B. Nielsen, I. McCulloch, D.G. Rebois, T. Kirchartz, M.S. Hill, F.C. Molloy, J. Nelson, S.A. Haque, Influence of crystallinity and energetics on charge separation in polymer-inorganic nanocomposite films for solar cells, Sci. Rep. 3 (2013) 1531.

[261] European Commission Joint Research Centre, Institute for Energy and Transport, Photovoltaic Geographical Information System (PVGIS), http://re.jrc.ec.europa.eu/pvgis/cmaps/eur.htm, 24.02.2016.